SAPIENZA
Università di Roma
Facoltà di Farmacia e Medicina

Ph.D. in
MORPHOGENESIS AND TISSUE ENGINEERING

XXXV Cycle
(A.A. 2019/2020)

Development of innovative techniques, experimental devices and testing protocols for the measurement of muscle and neuromuscular junction functionality in Amyotrophic Lateral Sclerosis

Ph.D. Student
Flavia Forconi

Tutor
Prof. Emanuele Rizzuto

Coordinator
Prof. Antonio Musarò

CONFIDENTIALITY NOTICE

Reviewers and PhD committee members are obliged to keep the files confidential and to delete all records after completing the review process.

Receipt of scientific papers, in order to obtain the title of PhD, as a committee member of PhD course in Morphogenesis and Tissue Engineering requires compliance with the following regulations:

i. consider the Confidential and Reserved Information as strictly private and take all reasonable steps to keep it that way;

ii. use the confidential and reserved information only for the purpose for which it was provided or disclosed, undertaking not to disclose the information contained in the documents received to third parties;

iii. guarantee maximum confidentiality, also in compliance with the current legislation on trademarks, copyrights and patents for industrial inventions and on the basis of the privacy legislation, pursuant to Legislative Decree 196/2003, regarding know-how and all the information acquired, which cannot in any way, in any case and for any reason be used for one's own or others' profit and/or be disclosed and/or reproduced or otherwise disclosed to third parties.

Index

1. Summary

Amyotrophic Lateral Sclerosis (ALS) remains an invariably fatal disease, in which neuromuscular junction (NMJ) functionality is strongly impaired. To this, the aim of this research project was to develop a series of novel testing tools for a precise assessment of the altered communication between muscle and nerve in ALS progression. A novel technique for the *in-situ* measurement of murine Tibialis Anterior (TA) NMJ functionality in isotonic conditions was developed and validated. A novel parameter, named *Isotonic Neurotransmission Failure* (*INF*), was proposed. Results showed an increase in *INF* of $SOD1^{G93A}$ mouse TA muscles at the end-stage of the disease, highlighting, for the first time, an increased impairment of NMJ functionality in isotonic conditions. An embedded system for the measurement of 3D engineered skeletal muscle tissues' contractility with a non-invasive technique was proposed. Results showed the capability of the system to not impair tissue's contractility during the entire growth, and to discriminate healthy and pathological conditions. Finally, a 3D microfluidic device was designed and realized to promote the formation of NMJ between spinal cord-derived neuronal cells and 3D engineered skeletal muscle. Results showed a good attraction between these two cells populations, paving the basis for the development of a more comprehensive 3D NMJ *in-vitro* model. On the other hand, since extracellular vesicles (EVs) are involved in ALS pathological proteins transportation, a series of preliminary experiments with muscle cells' populations was carried out, with the final aim of evaluating the role of $SOD1^{G93A}$ mice-derived EVs on the novel experimental models here proposed. Results showed that $SOD1^{G93A}$ mice-derived EVs increased in number during the ALS progression, and impaired C2C12 cells' differentiation. In conclusion, a series of novel testing tools have been developed for a precise assessment of the NMJ functionality in different models which, of note, can be also employed to unravel the mechanism behind muscle-nerve impairments in other neurodegenerative pathologies.

2. Introduction

2.1 Amyotrophic Lateral Sclerosis

Amyotrophic Lateral Sclerosis is a fatal neurodegenerative disease characterized by the progressive loss of motor neurons (MNs) in the brain, brain stem and spinal cord. This motor neurons degeneration leads to muscle atrophy, weakness, progressive paralysis and, ultimately death, typically within 2-5 years after diagnosis [1], [2]. The most common ALS form is the sporadic one (sALS), with no family linkage and unknow etiology, while the remaining 5-10 % of cases represents the familial ALS (fALS), with a pattern of autosomal-dominant inheritance with variance in known ALS-linked genes [3]. It has to be noted that the two forms, although different, have similar pathological hallmarks and symptoms, suggesting that the mechanisms of the progressive neurodegeneration of cortical and spinal MNs share common component in sALS and fALS. ALS research has primarily focused on mechanisms regarding MNs cell death. However, degenerative processes in skeletal muscle, particularly involving neuromuscular junctions, have been observed in the early stages of disease progression [1], [4]. Many studies have supported the “dying-back” hypothesis, according to which a progressive distal NMJ degeneration occurs, followed by axonal degeneration and MNs death [5]. In addition, the generation and characterization of a specific $SOD1^{G93A}$ mouse model (MLC/$SOD1^{G93A}$) revealed that the muscle-specific expression of mutant SOD1 gene caused accumulation of reactive oxygen species (ROS), muscle atrophy, NMJ displacement and neuron degeneration, in line with “dying-back” hypothesis [6].

Recent studies have shown common alterations in gene expression for sporadic and familial ALS forms, highlighting a possible sharing of the pathogenetic mechanism [7]–[9]. Among these, the most commonly mutated genes in ALS patients are Chromosome9 open reading frame 72 (C0orf72), which occurs in

30-40 % cases of fALS, superoxide dismutase 1 (SOD1), accounting for 14-23 % of fALS and 1-7 % for sALS, transactive response DNA-binding protein (TARDBP) and fused in sarcoma (FUS), which both occur for about 5 % of fALS cases [8], [9]. In particular, among the familial cases, 20 % is due to mutation in the gene encoding Cu/Zn superoxide dismutase (SOD1), a homodimeric metallo-enzyme which catalyzes the dismutation of the toxic superoxide anion O_2^- to O_2 and H_2O_2 [10]. SOD1 is an antioxidant enzyme involved in the detoxification of reactive oxygen species (ROS) and it normally reduces oxidative stress by converting superoxide anions to hydrogen peroxide [11]. More than 100 mutations have been identified in SOD1 gene, which are able to induce a cytotoxic gain of functions as a result of abnormal aggregation of misfolded SOD1 protein in MNs and muscles, thus leading to the generation of free radicals and to a progressive degeneration and death of MNs [7], [12]. In fact, SOD1-mediated toxicity is not due to loss of its antioxidative function but to a gain of one or more toxic properties [13], [14].

Recently, mutations in several genes have been linked to familial forms of ALS, even if the mechanisms behind this correlation are still unknown [15]. On the contrary, the mechanisms that link mutations in the superoxide dismutase gene (SOD1) to ALS have been extensively studied since 1993, when Rosen et al. [10] reported a tight genetic linkage between fALS and mutations of Cu/Zn superoxide dismutase gene. High expression of this altered gene in the central nervous system (CNS) is associated with a progressive decline of motor function, as well as degenerative changes and death of MNs within spinal cord and brainstem, suggesting a relationship between altered SOD1 activity and motoneurons degeneration [12].

To date, more than 100 mutations in SOD1 gene have been described in ALS, thus allowing the generation of different animal models of ALS. Mice over-expressing the mutant forms of SOD1 enzyme (mSOD1 mice) developed a motor neuron disease with all the clinical features occurring in sporadic and familial forms of ALS, as progressive motor neurons and neuromuscular junction

degeneration, weight loss from denervation-induced muscle atrophy and paralysis [16]. Among all the animal models used to study ALS, $SOD1^{G93A}$ mouse is the most commonly employed [13] and it is based on the expression of high levels of human SOD1 with a glycine-to-alanine substitution in position 93, developing neurodegeneration of spinal MNs and progressive motor deficit. $SOD1^{G93A}$ ALS mouse model carries the mutation in an array of, approximately, 25 copies of the human transgene, randomly inserted into mouse chromosome 12 [17].

As regarding the progression of ALS in $SOD1^{G93A}$ mice, the onset of clinical symptoms occurs at 80-90 days, approximately, while the death occurs at 140-150 days of age [13]. Adult post-natal age (P80-P120) is considered the symptomatic stage of $SOD1^{G93A}$ mouse model due to the decline in motor function and MNs cell death. Therefore, the period prior to 80 days is usually considered as the presymptomatic phase of disease. Many studies have largely characterized the early pathogenesis in several muscle types of $SOD1^{G93A}$ mouse models, by a molecular and functional point of view. For example, Vinsant et al. [18] demonstrated that in $SOD1^{G93A}$ mice 20 % of MNs, both central and peripheral, undergoes degeneration by P60, whereas NMJ innervation in fast fatigable muscles is reduced of 40 % starting from P30. On the other hand, Gould et al. [19] showed a reduction in the innervation of Gastrocnemius muscle fibers of 20 % without any changes in axonal transport. Soleus muscle showed denervation and muscle atrophy at around P70, and a drop in motor unit number and muscle force is not detected until P90 [18]. Hegedus et al. [20], [21] studied the loss of motor units, and therefore the decrease of maximum tetanic force in fast-twitch muscles (Tibialis Anterior, medial gastrocnemius, Extensor Digitorum Longus (EDL)) and slow-twitch muscles (Soleus) of $SOD1^{G93A}$ mice during the progression of ALS. In particular, they have demonstrated that fast-twitch muscles undergo a decrease of the motor unit number and of tetanic force, from 40 days of age to 90 days of age, when symptoms manifest. On the contrary, slow-twitch muscles display a loss of motor units and a

decrease in tetanic force at the onset stage, i.e. approximately at 90 days of age. In addition to the force decline, a work by Derave and colleagues [22] showed that contraction and relaxation rates in EDL and Soleus muscles slowed with increasing ageing. In both muscles, however, $SOD1^{G93A}$ mice exhibited improved fatigue resistance and faster recovery from fatigue than control muscles. Tab. 1 summarizes the effects of ALS progression on fast-twitch and slow-twitch muscles.

Table 1. Effects of ALS progression on fast-twitch and slow-twitch muscles.

	Decrease of motor unit number	**Decrease of tetanic force**	**Degeneration of motor neurons**
Fast-twitch muscles	From 40 to 90 days of age	From 40 to 90 days of age	From 30 days of age
Slow-twitch muscles	From 90 days of age	From 90 days of age	From 60 days of age

To this, $SOD1^{G93A}$ mouse model has proven to be an invaluable tool for studying ALS pathogenetic mechanisms, by a molecular and functional point of view, during disease progression.

2.2 Techniques for the measurement of neuromuscular junction functionality

The neuromuscular junction is a specialized chemical synapse with an important role in transmitting and amplifying information from spinal motor neuron to skeletal muscle [23]. The loss of connection between muscle and nerve is severely impaired in several pathological conditions, as aging, muscular dystrophies and ALS. To this, the measurement of muscle and NMJ functionality may play a crucial role, with the aim of providing new insights on the physio-pathological interplay between muscle and nerve, as well as on the potential alterations directly related to skeletal muscle or indirectly due to NMJ impairment.

Muscle and NMJ functionality can be measured through the *ex-vivo* and *in-situ* experimental methodologies. In the first one, to reproduce, as close as possible, the physiological conditions supported by the muscle *in-vivo*, excised muscles are kept in a temperature-controlled Krebs-Ringer bicarbonate buffer solution continuously oxygenated for all the duration of the experiments, while controlled electrical pulses replace action potentials, thus allowing the release of Ca^{2+} and the resulting contraction of the muscle. On the contrary, in the *in-situ* methodology, the innervation, blood supply and mineral perfusion remain intact for all the duration of the experiment. NMJ functionality can be measured by comparing the contractile response of the muscle elicited by direct stimulation, occurring when electrical pulses are delivered on muscle membrane, and indirect stimulation, obtained with punctual stimulation of the nerve [24]. Since the direct stimulation completely bypasses the neurotransmission signalling, any differences in the two responses can be attributed to alterations of NMJ. Changes in contractile kinetics, maximum and specific force may be measured, even if the most interesting evaluation of NMJ functionality concerns the capability of transmitting neuronal signal when subjected to fatigue. Indeed, when the muscle is repeatedly stimulated to contract, it develops fatigue and the synaptic transmission is impaired [25]. Different studies have widely investigated the fatigue of muscle-nerve preparations in isometric conditions, i.e. the muscle is kept fixed at a constant length [26]–[29]. For example, Fogarty et al. investigated the neuromuscular transmission failure of *ex-vivo* Tibialis Anterior and diaphragm muscles in a rodent model of hypertonia and in aged rats [26], [27]. They showed that the early-onset hypertonia is strongly associated with impaired neuromuscular transmission and revealed an altered NMJ functionality in diaphragm muscles of aged rats at higher frequency. Personius and Sawyer [28] investigated the extent of neurotransmission failure in the diaphragm of adult dystrophic mdx mice. They proposed an isometric fatigue protocol in which a single direct stimulation on muscle membrane was followed by 14 indirect

stimulations through the nerve, with the aim of stressing NMJ. The fatigue of synaptic transmission in isometric conditions can be measured with two specific parameters, namely Neurotransmission Failure (NF) [24] and Intratrain Fatigue (IF) [30]. Briefly, NF expresses the difference in force decrease obtained through the indirect and direct stimulations normalized to that computed through the direct stimulation during the first contraction, while IF represents the force decrease within a single pulse train of stimulation. Similarly, Rizzuto et al [31] measured the NMJ functionality in soleus and diaphragm muscles excised from $SOD1^{G93A}$ ALS mouse model, also through the measurement of NF and IF parameters. Although all these previous studies contributed to obtain a more comprehensive understanding of NMJ functionality in different pathological conditions, they were all carried out in isometric conditions. However, the situation that better mimics the *in-vivo* muscle dynamic activity is the isotonic one, in which the muscle is allowed to shorten. Different studies investigated the isotonic fatigue only for direct stimulation on several muscle types [32]–[34]. In addition, in all these studies the muscle was repeatedly stimulated to shorten against a load equal to one-third of its maximal force (tetanic force), usually known as reference optimal force [35], [36]. This value was chosen as the best representative of the force at which the muscle generated its maximum power [35], [37], [38]. However, when testing muscle types from different animal models, the reference optimal force may significantly differ from the force at which the muscle really generates its maximum power and, consequently, significant errors might be introduced in all the parameters measured during isotonic fatigue protocol.

To this, in this thesis work, an isotonic fatigue protocol was first developed, in which the tested muscle was able to lift the experimental optimal force, i.e. the force value at which the muscle really generated the maximum power, computed through a real-time measurement of muscle power during the application of the after-load technique. Subsequently, we proposed a novel experimental technique, together with an extensive protocol, for the measurement

of NMJ functionality in isometric and isotonic conditions, with a particular reference to isotonic fatigue test. To extensively characterize the fatigue behaviour in isotonic conditions, a novel parameter, namely *Isotonic Neurotransmission Failure*, was also proposed, which computes the difference in shortenings occurred when stimulating the muscle through the nerve and on the membrane, normalized to that obtained when stimulating the muscle on its membrane during the first contraction.

Finally, this experimental technique was applied to evaluate the NMJ functionality of $SOD1^{G93A}$ mice at the presymptomatic, onset and end-stage of ALS progression, with the aim of providing new insights on the pathological interplay between muscle and nerve with the spreading of the disease.

2.3 Skeletal muscle tissue engineering

Tissue engineering (TE) is a multidisciplinary approach which involves the combination of living cells with a synthetic bioartificial or natural support to develop substitutes characterized by structural, mechanical, and functional properties as close as possible to the *in-vivo* tissue [39], [40]. Among all the tissues, skeletal muscle is the most abundant in the body, representing the 40-50 % of the average weight [41], and it is associated to several pathological conditions [42], [43]. The engineering of *in-vitro* skeletal muscle holds promises for the treatment of a variety of muscle diseases [44], including skeletal myopathies, such as muscular dystrophy or spinal muscular atrophy [45], [46], as well as for the design of *in-vitro* models employed for drug screening or investigation of phenomena regulating disease onset and progression [47]–[49]. The X-MET is a 3D *eX-vivo* Muscle Engineered Tissue generated from murine primary culture without using any scaffold [50], which shows morphological and functional characteristics close to native skeletal muscle. X-MET has been characterized for its spontaneous [51] and electrically induced [50] contractions, as well as for its mechanical power [52]. Therefore, the development of new technologies to

assess the contractile functions of *in-vitro* engineered tissues, also allowing for embedding a series of measurement sensors, is essential to improve tissues' development and might represent a crucial tool for the study of various neuromuscular and muscular diseases.

Nowadays, many of the methods used for contractile force measurements are the direct ones, based on the use of a micro-force transducer coupled with the muscle specimen [53]–[55]. These methods are invasive, since it is necessary to connect the tissue to be tested with the transducer each time a measurement is needed, and their use can introduce some limitations, such as the changes of the mechanical properties of the specimen. In fact, with this invasive method, it is possible to measure the mechanical properties of the specimen only once since it results damaged by the coupling with the micro-force transducer. To overcome these limitations, non-invasive devices and techniques, such as the optical ones, have been recently used for the study of tissues' biomechanical properties, as the contractile force. Their working concept is mainly based on the measurement of a cantilever or post deflection [56]. For example, Gaitas A. et al. [57] developed a versatile method for the measurement of contractile forces of cardiac myocytes characterized by a micro-machined cantilever sensor with an embedded deflection-sensing element, thus offering unlimited possibilities for monitoring cardiac contractility in different pathological conditions. Regarding skeletal muscle contractility, a Si-MEMS (Micro Electro Mechanical System) device, consisting of a microcantilever and a base, was designed and fabricated by Shimizu et al. [58] for the measurement of the active tension generated through electrical stimulation by skeletal muscle myotubes derived from C2C12 cell line. As regards the measurement accuracy of this device, to achieve reliable and reproducible measurements of the active tension of skeletal muscle tissues, it would be necessary to investigate the relationship between the number of cultured myotubes and the active tension. All these methodologies are the most used for the *in-vitro* measurement of 3D engineered skeletal muscle tissue, taking advantages from the non-invasiveness for the tissue as well as the

possibility to perform continuous monitoring of muscle contractility. However, they are highly complex to be realized and they are difficult to be integrated with other measurement systems, as for example high-resolution microscopy.

Recently, other emerging technologies have been proposed as an alternative way to perform contractility measurements, such as the Traction Force Microscopy, traditionally used for the measurement of the cell contractility [59] and now extended to the tissue-level [60], and the microelectrodes arrays (MEAs) system [61], whose working concept is based on the recording of the bioelectrical signal generated by the culture. These methodologies are based on a non-invasive approach, and they are compatible with high-resolution microscopy, but present some limitations. First of all, they do not provide a direct measurement of the contractile force, but of the contraction and relaxation velocities curves, where contractility is usually presented as percentage of the movement [62]. On this basis, the indirect measurement of contractile force results affected by the effect of propagation of uncertainty. Other limitations are inherent to the setup, being compatible only with specific types of culture (such as those characterized by a low cellular density [63]) and requiring the entire tissue to be placed in direct contact with the device [61].

Within this context, in this thesis the development of an embedded sensor for the continuous monitoring of muscle engineered tissues' contractility by using an optical tracking method was proposed. This sensor was then used, as *proof-of-concept*, to measure the contractile force of X-MET, treated with Bovine Serum Albumin (BSA), for 5 consecutive days, to test its non-invasiveness, in terms of correct growth, as well as its capability to discriminate pathological and physiological conditions.

In parallel, tissue engineering approach can also be used to generate three-dimensional models that well mimic the physiological conditions of neuromuscular junction. As previously described, changes in NMJ structure have been detected in several motor neuron diseases, as spinal muscular atrophy and Amyotrophic Lateral Sclerosis, suggesting that NMJ could be a relevant therapeutic target [64]. Two-dimensional (2D) cultures represent the

most traditional approach, and they are obtained by a layer of myotubes obtained from myoblasts onto which motor neurons are uniformly plated. This technical approach allows understanding the basis of NMJ formation [65]. For example, Frank and Fischbach [66] showed acetylcholine receptors (AChRs) clustering. In addition, Ullian et al. [67] revealed the role of Schwann cells on NMJ formation as well as Guo et al. [68] demonstrated the role of MNs in enhancing neonatal myosin heavy chain in primary skeletal muscle cells. Peterson et al. [69] showed the crucial role of the innervation in muscle regeneration by using organotypic cultures in collagen substrate of skeletal muscle fibres oriented toward ventral-root nerve fibres of fetal rodent spinal cord. In addition, Das et al. [70] performed co-cultures experiments with rat embryonic neurons and rat primary muscle cultures and their results showed a long-term survival of the co-culture as well as a maturation of the neonatal myosin heavy chain and a good immunostaining of NMJ model. In 2014, Chipman et al. [71] used co-cultures of murine embryonic stem-cell derived MNs and primary chick myotubes to study the role of neuronal cells' adhesion molecule to critical assess dysfunction in NMJ maturation. In 2015, Demestre et al. [72] realized a NMJ model composed of MNs and myotubes derived from human iPSCs. However, these 2D systems do not provide information about the intricate signalling networks that exist between NMJs and the biological environment [73] and show limitations to perform functional tests.

To overcome 2D co-cultures, three-dimensional (3D) cell culture systems have gained increasingly interest in drug discovery and tissue engineering due to their advantages in providing more physiologically relevant information and more predictive data for *in-vivo* tests, compared to 2D culture systems. However, despite different engineered muscle tissues have been proposed during the last decades [50], [74], [75], only a limited number of papers regarding the integration of motor neurons with a heterogeneous 3D skeletal muscle construct are reported in the literature. At this point, it is interesting to note that skeletal muscle interacts with several components, including the autonomic nerves for pulse transmission, the vessels for efficient oxygenation, and the embedded regulatory

and metabolic machinery for maintaining cellular homeostasis [76]. Indeed, only a heterogeneous cell population guarantees homeostatic processes and allows to better mimic the processes of vascularization and innervation *in-vitro* [74]. In 2015, Morimoto et al. [77] described the generation of three-dimensional free-standing skeletal muscle fibres obtained from murine C2C12 cells co-cultured with motor neurons derived from neutrospheres of mouse neural stem cells, by using PDMS and Matrigel solutions. More recently, Bakooshli et al. [78] reported a human tissue engineered NMJ model constituted by primary myoblasts and iPSC-derived motor neurons. Finally, with the development of tissue engineering, different systems have been proposed to improve the alignment of myotubes, as the use of micro-fluidics device or electro-spinning, with the final aim of increasing the fusion and formation of NMJ. In 2015, Yoshida et al. [79] showed the incorporation of human SMA motor neurons in conjunction with healthy murine muscle in a microfluidic system and in 2018, Osaki et al. [80] reported an ALS-on-a-chip model in which they plated ALS motor neurons and cells obtained from health human muscle. Another work described the potential use of a microfluidic platform allowing simultaneous 3D co-culture of mouse embryonic stem cell (mESC)–derived motor neurons and skeletal muscle cells using PDMS chambers separated by flexible pillars that serve to direct neurite outgrowth as well as to deflect upon muscle contraction [65]. Using optogenetic hiPSC-induced motor neurons from patients with sporadic ALS, Vila et al. [81] have quantified neurite outgrowth during the pathogenesis. However, the NMJ models described in these papers lack the skeletal muscle complexity, and only few of them proceeded also with functional evaluation and a specific study of ALS neurodegenerative disease.

To this, this part of the project aimed at filling the gap that still exists in the generation of a 3D NMJ model, by developing an innovative microfluidic device to enhance and promote the formation of NMJ between X-MET and embryonic mouse spinal cord-derived cells.

2.4 Role of extracellular vesicles in Amyotrophic Lateral Sclerosis

The progression of ALS is mostly mediated by altered intercellular communication in the spinal cord between neurons and glial cells [82]. Intercellular communication is an essential hallmark of multicellular organism, and it can be mediated through direct cell-cell contact or transfer of secreted molecules, as well as extracellular vesicles [83]. Extracellular vesicles have become an interesting research field, since they are known to mediate near and distant intercellular communication within and between different cell types and tissues, thus affecting the pathological and physiological conditions of recipient cells, as observed in metastatic cancer and neurodegenerative diseases [84]–[87].

EVs are spherical structures, and are mainly classified in exosomes, microvesicles and apoptotic bodies according to their biogenesis, size and mechanism of secretion [83], [88]. In detail, exosomes are formed when multivesicular bodies (MVBs) fuse with plasma membrane and release vesicles with a size ranging from 50 to 200 nm [83], [89], [90]. Microvesicles originate from the direct budding of plasma membrane in response to increased calcium influx and they are larger than exosomes, with a size of 100-1000 nm [91]. Finally, apoptotic bodies are released form apoptotic or dying cells and are characterized by a size between 500 nm and 2 μm [92]. Extracellular vesicles have been derived from different body fluids, including blood [93], urine [94], saliva [95] and cerebrospinal fluid [83], with several isolation and purification methods.

Functions of EVs in physiological and pathological processes depend on the ability of EVs to interact with recipient cells in delivering their cargo of proteins, lipids, RNAs, microRNAs (miRNAs) and non-coding RNAs, as shown in Fig.1.

After binding to recipient cells, EVs may remain stably associated with the plasma membrane or dissociate, directly fuse with the plasma membrane, or be internalized through distinct

endocytic pathways (Fig. 1). When endocytosed, EVs may subsequently fuse with the endosomal delimiting membrane or be targeted to lysosomes for degradation.

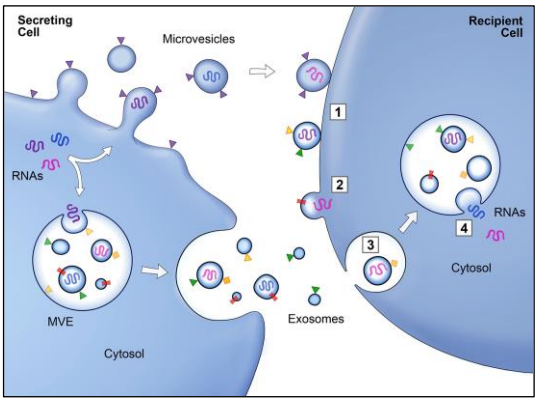

Figure 1. Schematic of EVs transfer content to recipient cell [83].

In the last two decades, extracellular vesicles' role has been widely investigated in several neurodegenerative diseases, as multiple sclerosis, Alzheimer disease (AD) and Amyotrophic Lateral Sclerosis. For example, Casella G. et al. reported a significant reduction in tissue damage of multiple sclerosis mouse model after the injection of EVs engineered to contain the anti-inflammatory cytokine IL-4 [96]. In AD, it has been demonstrated that β-amyloid peptides, which are intracellularly generated, were released into the extracellular space, in association with exosomes [97]. As regarding ALS, it has been hypothesized that pathological proteins, as mutant SOD1, FUS and TDP-43, can be transported through extracellular vesicles [98], highlighting the key role of EVs in the spreading of the disease. Tab. 2 summarizes the role and effects of EVs in neurodegenerative diseases.

Table 2. Role and effects of EVs in neurodegenerative diseases.

Neurodegenerative disease	Role/effects of EVs
Multiple sclerosis	Reduction in tissue damage after the injection of EVs containing IL-4
Alzheimer disease	EVs as intercellular mediators of β-amyloid peptides
Amyotrophic Lateral Sclerosis	EVs involved in the transportation of ALS pathological proteins

Despite EVs have been widely investigated when derived from cell lines and primary cell cultures [98], [99], only few publications investigated their involvement in ALS development and progression, whether in patients or animal models. For example, Sproviero et al. [100] have characterized microvesicles (MVs) and exosomes (EXOs) derived from sporadic ALS patients' blood, demonstrating a different concentrations and size when compared to healthy controls. In addition, they observed that sALS patients-derived MVs were significantly enriched in SOD1, TDP-43, phosphor-TDP-43 and FUS proteins in comparison to controls, thus suggesting that MVs might play a crucial role in ALS propagation. In addition, it was demonstrated that central nervous system (CNS)-derived EVs from $SOD1^{G93A}$ mice at the onset of ALS originated from astrocytes and neurons and contained abundant misfolded SOD1 protein [101]. Since ALS is a multisystemic disease, different studies investigated the role of EVs when derived from primary muscle cells of ALS patients. Anakor et al. confirmed the neurotoxicity of vesicles secreted by ALS patients' myotubes on recipient motor neurons, astrocytes and myotubes [84]. In particular, these exosome-like vesicles were able to reduce the survival of motor neurons and of myotubes and to decrease neurite length and branching. In agreement with these studies, Le Gall et al. [102] demonstrated that ALS patients' muscle derived vesicles were toxic to motor neurons, which established the skeletal muscle as a potential source of vesicle-mediated toxicity in ALS. As regarding the cargo of EVs in terms of microRNAs, it was demonstrated that myotube-derived exosomes from atrophied muscles were enriched in miR-29b-3p, which could be efficiently transferred to neuronal

cells, by inhibiting neuronal differentiation and possibly affecting the integrity of neuromuscular junction [103]. Moreover, Rizzuti et al. [104] performed microRNA expression profile analysis of iPSC-derived motor neurons and related exosomes (EXOs) from familial ALS patients, demonstrating a down regulation of miR625 in EXOs, a target of RNA-p21, which mediates neuroinflammation, oxidative stress and apoptosis.

Taken together, all these findings suggested that EVs derived from ALS mouse models and patients might play a crucial role in the progression of the disease. To this, with the future aim of evaluating the effects of EVs on different models (3D engineered construct, NMJ model, muscle-nerve preparations), a molecular characterization of EVs derived from $SOD1^{G93A}$ ALS mouse models at the presymptomatic, onset and end-stage of the disease was conducted, with an investigation of their physio-pathological effects on skeletal muscle C2C12 cell functions.

3. Aims

Amyotrophic Lateral Sclerosis remains an invariably fatal disease in absence of any effective therapy. Novel approaches for a more comprehensive investigation of the impairment in NMJ functionality are therefore needed. In view of this, the general aim of my thesis project was to develop and validate novel experimental tools for a precise assessment of the altered communication between muscle and nerve in $SOD1^{G93A}$ ALS mouse model during disease progression. In addition, since it is known that extracellular vesicles are involved in ALS pathological proteins transportation, as toxic mediators [84], [102] , a series of experiments to study the effects of EVs derived from ALS mouse model on muscle cells' populations was conducted, with the final aim of evaluating the role of EVs on the experimental models here proposed.

The experimental plan was designed considering the following aims:

1. Development of innovative experimental techniques, devices and testing protocols for the measurement of muscle and NMJ functionality in ALS progression. A novel technique for the *in-situ* measurement of murine Tibialis Anterior NMJ functionality in isotonic conditions, together with a novel parameter, *Isotonic Neurotransmission Failure*, were proposed. An embedded system for the measurement of 3D engineered skeletal muscle tissues' contractility with a non-invasive technique was developed. Finally, a 3D microfluidic device was designed and realized to promote the formation of NMJ between spinal cord-derived neuronal cells and 3D engineered skeletal muscle.

2. Molecular characterization of EVs derived from $SOD1^{G93A}$ ALS mouse model. The goal of this part of the project was to investigate the physio-pathological role of EVs in the modulation of C2C12 cell line functions.

4. Results

4.1 Development of techniques, devices and testing protocols for the measurement of muscle and neuromuscular junction functionality

4.1.1. Measurement of SOD1^{G93A} mice neuromuscular junction functionality in isometric and isotonic conditions

With the aim of deeply characterizing NMJ functionality in isotonic conditions, an innovative experimental protocol for isotonic fatigue was first developed, in which each muscle was tested to repeatedly shorten against a load equal to the experimental optimal force rather than to the reference value [105]. To this, a sub-VI (LabView 2019, NI) for the real-time measurement of the maximum power generated by the muscle, and therefore of the experimental optimal force, was developed to be run in parallel of the main program. Once the Hill's curve [35] was computed after the application of the after-load technique, the developed program estimated the power delivered by the muscle by multiplying the resistive loads to shortening velocity values over the entire range of forces. Finally, the experimental optimal force (F_{exp}) was computed as the force value corresponding to the maximum power and, subsequently, employed as the resistive load that the muscle had to lift during isotonic fatigue test. Fig. 2 shows an example of the power curves for Tibialis Anterior muscle, stimulated directly, obtained with two distinct experiments. For both tests, the maximum power was generated by the muscle at a force level higher than the reference one, equal to one-third of the corresponding tetanic force (F_{ref} = 33 % of F_{Tet}) (dashed line in Fig. 2). However, whether in one of the tested muscles the experimental optimal force was quite close to the reference one (37 %), in the other tested muscle it was extremely higher than that (44 %).

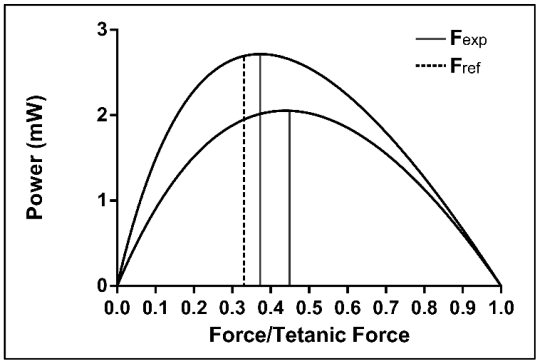

Figure 2. Example of power curves for Tibialis Anterior (TA) muscle, stimulated directly, related to two distinct experiments [105].

Of note, in all the experiments conducted to validate the technique and compute the errors associated in the wrong use of the reference optimal force, the force value corresponding to the maximum power delivered by the TA muscle was higher than the theoretical one. In particular, the experimental optimal force was, on average, equal to 39.46 ± 1.4 %.

In Fig. 3 it is reported the mean values and standard deviation (SD) of fatigue time measured for TA muscles tested at experimental optimal force and for TA muscles tested at reference force.

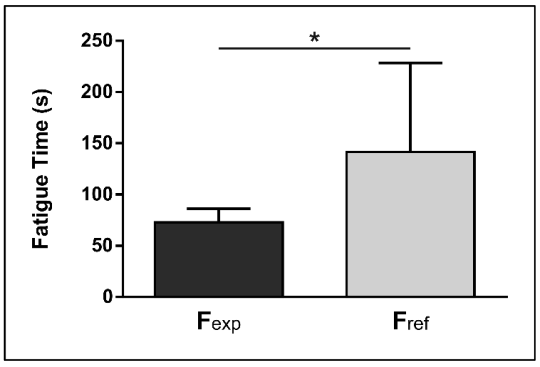

Figure 3. Tibialis Anterior muscle fatigue time measured during isotonic fatigue protocol, when muscles shortened against a load equal to F_{exp} (black) and to F_{ref} (grey). Values are mean ± SD. *: p-value<0.05 [105].

As expected, for TA muscles tested at the experimental optimal force the average fatigue time (72.8 ± 13.4 s) was significantly lower than the value obtained for the group of muscles tested at the reference optimal force (141.5 ± 86.9 s), being this reduction of about 50 %. Interestingly, the fatigue time obtained when testing muscles to contract against the experimental optimal force showed a dramatic reduction in the measurement of the variance, whereas the coefficient of variation (CV) decreased from 61.4 % to 18.4 % on average.

The sum of isotonic power and work values computed for each isotonic fatigue trial and normalized to TA muscle weight are shown in Fig. 4.

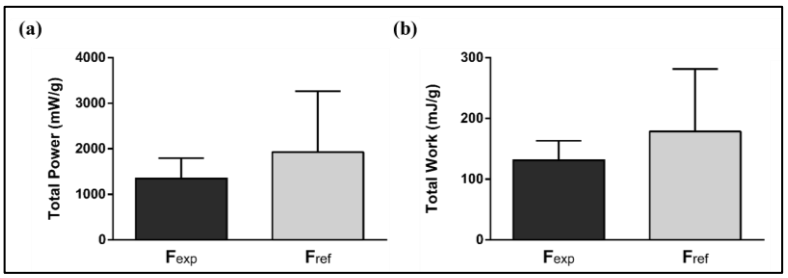

Figure 4. Normalized total mechanical a) power and b) work during the development of isotonic fatigue. Values are mean ± SD [105].

Results related to power and work were in line to what already found for the fatigue time. A decrease of both power and work was reported when testing muscles to shorten against the experimental optimal force, even if not statistically significant. Once again, a huge reduction of the variance in the measurements was reported, with CV values lowering from 69.24 % to 33.10 % and from 57.55 % to 24.49 % for power and work, respectively.

On this basis, we developed an innovative experimental technique, together with a continuous testing protocol, for the *in-situ* measurement of $SOD1^{G93A}$ mice NMJ functionality in isometric and isotonic conditions, with a particular reference to isotonic fatigue, when TA muscle was stimulated directly on its membrane and indirectly through the sciatic nerve [106]. The protocol was

constituted of five different phases: twitch test in isometric conditions (1), force-frequency isometric test (2), after-load test in isotonic conditions (3), isometric fatigue paradigm (4) and isotonic fatigue test (5). Fig. 5 shows an example of the entire stimulation protocol with force and shortening values measured for a control TA muscle.

The muscle was initially held isometric and stimulated alternatively with four 1 ms single pulses, two delivered directly and two through the nerve with a rest period of 15 s between each one. Time to peak (TTP), half relaxation time (1/2RT), maximum value of force derivative (dF/dt, -dF/dt) and Twitch Force (F_{Tw}) were measured from the direct and indirect twitch responses to characterize the contractile kinetics of the tested muscle.

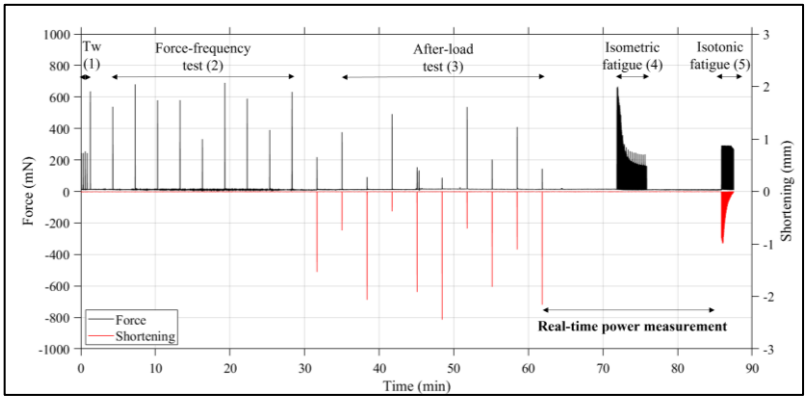

Figure 5. Example of the experimental protocol for the measurement of NMJ functionality: force (black) and shortening (red) values evoked for 5-month-old control mouse TA muscle, stimulated alternatively directly and indirectly [106].

After a resting period of 25 s, the muscle was stimulated with a series of 0.3 s pulse trains at a frequency ranging from 30 Hz to 150 Hz to compute the force-frequency curves for direct and indirect stimulations. In detail, the TA was subjected to the following sequence of stimulations: N90 (indirect stimulation through the nerve at 90 Hz), M60 (direct stimulation on muscle membrane at 60 Hz), N150, M120, N60, M30, N120, M90, N30, M150.This random order was chosen with the aim of avoiding muscle adaptation. A rest

time of 180 s was imposed before each stimulation to allow the muscle to completely recover its contractile capability. The third phase of the protocol started after a resting interval of 200 s and consisted in the application of the after-load technique in isotonic conditions for the measurement of muscle maximum power. A series of 0.3 s pulse trains at a frequency of 120 Hz was applied to the muscle through the nerve and on its membrane, simultaneously controlling the load that TA had to lift. The resistive load values were in the range of 10 to 80 % of maximum tetanic force, both for direct and indirect stimulations, in a random order to avoid muscle adaptation to increasing or decreasing loads. In detail, they were delivered in the following sequence: N30 (nerve stimulation at 30 % of resistive load), M60 (muscle membrane stimulation at 60 % of resistive load), N10, M80, N20, M10, N80, M30, N60, M20. It is worth noting that the resting times imposed before each stimulation, and in particular during this heavy stimulating paradigm, were chosen to guarantee that the muscle was always able to generate a maximum force comparable (i.e.>90 %) to the unfatigued one. Indeed, during this phase of the protocol, a resting period of 200 s was set before each stimulation. Hence, at the end of this phase, the software was programmed to compute the Hill's curve [35], the power-force curve and, therefore, the experimental optimal force (F_{exp}), namely the force at which the muscle was able to generate its maximum power. Indeed, after a resting period of 10 min, in the fourth part of the protocol the muscle was subjected to a fatigue test in isometric conditions, aimed at stressing the NMJ functionality [28]. In particular, the muscle was stimulated on its membrane with one 0.3 s pulse train at 120 Hz, followed by fourteen 0.3 s pulse trains at 120 Hz delivered through the nerve, interspersed with 0.7 s of rest. This sequence was repeated 16 times. In this part of the protocol, the Neurotransmission Failure and the Intratrain Fatigue were measured to evaluate the fatigue of synaptic transmission in isometric conditions, as known in literature [24], [30], [31]. After a resting interval of 10 min, the experimental protocol ended with the fatigue test in isotonic conditions, here proposed and developed for

the first time in literature. With the goal of stressing the junction but aiming also at the definition of a parameter that could represent the differences in control and pathological NMJ in an accurate and repeatable manner, we preliminary performed different tests by varying the number of pulse trains delivered through the sciatic nerve and the resting period after each isotonic phase. These preliminary tests suggested that the optimal isotonic fatigue protocol was characterized by one 0.3 s pulse train delivered on TA membrane, followed by three 0.3 s pulse trains applied through the sciatic nerve, with a resting period of 1.0 s. Indeed, in all the tests we conducted, the fatigue of synaptic transmission in indirect stimulation occurred earlier than in direct one. The frequency of the pulse train was set at 120 Hz for direct and indirect stimulations, and the muscle was allowed to shorten against a load equal to the experimental optimal force computed once the after-load phase was concluded [105]. An example of isotonic fatigue test for a wild-type TA is reported in Fig. 6. As can be seen, the experimental optimal force (F_{exp}) was higher than reference value (F_{ref}), equal to the 33 % of the tetanic force, both for direct and indirect stimulations. The fatigue test ended when the muscle was no longer able to shorten against the resistive load, and the fatigue time (T_{Fat}) was measured as the time necessary to fatigue the specimen. As previously said, this condition always occurred when stimulating the muscle through the nerve, as in the example of Fig. 6.

To characterize the NMJ transmission during the isotonic fatigue protocol, an innovative parameter, similarly to what has been done for the isometric fatigue [24], was devised, namely *Isotonic Neurotransmission Failure*:

$$INF = \frac{NS-MS}{1-MS}\% \qquad (1)$$

where *NS* and *MS* are the shortening decreases after nerve and muscle stimulation and were computed as the difference in maximum shortening between the first stimulation and the

subsequent ones, normalized on the maximum shortening generated at the first stimulation.

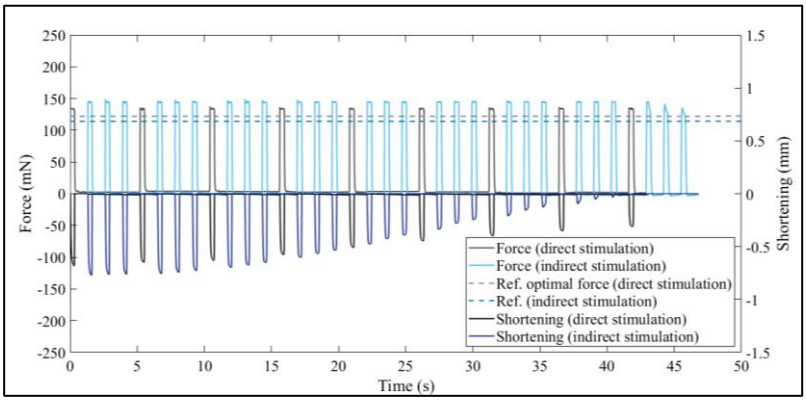

Figure 6. Example of isotonic fatigue protocol. Direct stimulation: F_{exp} = 133.59 mN (36.4 % of F_{Tet}); indirect stimulation: F_{exp} = 147.16 mN (42.8 % of F_{Tet}). The fatigue test ended when the muscle was not able to shorten following the indirect stimulation [106].

As regards the nerve stimulation, the *INF* was computed on the first pulse train immediately after the direct stimulation on muscle membrane. *INF* was computed at two different stages of the isotonic fatigue phase: in the middle (50 %) and shortly before (80 %) the end. Indeed, since the isotonic fatigue test ended when the muscle was no longer able to lift the resistive load, it was not possible to measure the *INF* at the end of the test (*INF*=100 %). To this, to increase the accuracy of *INF* it was necessary to determine in advance the timepoint at which it must be evaluated. Moreover, the power and work generated by the muscle during the fatigue test were computed as the sum of the product of the constant load for the highest shortening velocity and displacement during each direct and indirect shortening, respectively. Normalized power and work were obtained dividing maximum power and work by muscle mass, respectively.

First, this experimental technique and testing protocol were validated, in terms of measurement accuracy between direct and indirect stimulations, when computing all the parameters, both in

isometric and isotonic conditions [106]. Tab. 3 summarizes all the parameters measured during isometric tests. For these parameters, no statistically significant differences were obtained between the values measured when the TA muscles were stimulated directly and through the nerve. In addition, the coefficient of variation (CV) values measured for the direct and indirect stimulations were in good accordance with each other. In addition, it was measured a maximum average value NF equal to 41.21 ± 10.21 %, with a CV in agreement with the literature [107].

Table 3. Isometric test parameters. Kinetics contractile parameters (TTP, 1/2 RT, dF/dt), Twitch force (F_{Tw}), specific Twitch force (F_{Tw}/CSA), tetanic force (F_{Tet}), specific tetanic force (F_{Tet}/CSA), Intratrain Fatigue of Tibialis Anterior specimens in Wild-Type mice, stimulated on the muscle and through the nerve. Values are mean ± SD. n=8 [106].

	WT muscle	**WT nerve**
TTP (ms)	26.61 ± 7.72	25.91 ± 5.89
1/2RT (ms)	23.51 ± 8.54	24.59 ± 6.88
dF/dt (mN/ms)	10.70 ± 3.57	11.23 ± 3.80
F_{Tw} (mN)	156.20 ± 52.05	161.70 ± 50.05
F_{Tw}/CSA (mN/mm^2)	26.18 ± 9.51	26.93 ± 9.64
F_{Tet} (mN)	465.90 ± 125.40	485.90 ± 126.30
F_{Tet}/CSA (mN/mm^2)	77.64 ± 27.99	79.88 ± 22.18
IF (%)	85.03 ± 10.46	75.43 ± 11.98

An example of the Hill's curves and power curves normalized on muscle mass for a Wild-Type C57/BL6 (WT) TA muscle is shown in Fig. 7. Fig. 7a points out that the Hill's curve computed for the nerve stimulation was almost coincident to the one obtained for the direct stimulation. As a consequence, the maximum shortening velocity calculated through the nerve stimulation (47.00 mm/s) was highly close to the one obtained for the direct stimulation

(46.82 mm/s). In addition, results of the experimental and reference optimal force values for direct and indirect stimulations were in high accordance with those above obtained for the direct stimulation on WT TA muscle. Indeed, the maximum power was generated by the muscle at a force level higher than the reference one, equal to one-third of the corresponding tetanic force (F_{ref} = 33 % of F_{Tet}), both for direct and indirect stimulations (Fig. 7b).

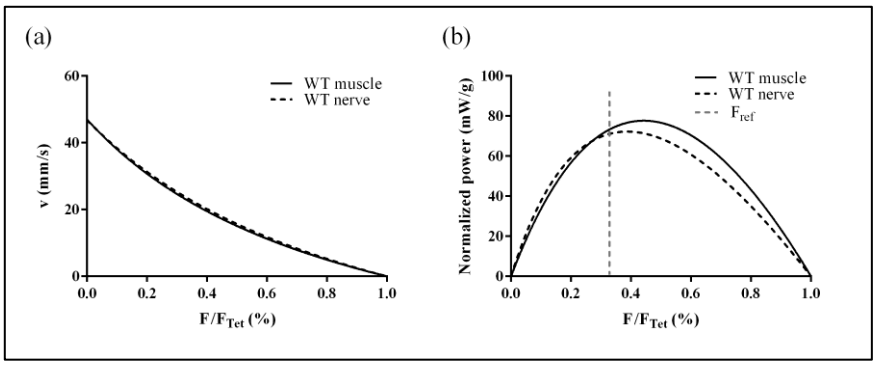

Figure 7. Example of (a) Hill's curves (F/F_{Tet} – v) and (b) normalized power (F/F_{Tet} – P/muscle mass) curves of one WT Tibialis Anterior muscle, for direct (muscle) and indirect (nerve) stimulations [106].

Tab. 4 reports the mean ± SD of the parameters obtained from the isotonic tests, namely after-load technique and isotonic fatigue test. For all the measured parameters, the CV obtained stimulating the specimen through the nerve was in high accordance with the corresponding one obtained for direct muscle stimulation. To evaluate the efficacy of the real-time measurement of maximum power, and therefore the determination of the experimental optimal force, we reported the measurement of the reference value of the optimal force for each muscle as one-third of the tetanic force, both for muscle and nerve stimulations. In accordance with the results obtained on WT mice TA muscles stimulated only directly [105], in all the experiments, the force value corresponding to the maximum power generated by the TA muscle, stimulated directly and indirectly, was higher than the theoretical one. On average, the

relative errors computed as the difference between the theoretical (F_{ref}) and experimental (F_{exp}) optimal force values normalized to the theoretical one ((F_{ref}-F_{exp})/F_{ref}) resulted equal to 18.21 and 24.25 %, for the direct and indirect stimulations respectively. Moreover, for the parameters obtained through the application of the isotonic fatigue test, no significant differences were reported between the values measured when stimulating the muscle through the nerve and on its membrane, as well as the CV computed in the two cases was in high agreement.

Table 4. Maximum power (P_{max}), normalized maximum power (P_{max}/m), maximum shortening velocity (v_{max}), experimental optimal force (F_{exp}) and reference optimal force (F_{ref}) of Tibialis Anterior specimens in Wild-type mice, measured through the after-load technique for muscle and nerve stimulations. Total power (P_{tot}), normalized total power (P_{tot}/m), total work (W_{tot}), normalized total work (W_{tot}/m) of Tibialis Anterior specimens in Wild-type mice, computed during the isotonic fatigue test, for muscle and nerve stimulations. Values are mean ± SD. n=8 [106].

	WT muscle	**WT nerve**
After-load test		
P_{max} (mW)	4.24 ± 2.08	5.21 ± 2.60
P_{max}/m (mW/g)	84.31 ± 37.10	101.70 ± 39.56
v_{max} (mm/s)	55.45 ± 15.58	59.40 ± 18.16
F_{exp} (mN)	184.40 ± 48.66	202.40 ± 43.96
F_{ref} (mN)	156.00 ± 41.69	162.90 ± 42.25
Isotonic fatigue test		
P_{tot} (mW)	25.55 ± 12.22	29.32 ± 11.57
P_{tot}/m (mW/g)	477.48 ± 170.68	553.64 ± 163.24
W_{tot} (mJ)	1.19 ± 0.54	1.41 ± 0.67
W_{tot}/m (mJ/g)	22.32 ± 7.80	26.65 ± 10.55

With the aim of deeply investigating the synaptic transmission in isotonic conditions, a novel parameter, called *Isotonic Neurotransmission Failure*, was also proposed. Fig. 8 shows an example of *INF* curves for TA muscle in WT (a) and SOD1^{G93A} (b) mice. It is possible to note a different trend of the *INF* curves between control and transgenic mice, thus pointing out that for SOD1^{G93A} TA muscles shortening decrease occurring during nerve stimulation was higher than the one obtained with muscle membrane stimulation from the beginning of the electrical stimulation, while for WT muscle this condition occurred about after half of the fatigue test.

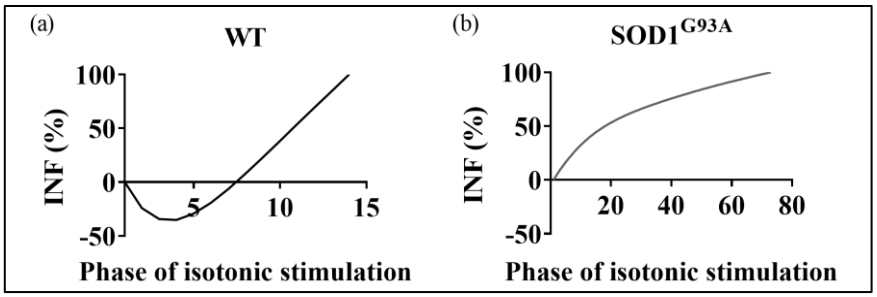

Figure 8. Example of *Isotonic Neurotransmission Failure* for TA muscle in WT (a) and SOD1^{G93A} (b) mice [106].

At this point, it has to be marked that this behaviour was a direct consequence of the proposed isotonic fatigue protocol, aimed at revealing impairments in the synaptic transmission, without over-stressing NMJ. In Fig. 9 it is reported the fatigue time (T_{Fat}) and the *Isotonic Neurotransmission Failure* computed at 50 and 80 % of the duration of isotonic fatigue test, for SOD1^{G93A} and WT mice. The fatigue time in transgenic muscles was significantly higher than the one measured in control ones, as well as the INF at 50 % and 80 %.

With the aim of studying the NMJ functionality in isotonic conditions during ALS progression, the *in-situ* technique was applied in TA-sciatic nerve preparations of SOD1^{G93A} mice at the presymptomatic, onset and end-stage of the disease and of age-matched WT ones.

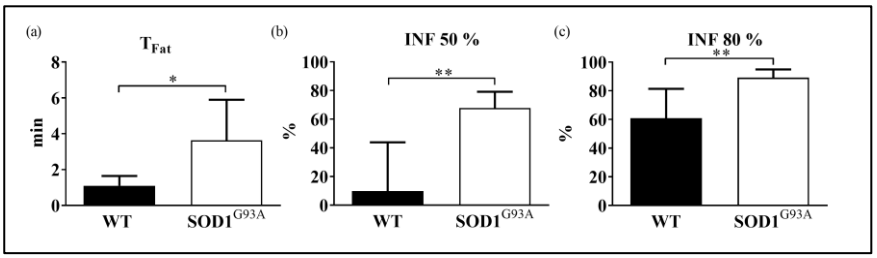

Figure 9. Fatigue time (T_{Fat}) (a) and *Isotonic Neurotransmission Failure* at 50 % (b) and 80 % (c) of isotonic fatigue test. Values are mean ± SD. n=7 for WT, n=5 for SOD1^{G93A}. *: p-value<0.05. **: p-value<0.01 [106].

Fig. 10 shows the mean values and SD of TA muscle mass and cross-sectional area (CSA) of SOD1^{G93A} mice at the presymptomatic, onset and end-stage of ALS progression and of age-matched WT mice. It is possible to note that mass and CSA of transgenic muscles were significantly lower than control ones, for all tested stages of ALS progression. Transgenic mice displayed a similar decrease in muscle mass at the presymptomatic (47 %) and onset stage (49 %), in comparison to age-matched control littermates. Consequently, a significant decrease of about 42 % and 44 % resulted in CSA of SOD1^{G93A} mice muscles, at the presymptomatic and onset stage, respectively, when compared to age-matched control muscles. In addition, a higher decrease resulted in SOD1^{G93A} mice TA mass and CSA at the end-stage of the disease, in comparison to the other disease stages. In particular, transgenic muscles showed a significant decrease of about 80 % in muscle mass, which resulted in a significant reduction of 67 % in CSA, in comparison to age-matched control samples.

The mean values and SD of rate of force production (dF/dt) and of force relaxation (-dF/dt) are shown in Fig. 11. It is possible to note that transgenic TA muscles displayed a strong decrease in contractile kinetics in comparison to control ones, at all tested stages of ALS progression. TA muscles of SOD1^{G93A} mice at the presymptomatic and onset stage reported a significant reduction in dF/dt in comparison to age-matched WT samples, for both kind of stimulation.

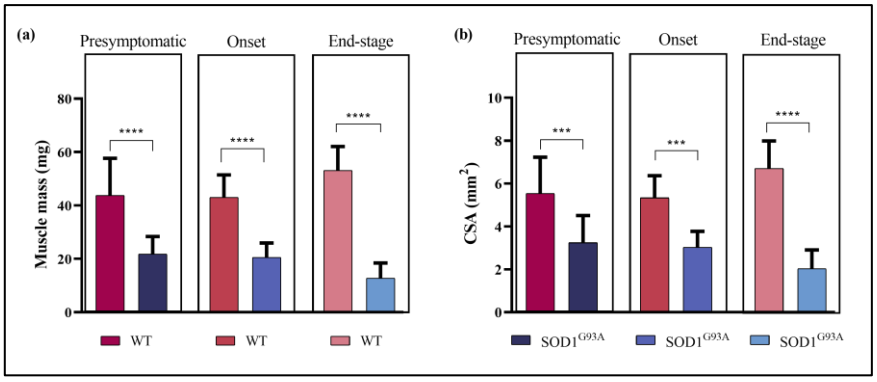

Figure 10. a) Muscle mass and b) Cross-sectional area (CSA) for TA muscles of SOD1^{G93A} mice at presymptomatic, onset and end-stage of ALS progression and age-matched WT ones. Values are mean ± SD. 9≤n≤16. ***: p-value>0.0005; ****: p-value<0.0001 "SOD1^{G93A}" vs "WT".

In particular, at the presymptomatic stage, dF/dt is equal to 4.04 ± 1.34 mN/ms and 3.68 ± 1.44 mN/ms in transgenic muscles, for direct and indirect stimulation, respectively, while it is equal to 8.37 ± 3.51 mN/ms and 8.93 ± 3.97 mN/ms in age-matched control muscles, for direct and indirect stimulations, respectively. On the other hand, at the onset stage, dF/dt is 4.04 ± 1.19 mN/ms and 3.82 ± 1.29 mN/ms in SOD1^{G93A} mice muscles, for direct and indirect stimulations, respectively, and it is equal to 9.77 ± 3.13 mN/ms and 11.55 ± 3.54 mN/ms in age-matched WT mice, for direct and indirect stimulations, respectively. At the end-stage of the disease, transgenic muscles showed a significant slowdown in dF/dt with a decrease of about 75 % when compared to control ones, when stimulated both on muscle membrane and through the nerve. In addition, a significant increase of dF/dt for control muscles at the presymptomatic stage is reported when stimulated indirectly in comparison to the onset and end-stage of the disease. Of note, a significant increase of dF/dt is reported for the direct stimulation in control mice between the presymptomatic and end-stage. On the other hand, a slight decrease of dF/dt is reported for SOD1^{G93A} mice

muscles during ALS progression, for both stimulations, even if not statistically significant.

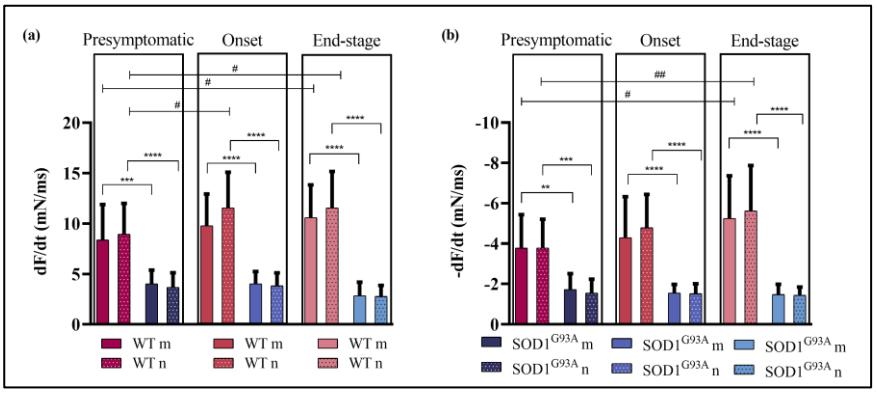

Figure 11. a) Rate of force production (dF/dt) and b) Rate of force relaxation (- dF/dt) for TA muscles of $SOD1^{G93A}$ mice at presymptomatic, onset and end-stage of ALS progression and age-matched WT ones. Values are mean ± SD. m is for muscle (direct stimulation), n is for nerve (indirect stimulation). $9 \leq n \leq 16$. **: $p<0.005$, ***: $p \leq 0.0005$, ****: $p<0.0001$, "$SOD1^{G93A}$ vs WT"; #: $p<0.05$, ##: $p<0.005$, "WT presymptomatic" vs "WT onset" and "WT presymptomatic" vs "WT end-stage".

Moreover, 3-way ANOVA revealed no significant differences in dF/dt between direct and indirect stimulations for transgenic muscle, even if at the presymptomatic stage a decrease in dF/dt was found when stimulated indirectly through the nerve and directly on membrane. Similar results were obtained for the rate of force relaxation (-dF/dt), as shown in Fig. 11b.

Fig. 12 shows the mean value and SD of tetanic force (F_{Tet}) and specific tetanic force (F_{Tet}/CSA) of transgenic and control muscle during ALS disease. As shown in Fig. 12a, for all tested ages, transgenic muscles generated a tetanic force lower than the one developed by control samples, both for direct and indirect stimulation. At the presymptomatic stage, tetanic force developed by $SOD1^{G93A}$ mice displayed a significant decrease of about 37 % for muscle stimulation and 49 % for nerve stimulation, when compared to age-matched WT littermates. Similarly, at the onset,

tetanic force generated by transgenic muscles showed a decrease of 60 % for direct stimulation and 66 % for indirect one, on average, in comparison to control samples. Moreover, at the end-stage a higher decrease in tetanic force generated by SOD1^{G93A} mice was observed in comparison to WT samples, both for direct and indirect stimulation. Transgenic muscles developed a maximum force 71 % and 76 % lower to control muscles for direct and indirect stimulations, respectively. Of note, a decrease in maximum force of about 17 % and 8 % was reported in SOD1^{G93A} mice muscles when stimulated indirectly in comparison to the direct stimulation at the presymptomatic and onset stage of the disease, respectively

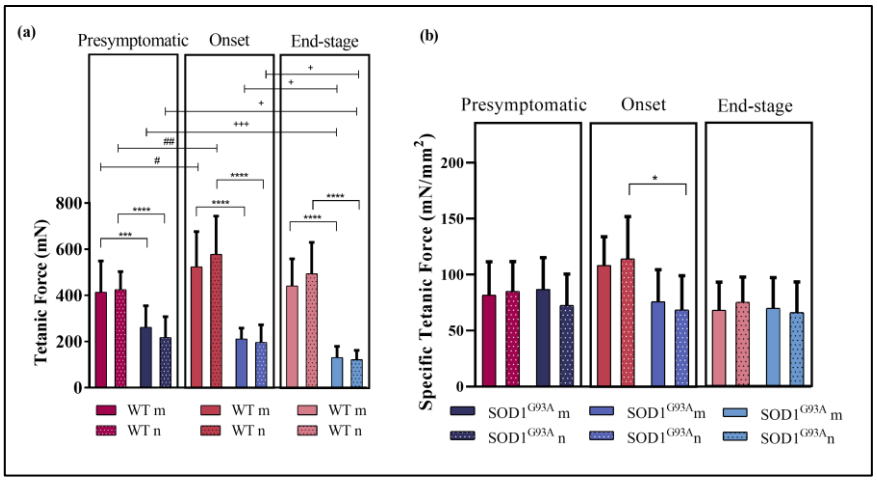

Figure 12. a) Tetanic force and b) Specific tetanic force for TA muscles of SOD1^{G93A} mice at presymptomatic, onset and end-stage of ALS progression and age-matched WT ones. Values are mean ± SD. m is for muscle (direct stimulation), n is for nerve (indirect stimulation). 9≤n≤16. *: p<0.05, ***: p<0.001, ****: p<0.0001, "SOD1^{G93A}" vs "WT". #: p<0.05, ##: p<0.005, for WT "presymptomatic" vs "onset"; +: p<0.05, +++: p<0.001, for SOD1^{G93A} "presymptomatic" vs "onset", "onset" vs "end-stage".

. In addition, SOD1^{G93A} mice displayed a significant reduction in tetanic force during ALS progression, both for direct and indirect stimulations.

As shown in Fig. 12b, a significant reduction was obtained in specific tetanic force, about 60 %, generated by SOD1^{G93A} mice TA muscles at disease onset, when stimulated indirectly, in comparison with age-matched WT ones.

Fig. 13 shows force-frequency curves, normalized on the tetanic force, at the presymptomatic, onset and end-stage of the disease, both for direct and indirect stimulation. It is possible to note that transgenic muscles were able to generate their maximum force at lower stimulation frequencies in comparison to control muscles, both for direct and indirect stimulation, regardless of ALS disease stage.

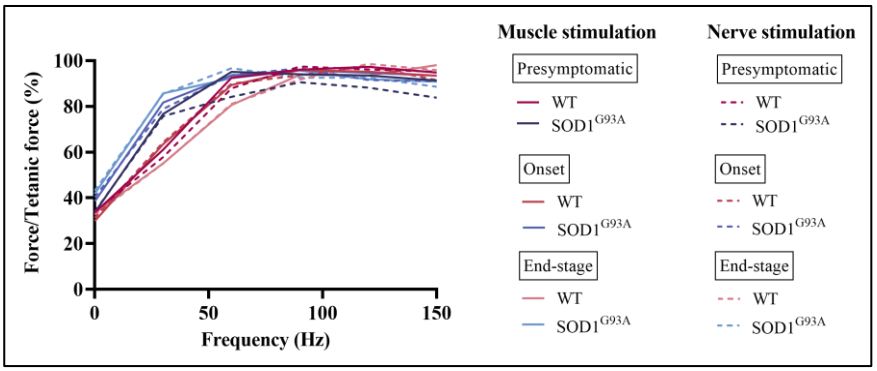

Figure 13. Force-frequency curves normalized on the tetanic force for TA muscles of SOD1^{G93A} and WT mice at presymptomatic, onset and end-stage of ALS progression, for direct and indirect stimulations. Values are mean. $9 \leq n \leq 16$.

For the after-load test, Fig. 14 shows the Hill's and power-force curves of TA muscles of SOD1^{G93A} mice at presymptomatic, onset and end-stage of disease and age-matched WT mice, both for muscle and nerve stimulation. For direct and indirect stimulations, shortening velocity and power of transgenic muscles were lower when compared to control samples, for all resistive loads and ages. Indeed, the maximum shortening velocity of TA muscles of transgenic and control mice, both for direct and indirect stimulation, is reported in Fig. 15.

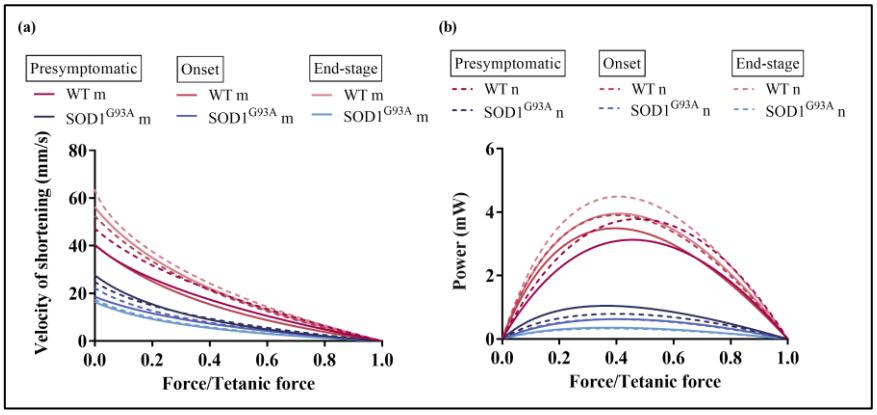

Figure 14. a) Hill's curves and b) power-force curves for TA muscles of SOD1^{G93A} mice at presymptomatic, onset and end-stage of ALS progression and age-matched WT ones, when muscle is stimulated directly and indirectly. m is for muscle (direct stimulation), n is for nerve (indirect stimulation). Values are mean. $9 \leq n \leq 16$.

As previously described, SOD1^{G93A} mice TA muscles generated a maximum velocity significantly lower than the one of WT littermates with the progression of ALS, both for direct and indirect stimulation. In particular, at the presymptomatic stage, SOD1^{G93A} mice muscles displayed a significant decrease of 45 %, on average, in maximum velocity in comparison to age-matched WT ones, when muscle was stimulated indirectly. At the onset and end-stage, maximum shortening of transgenic muscles significantly decreased when compared to control samples, both for direct and indirect stimulations. On the contrary, WT mice muscles reported a significant increase of maximum velocity with the progression of the disease, when muscle was stimulated directly and indirectly. As regarding the evaluation of the experimental optimal force, in all the experiments performed, the maximum power was generated by TA muscles of SOD1^{G93A} and WT mice at a force level higher than the reference one (33 %), both for direct and indirect stimulations (data not shown). Of note, in some experiments the experimental optimal force was quite close to the reference one (~37 %), while in other ones it resulted extremely higher than the reference one (~ 44%).

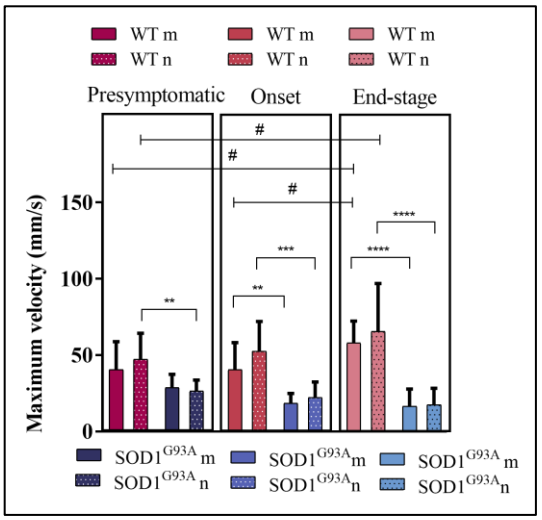

Figure 15. Maximum shortening velocity for TA muscles of SOD1^{G93A} and WT mice at presymptomatic, onset and end-stage of ALS progression. Values are mean ± SD. m is for muscle (direct stimulation), n is for nerve (indirect stimulation). 9≤n≤16. **: p-value<0.005, ***: p<0.001, ****: p<0.0001, "SOD1^{G93A}" vs "WT"; #: p<0.05, for WT "presymptomatic" vs "end-stage" and "onset" vs "end-stage".

For isometric fatigue phase, Fig. 16 shows the Neurotransmission Failure curves for each phase of stimulation and the maximum NF value for SOD1^{G93A} and WT mice TA muscles at the presymptomatic, onset and end-stage of the disease. NF values increased with isometric fatigue phases, both for SOD1^{G93A} and WT mice muscles, thus reaching a plateau at around the 11th phase of the test. At the onset stage, NF values were lower for SOD1^{G93A} model in comparison with WT ones. In fact, the extent of neurotransmission failure was higher for WT mice, in comparison to transgenic ones, even if not statistically significant, as shown in Fig. 16d. On the other hand, at the presymptomatic and end-stage, SOD1^{G93A} mice displayed higher maximum value of NF, not statistically significant, when compared to those of WT samples.

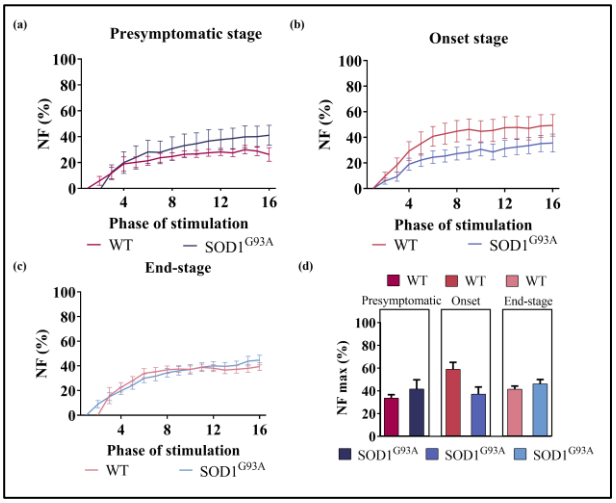

Figure 16. Neurotransmission failure curves computed for SOD1^{G93A} and WT mice TA muscles at the presymptomatic (a), onset (b) and end-stage (c) of the disease progression. d) Maximum value of NF. Values are mean ± SEM. $9 \leq n \leq 16$.

Fig. 17 shows the Intratrain Fatigue values for each phase of isometric fatigue protocol, for transgenic and control muscles during disease progression. At all tested ages, we obtained that IF decreased with the fatigue protocol for SOD1^{G93A} and WT mice. In accordance with NF values, at the onset stage, IF values were significantly lower for WT mice muscles than for SOD1^{G93A} ones, while at the other stages, there were no significant differences between transgenic and control muscles.

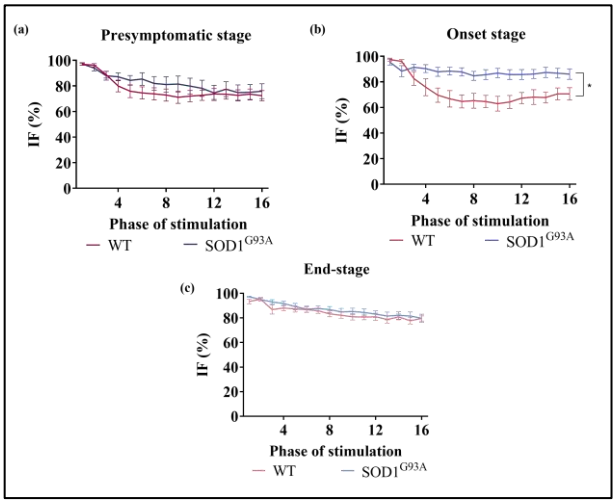

Figure 17. Intratrain Fatigue curves computed for SOD1^{G93A} and WT mice TA muscles at the presymptomatic (a), onset (b) and end-stage (c) of the disease progression. Values are mean ± SEM. 9≤n≤16. *: p-value<0.05.

As regarding isotonic fatigue test, Fig. 18 shows an example of power and work curves for TA muscles of SOD1^{G93A} mice at the presymptomatic, onset and end-stage of the disease and of age-matched WT ones. It is possible to note that the trend of isotonic power and work is very different between transgenic and control muscles, both for direct and indirect stimulations, at all tested ages.

In particular, in the first phases of isotonic protocol, control mice muscles were able to generate higher values of power and work, in comparison with transgenic ones, thus fatiguing earlier than SOD1^{G93A} samples. On the contrary, SOD1^{G93A} mice muscles generated lower values of power, compared to control ones, thus maintaining power for more time. For example, at the onset stage, WT muscle was no longer able to shorten against the resistive load when stimulated indirectly after 10 phases of stimulation (i.e. 16 s), while for SOD1^{G93A} muscle this occurred after 127 phases (i.e. 203 s) of stimulation, as shown in Fig. 18b and 18e.

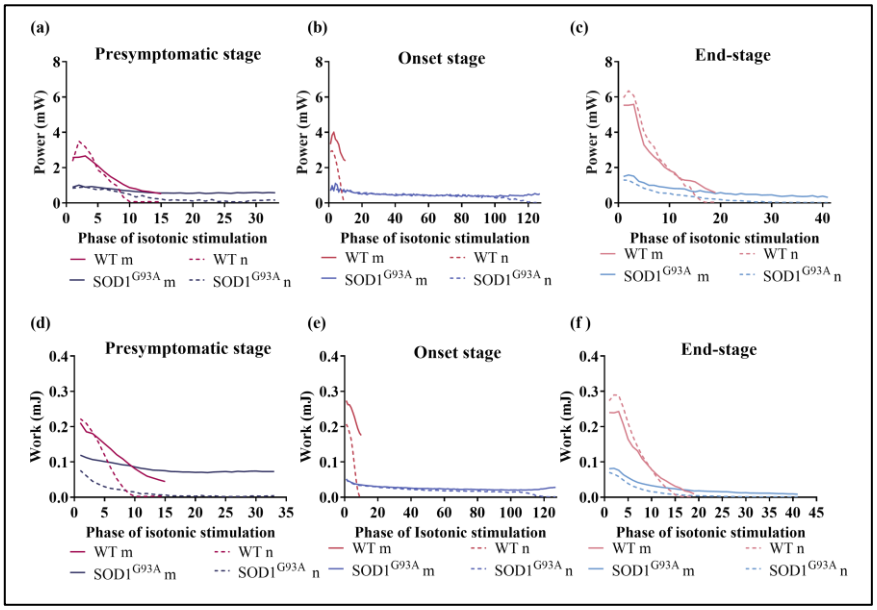

Figure 18. Example of power and work curves for TA muscles of SOD1^{G93A} at presymptomatic, onset and end-stage and of age-matched WT samples. m is for muscle (direct stimulation), n is for nerve (indirect stimulation). Values are mean.

Fig. 19 reports the mean values and SD of fatigue time and *INF* at 80 % of isotonic fatigue test computed for TA muscles of SOD1^{G93A} mice at presymptomatic, onset and end-stage of ALS and of age-matched WT ones. At all tested stages of ALS, control samples fatigued earlier than transgenic ones, even if not significantly, in accordance with power and work curves showed above (Fig. 19a). However, even if SOD1^{G93A} mice muscles displayed a greater resistance to fatigue, they underwent a bigger impairment in the synaptic transmission, in comparison with control samples, as shown in Fig. 19b. In particular, SOD1^{G93A} muscles showed a significant increase of about 30 % in *INF* at the end-stage, in comparison with age-matched WT samples.

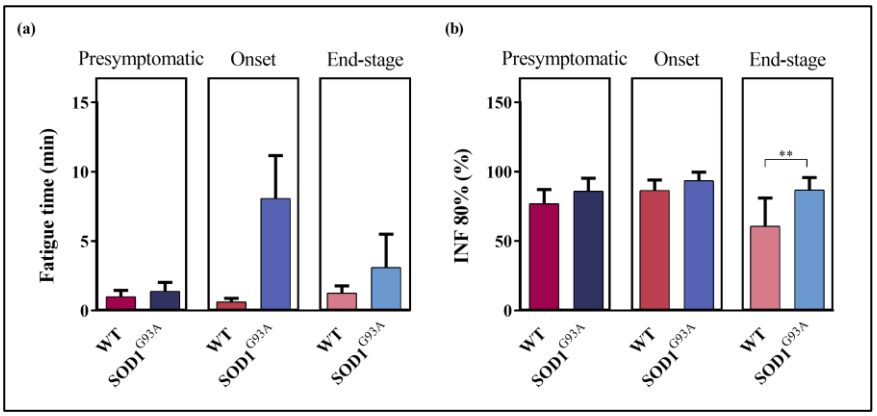

Figure 19. a) Fatigue time and b) *Isotonic Neurotransmission Failure* for TA muscles of SOD1^{G93A} and WT mice at presymptomatic, onset and end-stage. Values are mean ± SD. 3≤n≤6. **: p-value<0.01.

4.1.2. 3D embedded system for the measurement of engineered skeletal muscle contractile force

An embedded sensor for the measurement of *ex-vivo* engineered muscle tissue's (X-MET [50]) contractility during its growth by using an optical tracking method was designed and realized, as shown in Fig. 20 [108]. Typically, the muscle engineered tissue growths between two fixed pins, and the idea behind the development of the measurement system was based on the possibility to measure the calibrated deflection of one of the two pins, which was therefore designed with specific dimensions and compliance. The sensor was realized in plexiglass and stainless steel to allow for the sterilization by ultraviolet (UV) light. The dimensions of the entire device were set at 50x45x8 mm to be placed in a 90 mm Petri dish to allow for the contractility monitoring during the entire growing phase of the tissue in the incubator. The sensor was composed of a central groove with dimensions of 40x20x4 mm coated with silicon (Sylgard 184, Dow Corning) to allow for the accommodation of the X-MET.

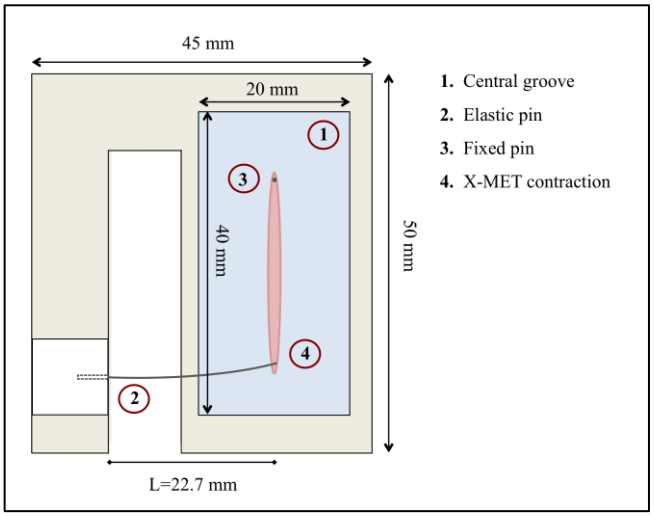

Figure 20. Schematic of the sensor (top view) for the measurement of X-MET contractile force [108].

In detail, one of its ends was pinned to the silicone substrate, while the other end was linked to the calibrated pin held horizontally by a specific support. Indeed, the base concept of the measurement system was to let the tissue continuously growth within this device, and then take advantage of an optical tracking algorithm to measure the deflection of the compliant pin during tissue contraction, whether this was spontaneous or obtained through electrical stimulation. Of note, this procedure avoided to detach the tissue from the supporting pin to link it to the force transducer. The dimensions and the mechanical properties of the elastic pin were chosen according to theoretical considerations [109]. In details, the behaviour of the elastic pin was approximated to that of a cantilever subjected to bending. Considering a circular pin with a radius of R=0.15 mm and a Young modulus of E=169 GPa (from datasheet), we designed the length of the elastic pin L to have a deflection of its tip in the range 5-50 μm according to the following equation:

$$k = \frac{3EI}{L^3} \qquad (2)$$

where *I* is the moment of inertia for a circular pin and *k* is the elastic constant, given from the ratio between the force developed by the tissue and the pin tip displacement. Of note, the range 5-50 μm was chosen taking into consideration the force values usually generated by these tissues during spontaneous contraction and electrical stimulation [52] and those expected to be generated by the treated samples when inducing to simulate an aged microenvironment, as suggested by the literature [110], [111]. The needs of the optical tracking method were also taken into consideration, on the basis of different validation tests performed in our previous works [109], [112]. The elastic constant resulted k= 20 N/m for a pin length of L=22.7 mm.

Fig. 21 shows the linear regression test performed for the calibration of the elastic pin. The experimental value of the elastic constant, computed as the curve slope, was equal to 19.51 N/m, a value close to the theoric one (20 N/m), with a determination coefficient (R^2) equal to 0.992.

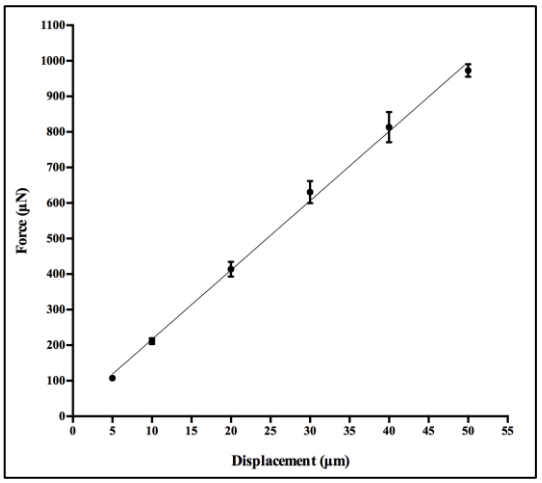

Figure 21. Linear regression for the force values measured by the micro-force transducer during the pin calibration procedure. Values are mean ± SD [108].

For the evaluation of the Region of Interest (ROI) positioning, and therefore for the measurement of X-MET contractile force by

the optical tracking method [112], the relative percentage errors were first computed among the 15 nodes of the central ROI (ROI C) for the two tested displacements. The relative error was equal to 2.24 ± 0.33 % and 1.81 ± 1.18 %, for a nominal displacement of 5 µm and 10 µm, respectively. Indeed, the relative error was always lower than 4 % and the highest value occurred for the smallest nominal displacement of 5 µm. Moreover, for both displacements, the relative error values were positive, thus pointing out that the optical tracking algorithm overestimated the displacement of the nodes of the central ROI.

Fig. 22 shows the mean values and SD of the errors relative to the displacement measured for the central ROI for all the tested positions of the ROI and for the two nominal displacements. The trend of the relative error was very similar for the two displacement conditions, as a function of the ROI positioning along the elastic pin.

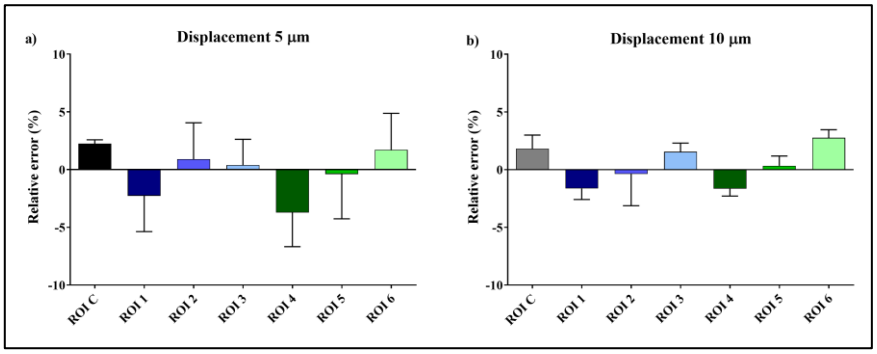

Figure 22. Relative percentage error for all the ROI positionings along the elastic pin, for a nominal displacement of 5 µm (a) and 10 µm (b). Values are mean ± SD. n=5 [112].

A good correspondence of the relative error sign for the tested ROI positionings between the two displacements was also reported, except for ROI 2 and ROI 5 in which, however, the average errors were close to zero but with high value of SD. The lower errors were obtained for the highest displacement of 10 µm, while for 5 µm the mean values and the standard deviations increased for all the

different positionings of the ROI. In particular, the optical tracking algorithm provided the highest relative error for ROI 4 when a nominal displacement of 5 μm was imposed, and it is equal to -3.72 ± 2.96 %. On the contrary, when the ROI was placed in correspondence of ROI 5, the lowest relative error was obtained (0.33 ± 0.84 %).

Tab. 5 summarizes all the parameters measured during the twitch test for both control and treated X-METs across the five days of acquisition. One-way ANOVA revealed that the specific twitch force (F_{TW}/CSA) developed by the treated X-METs was significantly affected by the *day* factor, and the Tuckey's multiple comparison tests revealed a significant decrease of force at day 2, day 3 and day 4 in comparison with day 0.

Table 5. Kinetics contractile parameters (TTP and 1/2RT) and specific twitch force (F_{TW}/CSA) in control and treated X-METs for the five days of acquisition. Values are mean ± SD. n=5 for control X-MET, n=4 for treated X-MET. **: p-value<0.01, ***: p-value<0.001 vs. treated X-METs. $^{+}$: p-value<0.05 vs. day 0 [108].

	TTP (ms)		**1/2RT (ms)**		**F_{TW}/CSA (mN/mm^2)**	
	Control	**Treated**	**Control**	**Treated**	**Control**	**Treated**
Day 0	40.7 ± 8.9	42.5 ± 5.0	59.3 ± 18.2	57.5 ± 12.6	0.7 ± 0.5	0.5 ± 0.3
Day 1	34.0 ± 8.0	32.2 ± 1.9	70.0 ± 9.4	45.0 ± 16.6	1.6 ± 0.7 ***	0.3 ± 0.3
Day 2	47.3 ± 13.2	35.0 ± 16.6	72.0 ± 16.8	70.0 ± 18.8	0.8 ± 0.6	0.1 ± 0.1 $^{+}$
Day 3	41.3 ± 10.7	50.0	64.7 ± 16.4	73.3	1.1 ± 0.5 **	0.0 ± 0.1 $^{+}$
Day 4	37.7 ± 18.2	13.3	64.0 ± 17.5	16.7	1.3 ± 0.5 **	0.1 ± 0.1 $^{+}$

On the contrary, no significant alterations in TTP, 1/2RT and specific twitch force across the five testing days in control group were found. In addition, two-way ANOVA showed that both the *day*

and *treatment* factors significantly affected the specific twitch force. Post-hoc tests also highlighted a significant difference between the control and treated X-METs on day 1, day 3 and day 4.

The maximum specific tetanic force of control and treated X-METs along the five days is shown in Fig. 23. No significant differences in the tetanic specific force developed by control X-METs across the five days were found. On the contrary, one-way ANOVA applied to the treated group revealed a significant influence of the *day* factor on the maximum specific force. The two-way ANOVA revealed that only the factor *treatment* significantly affected the maximum specific force. Fisher's multiple comparison test also showed significant decreases in the maximum specific tetanic forces developed by the treated X-METs when comparing with those developed by the control specimens for all the testing day, except for the initial one.

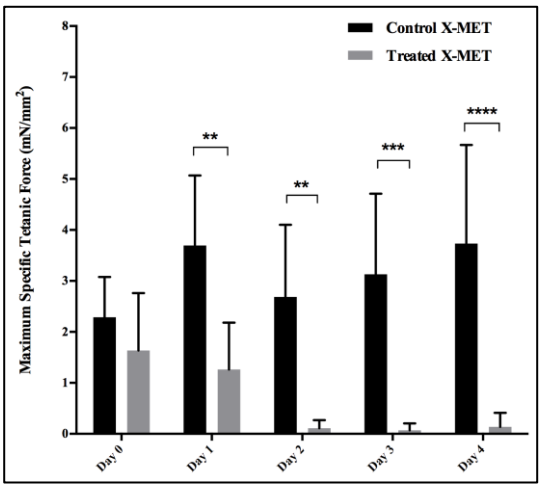

Figure 23. Maximum specific tetanic force developed by control and treated X-METs along the five days of experiment. Values are mean ± SD. n=5. **: p-value<0.01. ***: p-value<0.001. ****: p-value<0.0001 [108].

This latter point also confirmed that the treated specimens were as good as the untreated ones before the beginning of the treatment.

4.1.3. 3D microfluidic device for the formation of neuromuscular junction

As concerning the potential of the X-MET to be used for the generation of a 3D neuromuscular junction model, preliminary data demonstrated the presence of Ach-receptor β1 (AChR- β1) and β2 (AChR-β2) along the X-MET's structure, as shown in Fig. 24. In particular, one-way ANOVA test revealed the significant presence of Ach-β1 on the three-dimensional construct after 15 days in Differentiation Medium (DM), as shown in Fig. 24.

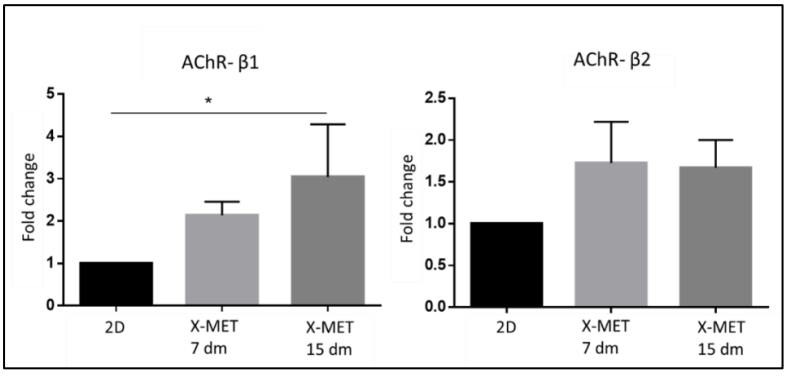

Figure 24. RT-PCR for AChR-β1 and AChR-β2 comparing 2D primary culture cells and 3D X-MET after 7 and 15 days in Differentiation Medium (DM). Values are mean ± SD.*: p-value<0.05.

In addition, preliminary co-cultures between X-MET (after 15 days in DM) and a murine embryonic spinal cord explant showed a good attraction between the two components. Immunofluorescence analysis showed a good co-localization of spinal cord and myosin cells (Fig. 25A and 25B), as well as of Smi-32 with Myosin Heavy Chain proteins to evaluate the presence of adult neurons and the incorporation on engineered skeletal muscle (Fig. 25C). In view of this, RT-PCR analysis revealed the significant up-regulation of mature AChRs (AChR-ε) on the X-MET structure co-cultured with the ventral spinal cord explant (Fig. 25D).

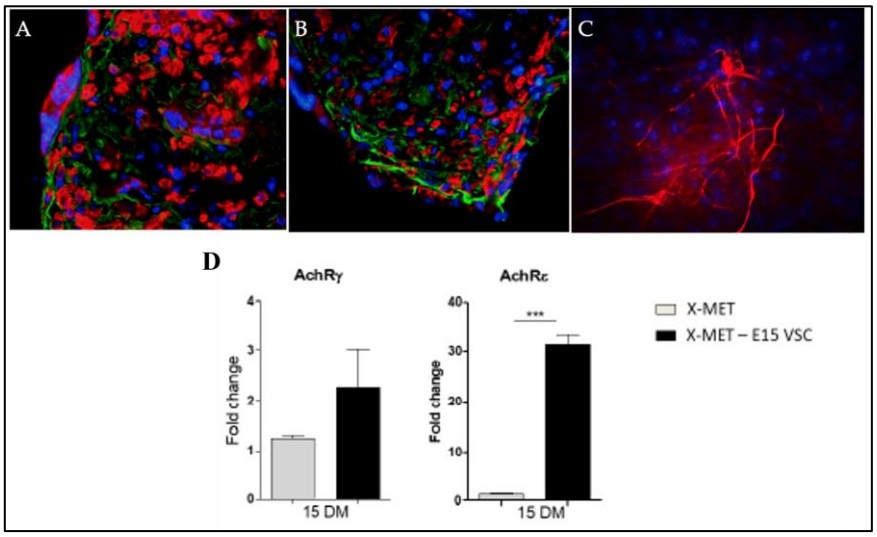

Figure 25. A), B) Immunofluorescence analysis for MyHC, GFP and Hoechst expression on cross section of X-MET after 10 days in co-culture with murine emrbyonic spinal cord explant. C) Immunofluorescence analysis performed on cross section of X-MET-Spinal cord explant for Smi-32 and Hoechst. D) RT-PCR for AChR subunits in X-MET and co-cultured X-MET. ***: p-value<0.001. n=3.

By using a commercial two-dimensional (2D) microfluidic device for the formation of NMJ, co-culture experiments with spinal cord-derived cells and the 2D population of X-MET revealed a good connection between the two compartments (Fig. 26a) and that the 60 % of neurofilaments outgrowth along the microchannels (Fig. 26b).

On this basis, we designed and realized a three-dimensional microfluidic device to promote the formation of NMJ between X-MET and mouse embryonic spinal cord primary culture. It was realized by photolithography and a polydimethylsiloxane (PDMS) stamp was used to generate the chambers required for the accommodation of the X-MET and spinal cord cells (Fig. 27a).

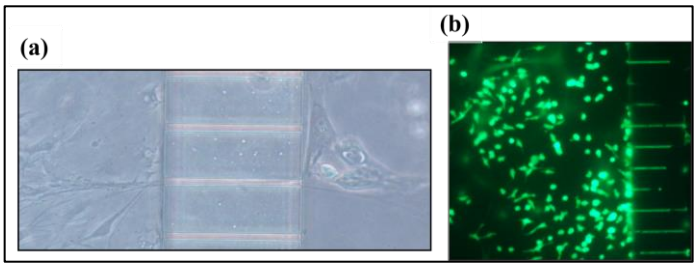

Figure 26. a) Transmission and b) GFP^+ mouse spinal cord-derived cells of compartmentalized PDMS chambers of 2D microfluidic device separated by functional microgrooves. Magnification 20X (a) and 40X (b).

The device was designed as two distinct compartments connected by a series of microchannels. The first compartment was composed by a pair of circular chambers for spinal cord-derived cells culture connected through a central groove, and the second one was made of a rectangular chamber for muscle engineered tissue placement.

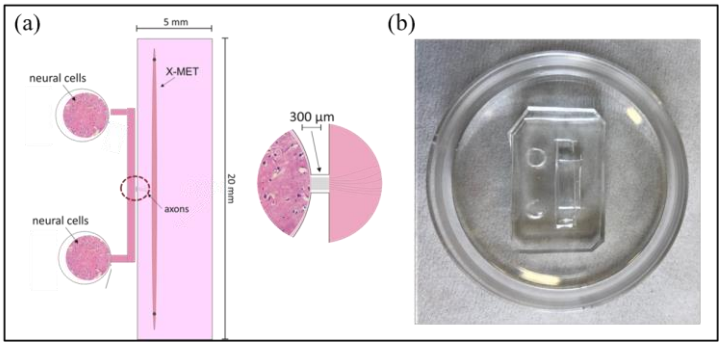

Figure 27. a) Schematic (top view) and b) picture of the 3D microfluidic device for the formation of NMJ between X-MET and neuronal cells.

. The microchannels between the two compartments acted as a mechanical filter, allowing the transfer of neuritic processes towards the other side of the device, excluding cell bodies of dimensions higher than those of microchannels. The resulting design allowed motor neuronal cells and muscle engineered tissue to grow in two different chambers, being connected only by the axons formed in the

microchannels. All the dimensions were defined according to those of 2D and 3D commercial and custom-made microfluidic devices [113], [114]. The entire structure was realized in silicone with a dimension of 30 mm x 20 mm x 5 mm for length, height and depth, respectively. The two chambers for neuronal cells culture were modelled as a cylinder of radius and height equal to 2.2 mm and 5 mm, respectively. The lateral and central grooves were realized with a depth of 0.1 mm, starting from the bottom of the device. In particular, the central groove was 1.5 mm wide and 7 mm long. The entire microgroove barrier was 1.57 mm wide, 300 µm long and 5 µm high and it was composed by 40 microchannels of 10 µm wide, distant from each other 30 µm. Finally, the chamber for muscle engineered tissue culture was modelled with the following dimensions: 20 mm of length, 5 mm of height and 5 mm of depth, to allow the muscle engineered tissue to be pinned inside.

Fig. 28 shows an immunofluorescence analysis of a co-culture obtained with a prototype of the microfluidic device. GFP^+ mouse was used for both X-MET and murine embryonic spinal cord cells and the picture was taken after 10 days of co-culture. Results demonstrated that 4 neurofilaments reached the 90% of microchannels' length.

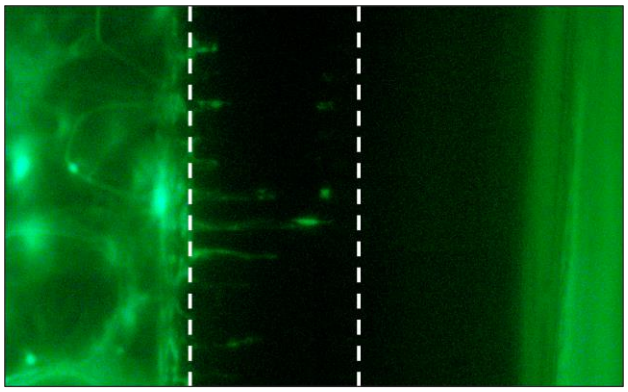

Figure 28. Immunofluorescence analysis for GFP^+ spinal cord-derived cells (left compartment) and X-MET (right compartment). Magnification 10X.

With the aim of promoting as much as possible the outgrowth of neurofilaments along the microchannels, we considered the electrical stimulation on neuronal cells. First, a simulation of electric field distribution on the 3D microfluidic device was performed to obtain the best electrodes' configuration [115] by using CST Studio Suite 2019 software. Fig. 29 shows the results of the simulation tests of electric field intensity generated by cylindrical pin electrodes (a), O-ring electrodes (b) and cylindrical disc electrodes (c) along the central groove of 3D microfluidic device for the tested values of radius, position in the neuronal chambers and applied voltage.

For all the types of electrodes, the magnitude of the electric field increased with the applied potential and the trend of the mean values was very similar for all the tested positions as a function of pin dimensions and voltage tested. For cylindrical pin electrodes (Fig. 29a), 2-way ANOVA revealed that the electrodes placed on the internal position were able to generate an electric field significantly higher than that generated by the pin located on all the other positions, for both radii and all voltage intensities. Moreover, for all the positions and potentials investigated, the electric field generated by the 0.3 mm radius electrodes was significantly higher than that delivered by the pin with a radius of 0.2 mm. On the other hand, no significant differences were revealed in the electric field generated by the electrodes located on high-centre and external of neuronal chambers for both radii and for all the potential intensities. The maximum electrical field induced along the central groove of the microfluidic device, when applying a potential of 8 V, was 184.70 ± 0.90 V/m and 186 ± 0.92 V/m for 0.2 mm and 0.3 mm pin radius, respectively. On this basis, the best condition that allowed to induce the highest electric field was represented by the pin electrodes of 0.3 mm radius, located symmetrically on the internal position of the neuronal chambers, with a voltage of 8 V.

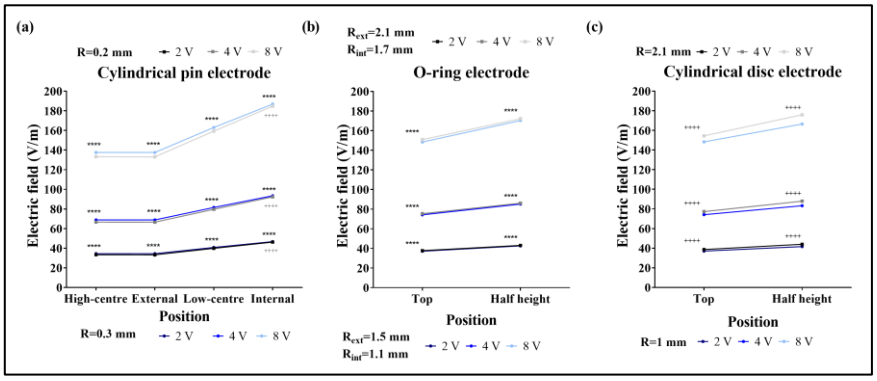

Figure 29. Electric field intensity generated by a pair of cylindrical pin electrodes (a), O-ring electrodes (b) and cylindrical disc electrodes (c) along the central groove of the 3D microfluidic device, by varying the size, the position in the neuronal chambers and the applied potential. Values are mean ± SD. a) ****: p-value < 0.0001 "R=0.2 mm" vs "R=0.3 mm". ++++: p-value < 0.0001 vs "Internal". b), c) ****: p-value < 0.0001 "R_{ext}=2.1 mm, R_{int}=1.7" vs "R_{ext}=1.5 mm, R_{int}=1.1 mm". ++++: p-value < 0.0001 "R=2.1 mm" vs "R=1 mm" [115].

As shown in Fig. 29b and 29c, a voltage of 8 V was able to induce the maximum electric field, equal to 172.22 ± 0.94 V/m and 175.93 ± 0.90 V/m for O-ring and cylindrical disc electrodes, respectively, when they were placed at half height of neuronal chambers. In view of this, the optimal electrode configuration able to induce the highest electric field along the central groove without damaging neuronal cells was represented by 0.3 mm cylindrical pin electrodes, located symmetrically on the internal position, with a voltage of 8 V.

The electric field distribution along the 3D microfluidic device simulated for the best electrodes configuration is shown in Fig. 30. It is possible to note that the electric field propagated symmetrically with maximum values closer to the electrodes, thus attenuating from the end of the lateral channels. Interestingly, the electric field was almost constant along the central groove, with a coefficient of variation (CV) lower than 0.5 %.

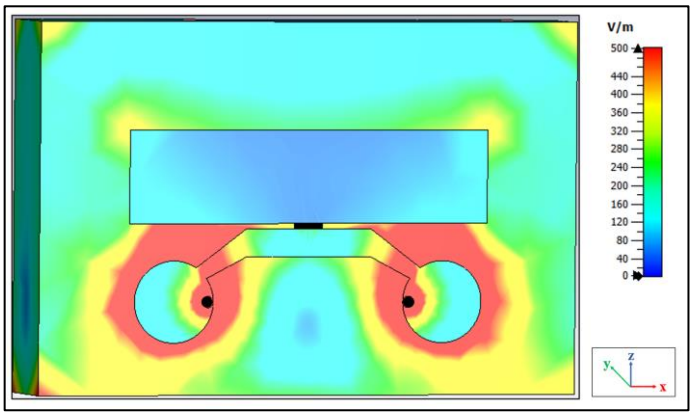

Figure 30. Simulation of the electric field distribution over the entire microfluidic device for the optimal electrodes' configuration [115].

With the aim of promoting NMJ formation in the 3D microfluidic device by using electrical stimulation on neuronal cells, spinal cord-derived cells were first stimulated with the best electrodes' configuration in Petri dishes of 35 mm. Results of electrical stimulation (ES) protocol are shown in Fig. 31, in terms of mean values and SD of number of nuclei and neurofilaments' elongation. One hour of electrical stimulation significantly increased the number of nuclei of around 280 % and 163 % in comparison with control conditions, for 24 and 48 hours after ES, respectively. In parallel, 24 hours later the end of ES, neurofilaments' length increased in comparison to control samples, for all the tested conditions. On the contrary, 48 hours later the ES axons' elongation decreased in comparison to control condition, even if the differences were not statistically significant, both for 1 hour and 2 hours of stimulation.

Fig. 32 shows the confocal microscopy analysis of a pilot experiment of co-culture between X-MET and GFP^+ mouse spinal cord-derived cells in the 3D microfluidic device, performed 10 days after the ES on neuronal cells. Due to the conformation of the device, it was not possible to clearly observe the X-MET (right side) at the microscopy.

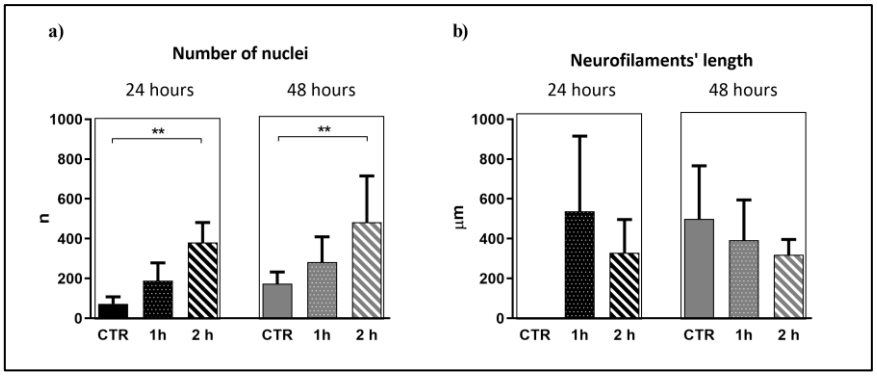

Figure 31. a) Number of nuclei and b) Neurofilaments' length of spinal cord-derived cells after electrical stimulation of 1 hour and 2 hours, 24 and 48 hours later the end of ES protocol. Values are mean ± SD. $3 \leq n \leq 10$. **: p-value<0.05.

However, results showed that ES yielded to an increase of most neurofilaments', allowing them to cross the microchannels and to reach the right side of the 3D device. Of note, on the basis of these results a new device will be designed to overcome this "optical" issue, by decreasing its wide to avoid as much as possible the penumbra zone resulted at the microscopy.

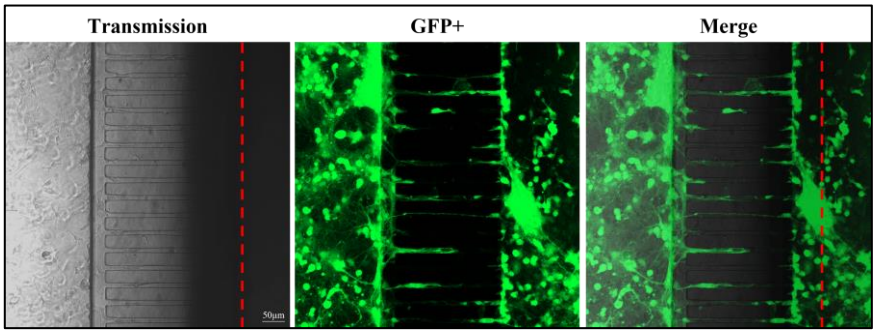

Figure 32. Immunofluorescence analysis for GFP^+ spinal cord-derived cells (left compartment) and X-MET (right compartment). Red dashed line represents the X-MET. Scale bar 50 µm. Magnification 10X.

4.2 Molecular characterization and functional effects of SOD1^{G93A} mouse extracellular vesicles on C2C12 cell line

4.2.1. Number of SOD1^{G93A} mouse extracellular vesicles

The mean values and standard deviation (SD) of the number of EVs derived from SOD1^{G93A} mice sera at the presymptomatic, onset and end-stage of ALS progression and from age-matched Wild Type C57/BL6 (WT) mice ones, normalized on the maximum value of the age-matched WT samples, are shown in Fig. 33. For the presymptomatic and onset stages of ALS progression, a significant difference in the number of EVs was reported in SOD1^{G93A} mice, in comparison with age-matched WT littermates.

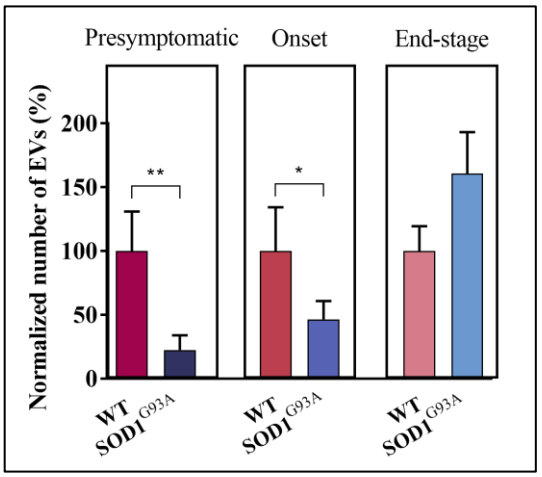

Figure 33. Normalized number of EVs in SOD1^{G93A} mice at presymptomatic, onset and end-stage of ALS and in age-matched WT mice. Values are mean ± SD. 3≤n≤6. *: p-value<0.05; **: p-value<0.01.

While at the presymptomatic and onset stage of ALS, SOD1^{G93A} mice displayed a significant decrease in the number of EVs of 78 % and 54 %, on average, in comparison with age-matched WT samples, at the end-stage the normalized number of EVs was higher

(+60 %), even if not statistically significant, in transgenic mice in comparison to WT samples.

4.2.2. Uptake of SOD1^{G93A} mice-derived extracellular vesicles by C2C12 cell line

Fig. 34 shows the confocal microscopy analysis performed on C2C12 cells in proliferation after being treated for 6 hours with CFSE^{+} EVs derived from SOD1^{G93A} mice at presymptomatic, onset and end-stage and from age-matched WT samples.

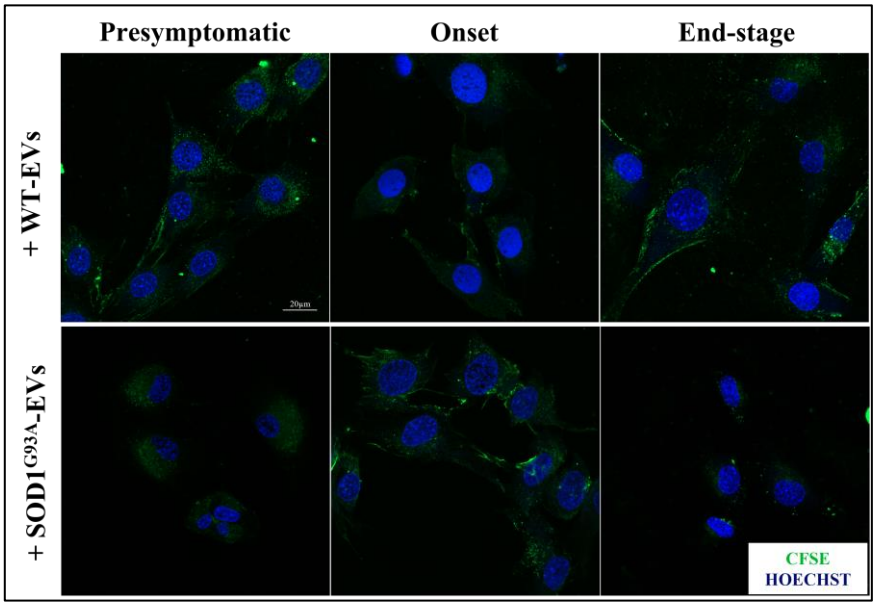

Figure 34. Confocal microscopy analysis of C2C12 cells in proliferation treated for 6 hours with CFSE^{+} EVs derived from SOD1^{G93A} mice (+SOD1^{G93A}-EVs) at presymptomatic, onset and end-stage and from age-matched WT littermates (+WT-EVs). Nuclei were stained with Hoechst (blue). Scale bar: 20 µm. Magnification 40X.

As shown in Fig. 34, it is possible to note a different efficiency of fusion among EVs collected from transgenic and control mice, except for the presymptomatic stage. Indeed, this qualitative data

was largely supported by the mean fluorescence intensity (MFI) analysis of $CFSE^+$ C2C12 cells in proliferation after 6 hours of treatment with $CFSE^+$ EVs derived from transgenic and control mice at the three different ALS stages, shown in Fig. 35. While at the presymptomatic stage, no significant differences were revealed in MFI between cells treated with control and transgenic-derived EVs (Fig. 35a), at the onset and end-stage of ALS, a significant difference in the MFI was reported between proliferating cells treated with EVs derived from $SOD1^{G93A}$ and WT mice (Fig. 35b, 35c). In particular, at the onset of ALS, $SOD1^{G93A}$ mice-derived EVs were able to fuse to target cells with a significant higher efficiency (+40 %) in comparison to control samples. On the other hand, at the end-stage of the disease, transgenic mice-derived EVs displayed a significant decrease of 36 %, on average, in MFI, when compared to control mice-derived EVs.

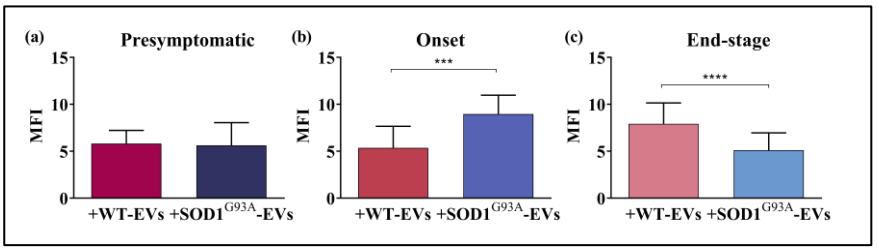

Figure 35. Mean Fluorescence Intensity (MFI) quantification of $CFSE^+$ C2C12 cells in proliferation after 6 hours of treatment with $CFSE^+$ EVs derived from $SOD1^{G93A}$ mice at presymptomatic (a), onset (b) and end-stage (c) of ALS progression and from age-matched WT littermates. Values are mean ± SD. $10 \leq n \leq 20$. ***: p-value<0.0005; ****: p-value<0.0001.

Similarly, the uptake of $CFSE^+$ EVs derived from $SOD1^{G93A}$ mice at presymptomatic, onset and end-stage and from age-matched WT mice by C2C12 cells completely differentiated in myotubes, after 6 hours of treatment, was evaluated. Confocal microscopy analysis and MFI analysis of C2C12 cells completely differentiated in myotubes treated for 6 hours with $CFSE^+$ EVs derived from $SOD1^{G93A}$ mice sera at presymptomatic, onset and end-stage and from age-matched WT samples are shown in Fig. 36. By MFI

analysis, after 6 hours of treatment WT mice-derived EVs were able to fuse to the target cell with a higher efficiency in comparison with SOD1^{G93A} mice-derived EVs at the presymptomatic, onset and end-stage of ALS progression. In particular, at the onset stage, it was obtained a significant decrease of about 34 % in MFI of SOD1^{G93A} mice-derived EVs, when compared to WT ones.

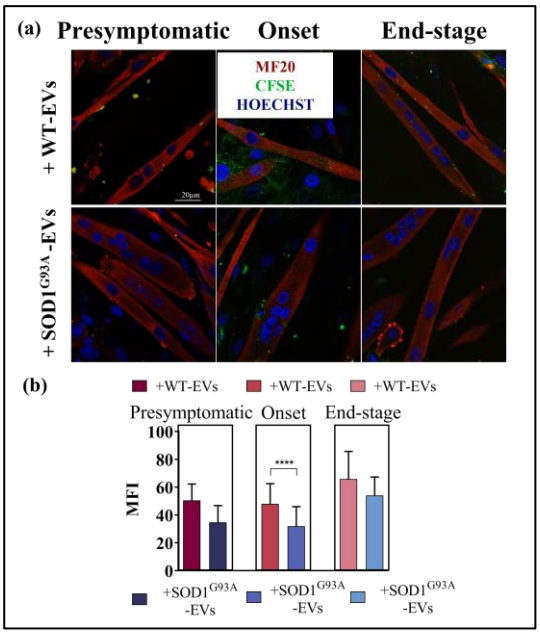

Figure 36. a) Confocal microscopy analysis of C2C12 cells completely differentiated in myotubes treated for 6 hours with CFSE^{+} EVs derived from SOD1^{G93A} mice (+SOD1^{G93A}-EVs) at presymptomatic, onset and end-stage of ALS progression and from age-matched WT littermates (+WT-EVs). Nuclei were stained with Hoechst (blue) and differentiated myotubes with MF20 (red). Scale bar: 20 µm. Magnification 40X. b) Mean Fluorescence Intensity (MFI) quantification of CFSE^{+} C2C12 cells completely differentiated in myotubes after 6 hours of treatment with CFSE^{+} EVs derived from SOD1^{G93A} mice (+SOD1^{G93A}-EVs) at presymptomatic, onset and end-stage of ALS progression and from age-matched WT littermates (+WT-EVs). Values are mean ± SD. $5 \leq n \leq 58$. ****: p-value<0.0001.

4.2.3. Functional effects of SOD1^{G93A} mice-derived extracellular vesicles on C2C12 cell line

Fig. 37 shows the mean and SD of the differentiation index computed for Day 2 of the myogenic differentiation process of C2C12 cells treated with EVs derived from SOD1^{G93A} mice at the presymptomatic, onset and end-stage of ALS progression and from age-matched WT littermates. At the presymptomatic and onset stage of ALS progression, no significant differences were obtained between control and treated C2C12 cells, both with transgenic and control mice-derived EVs (Fig. 37a and 37b). However, a trend toward lower values in the differentiation index was obtained for treated cells, in comparison to control ones. On the contrary, we obtained a significant decrease in the differentiation index, of about 35 %, for C2C12 cells treated with SOD1^{G93A} and WT mice-derived EVs (Fig. 37c), when compared to control cells, at the end-stage of the disease.

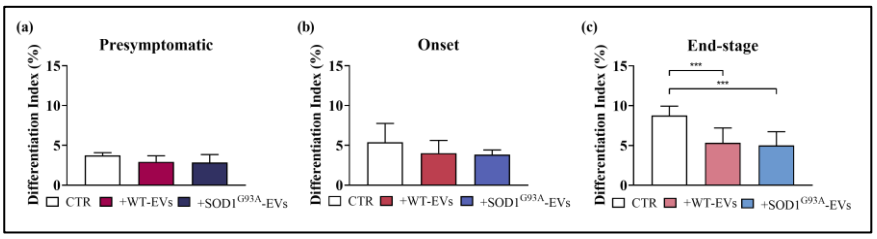

Figure 37. Differentiation index computed at Day 2 of the myogenic differentiation process of C2C12 cells treated with SOD1^{G93A} mice-derived EVs (+SOD1^{G93A}-EVs) and WT mice-derived EVs (+WT-EVs) at the presymptomatic (a), onset (b) and end-stage (c) of ALS progression. "CTR" is for control cells. Values are mean ± SD. 3≤n≤14. ***: p-value<0.001.

The mean values and SD of the fusion index computed for Day 4 of the myogenic differentiation process of C2C12 cells treated with EVs derived from SOD1^{G93A} mice at the presymptomatic, onset and end-stage of ALS progression and from age-matched WT mice are shown in Fig. 38. At the presymptomatic stage, one-way ANOVA revealed a significant decrease in the fusion index for

C2C12 cells treated with transgenic mice-derived EVs, in comparison to cells treated with control mice-derived EVs (Fig. 38a). On the other hand, at the onset and end-stage of ALS progression no significant differences were found in the fusion index between control and treated cells as well as between cells treated with control and transgenic mice-derived EVs, as shown in Fig. 38b and 38c. However, the fusion index of treated cells was lower, even if not statistically significant, when compared to the one of control cells, both for the onset and the end-stage of ALS.

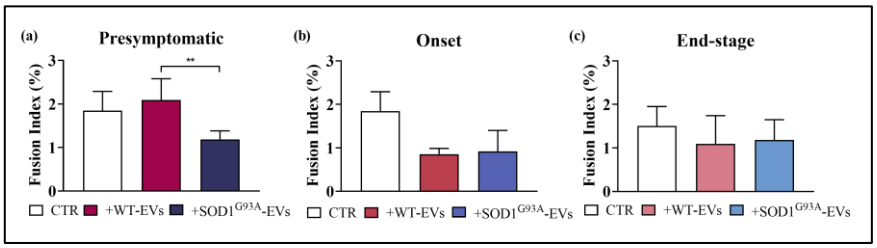

Figure 38. Fusion index computed for Day 4 of the myogenic differentiation process of C2C12 cells treated with $SOD1^{G93A}$ mice-derived EVs (+$SOD1^{G93A}$-EVs) and WT mice-derived EVs (+WT-EVs) at the presymptomatic (a), onset (b) and end-stage (c) of ALS progression. CTR is for control cells. Values are mean ± SD. $2 \leq n \leq 11$. **: p-value<0.005.

Fig. 39 shows the mean ± SD of the differentiation index for Day 4 of the myogenic differentiation process of C2C12 cells treated with EVs derived from $SOD1^{G93A}$ mice at the presymptomatic, onset and end-stage of ALS progression and from age-matched WT mice. At the presymptomatic stage of ALS progression, treated cells with transgenic and control mice-derived EVs reported a decrease, not statistically significant, in the differentiation index, when compared to control cells, as shown in Fig. 39a. Moreover, the differentiation index of cells treated with $SOD1^{G93A}$ mice-derived EVs was lower than that of WT mice-derived EVs, displaying a decrease of about 34 %. Similarly, at the onset stage, one-way ANOVA revealed no significant differences in the differentiation index between control and treated cells, both for transgenic and control mice-derived EVs. However, a decrease in the differentiation index was reported in

treated cells when compared to the control condition as well as between cells treated with SOD1^{G93A} and WT mice-derived extracellular vesicles. On the contrary, one-way ANOVA reported a significant decrease, of about 32 %, in the differentiation index of cells treated with SOD1^{G93A} mice-derived EVs when compared to control cells, at the end-stage of ALS. In parallel, cells treated with EVs derived from transgenic mice displayed a decrease, not statistically significant, in the differentiation index, in comparison to cells treated with control mice-derived EVs.

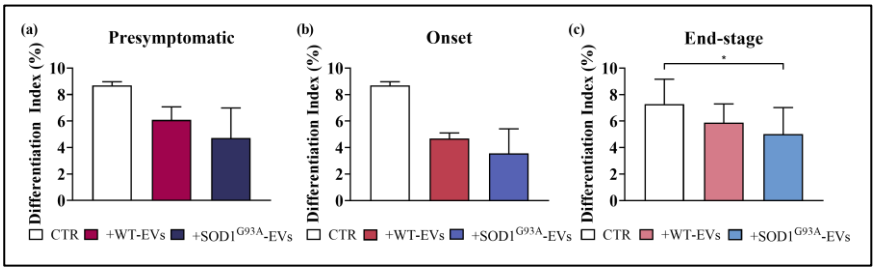

Figure 39. Differentiation index computed for Day 4 of the myogenic differentiation process of C2C12 cells treated with SOD1^{G93A} mice-derived EVs (+SOD1^{G93A}-EVs) and WT mice-derived EVs (+WT-EVs) at the presymptomatic (a), onset (b) and end-stage (c) of ALS progression. CTR is for control cells. Values are mean ± SD. $2 \leq n \leq 11$. *: p-value<0.05.

5. Discussion

The general aim of my PhD project was to develop novel measurement techniques, experimental devices and testing protocols for a more precise assessment of the altered communication between muscle and nerve in Amyotrophic Lateral Sclerosis progression.

An innovative experimental technique, together with a continuous testing protocol, for the *in-situ* measurement of muscle and NMJ functionality in isometric and isotonic conditions, with particular reference to isotonic fatigue, were developed. As regarding the development of isotonic fatigue protocol [105], the results pointed out that the reference value of the optimal force proposed in literature as resistive load to be imposed during isotonic fatigue phase underestimated the real optimal force. At this point, it has to be noted that even if the real-time measurement of muscle maximum power, and therefore of the experimental optimal force, resulted in an increase in the test duration and in the control software complexity, it was necessary to highly enhance the measurement accuracy of all the parameters related to isotonic fatigue. When testing the muscles only through direct stimulation, for example, the coefficient of variation for the fatigue time decreased from 61.4% to 18.4% when experimental optimal force was employed. In particular, the reduction in the variance, and therefore in the CV, of all the isotonic fatigue parameters, when muscle was tested at the experimental optimal force rather than at the reference value, was due to the fact that at the experimental optimal force the muscle developed its real maximum power, and not a power that could be quite close but also very different from this maximum value. On this basis, a novel experimental technique and testing protocol for the measurement of NMJ functionality in isometric and isotonic conditions were developed based on the contractile response evoked by direct stimulation on muscle membrane and indirect one through the nerve [106]. Results strongly confirmed the measurement accuracy in terms of average value and coefficient of variation of all

the isometric and isotonic parameters measured through the nerve stimulation in comparison with the corresponding values obtained for muscle membrane stimulation. This testing protocol was then applied on Tibialis Anterior-sciatic nerve preparations of $SOD1^{G93A}$ mice at the presymptomatic, onset and end-stage of ALS. $SOD1^{G93A}$ mice TA muscles were characterized by a progressive slowdown of contractile kinetics during pathology progression, highlighting a significant defect in their contractile response, when stimulated on the membrane and through the sciatic nerve. No differences were found in the tetanic force generated by TA muscles of transgenic mice when stimulated directly and indirectly, even if it is known a dismantling of NMJ during ALS disease [8]. However, since the contractile response of the muscle was measured both for direct and indirect stimulations, it is possible that the damage at muscular levels might strongly hide the impairment of NMJ functionality. Isotonic fatigue test results pointed out a different response of transgenic and control muscles. $SOD1^{G93A}$ mice developed power and work in a different way than control muscle and, as a consequence, fatigue time in transgenic muscles was higher than control ones, probably correlated to energy management by mitochondria [116]. The *Isotonic Neurotransmission Failure*, a parameter here proposed to capture NMJ impairment in isotonic conditions, computed at 80% of isotonic fatigue test resulted significantly higher in $SOD1^{G93A}$ mice at the end-stage in comparison to age-matched WT samples, pointing out that, even if the transgenic muscles showed a greater resistance to fatigue, they underwent a bigger impairment in the synaptic transmission. These results also confirmed the complexity of the mechanism behind the resistance to fatigue, as progressive failure of NMJ functionality and the consequent energy management by mitochondria in ALS. Finally, it worth nothing that the technique and testing protocol here proposed may be applied to other mouse models, contributing to unravel new mechanism behind several other neurogenerative diseases.

With the aim of measuring engineered skeletal muscle contractility, as the X-MET [50], an innovative sensor based on the detection of the displacement of an elastic pin, caused by the 3D engineered skeletal tissue's contraction, through an optical tracking method [108] was developed. The sensor was designed to be easily integrated with an optical setup, thus also performing continuous measurement for long period, and with a system for tissue electrical stimulation. The sensor was characterized testing control X-METs, and the experimental results confirmed that it was able to accurately measure the tissue contraction without affect tissue's growth and maturation. In parallel, the sensor was used to measure, as *proof-of-concept* of its capability to detect contractile alterations, the force response in a particular physio-pathological condition, the "accelerated aging". The results clearly showed that the sensor was also able to discriminate alterations in the force developed by the tissues treated to simulate an aged microenvironment.

With the aim of developing a 3D model of neuromuscular junction, we designed and realized a device to couple the X-MET and embryonic spinal cord primary culture. Based on the results obtained studying the bi-dimensional (2D) communication between the 2D population of the X-MET and spinal-cord derived cells, a microfluidic device was designed *ad hoc* to enhance the fusion and formation of NMJ. The device allowed the two populations to grow in two different chambers, being connected only by the axons formed in the microchannels, to have a spatio-temporal control over the cells and cells' migration. Electrical stimulation on neuronal cells in the 3D microfluidic device was able to promote the elongation of neurofilaments' along all the length of the microchannels, even if it was not possible to observe the X-MET in the microscopy, due to the conformation of the device. To this, a new configuration of the device might be useful to allow, as much as possible, the *in-vitro* connection between the two compartments.

It is known that extracellular vesicles are involved in ALS pathological proteins transportation, as toxic mediators. However, EVs have been widely investigated when derived from cell lines and

primary cell cultures [98], [99], only few studies investigated their involvement in ALS development and progression, whether in animal models or patients [100], [101]. In view of this, a molecular characterization of EVs derived from serum of $SOD1^{G93A}$ ALS mouse models at the three different disease stages, i.e. the presymptomatic, onset and end-stage of ALS, was performed to study the physio-pathological role of EVs in the modulation of cell functions, with the future aim of evaluating the effects of EVs on the different models here proposed. The increasing number of circulating EVs in $SOD1^{G93A}$ mice during ALS progression suggested that they might represent a direct effect of the disease, rather than play a role in its pathogenesis. With the aim of mimicking as much as possible the *in-vivo* condition of circulating EVs in $SOD1^{G93A}$ mouse plasma, we treated skeletal muscle C2C12 cell line with a fixed volume of EVs, thus maintaining the different number of EVs. As regards proliferating myoblasts, at the onset of the pathology, $SOD1^{G93A}$ mice-derived EVs had a higher capability of fusion on myoblasts, in comparison to WT-mice derived EVs, while at the end-stage their capability significantly decreased. Even if the number of EVs increased during ALS progression, their capability of fusion on myoblasts seemed not to be correlated with the disease spreading. These results suggested that the fusion of EVs on skeletal muscle cells was not random but seemed to be mediated by specific membrane receptors of the target cells. In addition, since ALS is a multisystemic disease, it is possible to note that the target of $SOD1^{G93A}$ mice-derived EVs might be neuronal-specific, as reported in literature [84], [102]. To this, further experiments are required to evaluate the uptake of $SOD1^{G93A}$ mice derived-EVs by neuronal cells. At all stages of ALS progression, $SOD1^{G93A}$ mice-derived EVs had a lower capability to fuse into myotubes, in comparison to WT ones. At this point, it has to be noted that EVs can fuse to the target cells by endocytosis or by directly fusing with the plasma membrane, thus releasing their cargo [83]. Experimental results suggested that the preferential way of fusion to myotubes could be by endocytosis, even if it could be not excluded that EVs

fuse to myotubes by realising their cargo. However, since myotubes are syncytial aggregates, we might have not been able to observe this type of fusion by immunofluorescence analysis, due to the exposure time. As regarding the functional effects of EVs on C2C12 cells' differentiation process, at Day 2, control and transgenic mice-derived EVs had a similar effect on C2C12 cells' differentiation, in terms of differentiation index values. However, only when treating the cells with EVs obtained from $SOD1^{G93A}$ mice at the end-stage and age-matched WT mice, a significant decrease in the differentiation index was reported, when compared to untreated cells. These results suggested that the EVs affected C2C12 cells' differentiation in the early stages of this myogenic process. As a consequence, at the end of the differentiation process, treated cells displayed a reduction in the fusion and differentiation index, in comparison to control cells, being lower the number of myotubes and of nuclei for each myotube. However, in this case EVs derived from $SOD1^{G93A}$ mice had a higher effect in the impairment of cells' differentiation, even if not statistically significant, in comparison to EVs derived from control littermates. This outcome suggested the potential role of EVs derived from $SOD1^{G93A}$ mice in the impairment of C2C12 cells differentiation process during ALS progression. Of note, it is possible to hypothesize that these effects might be due to the transfer of toxic elements to the myogenic differentiation process. To this, a deeper analysis of EVs cargo, and more specifically of differentiation markers, might represent a crucial tool for understanding the physio-pathological role of EVs in cells' differentiation process.

6. Materials and methods

6.1 Animals

All experiments were conducted within the animal welfare regulations and guidelines of the Italian National Law D.L. 04/03/2014, n.26, about the use of animals for research. Both female and male, $SOD1^{G93A}$ mice at the presymptomatic (about 75 days of age), onset (about 90 days of age) and end-stage (about 145 days of age) of ALS progression and age-matched Wild Type C57/BL6 ones were employed in this project.

6.2 Development of techniques, devices and testing protocols for the measurement of muscle and neuromuscular junction functionality

With the aim of measuring muscle and neuromuscular junction functionality, a series of novel testing tools were developed for a more precise assessment of the altered communication between muscle and nerve in ALS progression. In detail, a novel technique for the *in-situ* measurement of murine TA NMJ functionality in isotonic conditions was proposed together with an innovative parameter, INF. Moreover, an embedded sensor for the measurement of engineered skeletal muscle tissue contractile force with a non-invasive technique was designed and realized. Finally, a 3D microfluidic device was developed to promote the formation of NMJ between spinal-cord derived cells and 3D engineered skeletal muscle.

6.2.1. *In-situ* methodology and experimental protocol for neuromuscular junction functionality measurement

With the aim of studying the neuromuscular junction functionality of $SOD1^{G93A}$ mice at the pre-symptomatic, onset and end-stage of the disease in isometric and isotonic conditions, a series

of preliminary studies, by employing the *in-situ* technique, was conducted to evaluate the reduction in the errors of the parameters characterizing isotonic contraction by testing the Tibialis Anterior muscle to shorten against a load equal to the experimental value (F_{exp}) [105], i.e. the force at which the muscle developed the maximum power, rather than the reference optimal force (F_{ref}) always considered equal to 1/3 of the maximum generated force, as suggested by the literature to date [35]. A proper placing of the electrodes and an extensive testing protocol, by also proposing a novel parameter, *Isotonic Neurotransmission Failure*, to properly capture the impairments in neurotransmission during isotonic fatigue were devised too [106].

For all these purposes, the experimental procedure was based on the *in-situ* methodology. In detail, before the beginning of the experiment, the mouse to be tested was anesthetized with an intraperitoneal injection of Ketamina Cloridrato (Ketalar) and, during the experiment, a supplemental dose was given if necessary. The skin of the left hind limb muscle was removed, and the TA was identified. Its tendon was cut a few millimetres far from the end of the muscle, taking care not to include the tendon of Extensor Digitorum Longus muscle in the surgical isolation. The surrounding muscles were removed to expose the sciatic nerve. The mouse was placed on a temperature-controlled plate (37 ± 1 °C), the hind limb was inserted in a clamp to immobilize it as much as possible, and the foot was scotch-taped to the platform. During the test, the exposed tissues were kept moist by periodic application of mineral oil [29]. The experimental set-up is shown in Fig. 40. The TA tendon was tied with a 0.16 mm diameter nylon wire slip knot as close to the muscle attachment as possible and connected to the level-arm of a dual-mode actuator/transducer system (305C-LR, Aurora Scientific), as shown in Fig. 40b. In particular, the level-arm could be controlled either in force or in position mode, allowing to continuously switch between isometric and isotonic stimulation.

Muscle contractility was evoked by two pairs of stranded stainless wire electrodes (AS632 Cooner Wire): for indirect

stimulation the electrodes were placed close to the sciatic nerve, while for the direct one they were inserted laterally just under TA muscle surface, as shown in Fig. 40b. Electrical square pulses of about 7 mA for nerve stimulation and 5 mA for muscle one were generated by two electrical pulse stimulators (701C Aurora Scientific) with a width of 1 ms [29].

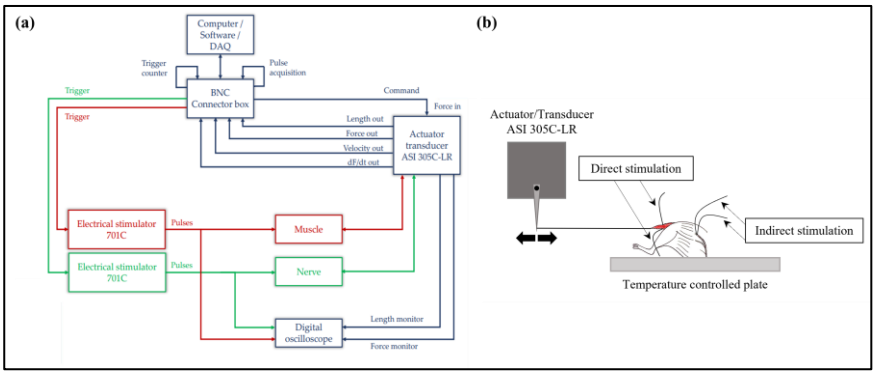

Figure 40. Schematic of the (a) experimental set-up and of the (b) electrodes positioning for direct and indirect stimulations. Tibialis Anterior muscle is in red, sciatic nerve is grey [106].

The actuator/transducer and the pulse stimulators were controlled by a custom-made software developed in LabVIEW 2019 (National Instruments) using a data acquisition board (PCIe-6363X, National Instruments). This software allowed for choosing all the stimulation parameters while simultaneously acquiring muscle shortening, force, time derivative of force, shortening velocity and pulse sequence for post-processing. Data were acquired with an acquisition frequency of 20 kHz for single pulse stimulation and 1 kHz for all pulse train stimulations. Indeed, during single pulse stimulations different parameters related to the "time" were computed, as TTP (Time to Peak) and 1/2RT (Half Relaxation Time), and a higher frequency was needed to increase measurement accuracy of this variable. For the remaining parts of the protocol, the parameters of interest were only related to the force and displacement amplitude, and a high accuracy on the measurement of

time was not necessary. A digital oscilloscope (Tektronix DPO2014B) was included in the experimental set-up for the real-time visualization of force and length. The optimal initial length was obtained by subjecting the muscle to a series of single pulses to find out the maximum twitch force [31]. At the end of the experiment, the mouse was sacrificed by cervical dislocation to minimize suffering. TA muscle length (L_o) and mass were measured for data normalization through an analog caliper, with an accuracy of 0.05 mm, and a Pioneer precision scale (Ohaus, Parsippany, NJ), with an accuracy of 0.1 mg. Muscle cross- sectional area (CSA) was estimated as reported:

$$CSA = \frac{m}{L_f * d} \qquad (3)$$

where m is the muscle mass, L_f is the optimal fiber length and d is the density of mammalian skeletal muscle, which is 1.06 mg/mm^3 [117]. In particular, L_f is obtained as the product between L_o and the fiber length to the tibialis length ration, which is equal to 0.6, as reported in literature [117].

To evaluate the errors introduced by testing TA muscle at the reference optimal force (F_{ref}) rather than at the experimental value (F_{exp}), fifteen 3-month-old WT mice were used, and two groups of muscles were subjected to the same experimental protocol, except for the isotonic fatigue phase. The numerosity of the two groups was chosen according to the sample size equation, which considers the z-score, the confidence interval and the margin of error. In particular, group 1 was constituted by 8 muscles stimulated to shorten against the experimental optimal force, while group 2, made up of 7 muscles, lifted the reference optimal force. Initially, single pulses were delivered to the muscle to measure the contractile kinetics parameters (Twitch force, rate of force production and of force relaxation, Time to peak, Half relaxation time). To obtain the tetanic force, the muscle was subjected to several pulse trains at different frequencies. Then, the third phase of the protocol consisted in the application of the after-load technique for the real-time

measurement of muscle maximum power and, therefore, of experimental optimal force (the force at which the muscle developed the maximum power). Finally, the TA muscle was subjected to the isotonic fatigue protocol, as previously described. The fatigue time, measured as the time necessary to reach the 10 % of the maximum shortening value, the power and work generated by the muscle during the fatigue test, computed as the sum of the product of the constant load both for the highest shortening velocity and for the displacement during each shortening, were measured [105].

Neuromuscular junction functionality of $SOD1^{G93A}$ mice was then evaluated through the *in-situ* methodology by comparing muscle contractile response elicited by direct stimulation on TA muscle membrane and indirect one through the sciatic nerve. Ten 5-month-old WT mice were employed to assess the precise sequences and resting times of the testing protocol for the measurement of isometric and isotonic parameters of muscle and NMJ functionality. To deeply characterize the NMJ in isometric and isotonic conditions, with a particular reference to isotonic fatigue, a continuous extensive testing protocol was developed to measure the synaptic transmission alterations between TA muscle and sciatic nerve [106]. Subsequently, to validate the proposing technique, eight 5-month-old WT mice were used to compute all the parameters proposed in the experimental protocol and five 5-month-old $SOD1^{G93A}$ mice were then used to compute the *Isotonic Neurotransmission Failure*. Finally, $SOD1^{G93A}$ mice at the pre-symptomatic, onset and end-stage of the disease and age-matched WT ones, with a number of samples ranging from 9 to 16, were used to evaluate the impairment in the neurotransmission in isometric and isotonic conditions during the disease progression, with a particular reference to isotonic fatigue.

As regards the real-time measurement of muscle maximum power, muscle tetanic force (F_{tet}) was determined from the force-frequency curve, for direct and indirect stimulations, and it was then employed to obtain the values of resistive loads to be imposed during the after-load test in isotonic conditions. The Hill's curve

[35], representing the relationship between muscle force (F) and shortening velocity (v), was computed interpolating the experimental data by using the 'Nonlinear Curve Fit' VI (LabView 2019, NI), on the hyperbolic equation:

$$(F + a) * (v + b) = c \qquad (4)$$

where a, b, c are positive constant values. In addition to the interpolation on the 5 experimental points, the curve was forced to pass through the point ($v = 0$; $F = F_{tet}$). Then the program estimated the power delivered by the muscle and, therefore, the experimental optimal force, both for direct and indirect stimulations. In addition, the Neurotransmission Failure was computed as:

$$NF = \frac{F-MF}{1-MF} \qquad (5)$$

where the force reductions in indirect (F) and direct (MF) stimulations were computed as the difference between maximum forces developed by the muscle at the first stimulation and at the others, normalized on the tetanic force generated at the first stimulation. The Intratrain Fatigue was computed as the ratio between the force generated by the muscle at the end of the pulse train and the maximum force generated during the same pulse train, in percent. As for the indirect stimulation, the NF and the IF values were computed on the first pulse train immediately after the direct stimulation.

6.2.2. Embedded sensor design for engineered tissue contractility force measurement

A sensor for the measurement of *ex-vivo* engineered tissue contractile force during its growth was designed and realized, by using an optical tracking method [108]. The case concept of the sensor was based on the measurement of the deflection of a flexible pin, designed with specific dimensions and compliance.

Once the sensor was realized, the elastic pin was calibrated to compute the experimental elastic constant *k.* One end of the elastic pin was fixed to a linear actuator with a resolution of 0.10 μm (Zaber, NA11B16-T4) and the other end, at the desired length (22.7 mm), was connected to a micro-force transducer with a resolution of 1 μN (Kronex, AE801). The elastic pin was subjected to six different known displacements by the linear actuator, namely 5 μm, 10 μm, 20 μm, 30 μm, 40 μm and 50 μm. This range of displacements was chosen as that expected from the force range reported for a theoretical elastic constant of 20 N/m [50], [52]. The duration of the displacement signals was set at 2 s, and each test was repeated 10 times. A custom-made software developed in LabVIEW 2019 allowed the synchronization between the linear actuator displacement and the force signal acquisition.

As regarding the experimental set-up, the X-MET was used as 3D muscle engineered tissue, which was obtained according to a protocol similar to the one illustrated by Carosio et al. [50]. Briefly, a heterogeneous cell population was obtained by the isolation of skeletal muscle from the hind limbs of a wild-type mice (WT) with a process of mechanical and enzymatic digestion (gentleMACS Octo Dissociator, MiltenyiBiotec). After 5-6 days in culture, the cells were induced to differentiate using a differentiation medium and after 2-3 days the cellular monolayer was delaminated by moving a tip around the peripheral area of the dish. To allow the complete remodelling of the X-MET in a self-organized cylindrical structure, the delaminated monolayer was clamped in a silicone-coated dish and maintained for three days. After this period, the specimens were clamped in the proposed sensor.

Differentiation medium (DM), constituted of Dulbecco's Modified Eagle Medium (DMEM), 5 % horse serum, 25 mM HEPES, 4 mM L-glutamine, 0.1 % gentamicin, penicillin/streptomycin, was used for the growth and the maintenance of the X-MET in culture. After demonstrating that the developed embedded sensor did not affect the correct growth of the X-MET, we tested the ability of the sensor to capture alterations in force contractility of muscle engineered tissues treated with Bovine Serum Albumin (BSA), known to mimic an aged microenvironment

[118], [119]. In view of this, four different X-METs were cultured in DMEM only enriched of 1 % BSA from the day they were placed in the novel sensor. The contractile properties of the specimens were measured for five consecutive days. This duration was chosen for two main reasons. At first, the 'accelerated aging' induced with the treatment was preliminary demonstrated yield to unresponsive X-METs after three days in culture. Second, we wanted to demonstrate the capability of our sensor to measure the contractility of the control X-METs and to verify the correct growth and maturation of the tissues over a longer period. Moreover, the embedded sensor was designed to be easily integrated with other technical facilities, as a stereomicroscope and a set-up for tissue electrical stimulation. X-MET contractility was evoked by a pair of platinum electrodes, placed parallel to the tissue, and connected to a pulse stimulator (Aurora Scientific 701C) (Fig. 41). The entire sensor was placed under a stereomicroscope (NIKON SMZ 800) equipped with a high frequency camera (Basler aca2040-180km) for image acquisition and an illuminator (Photonic PL-3000) was employed to adjust the image contrast for the post-processing correlation of the images. For the entire duration of the test, the tissue was maintained at a temperature of 37 °C ± 0.3 °C by using a temperature control plate (Okolabs.r.l., H401).

The stimulation protocol was constituted by one twitch test and four unfused/fused tetanic stimulations, in isometric conditions, to measure tissue contractile kinetics and force frequency relationship, respectively. All the stimulation parameters were chosen according to those used in our previous works [50]–[52] and similar to those found in the literature [120]. The current intensity of a single pulse was set to 400 mA for both twitch test and tetanic stimulations. The twitch response was obtained with a 1 ms single pulse stimulation.

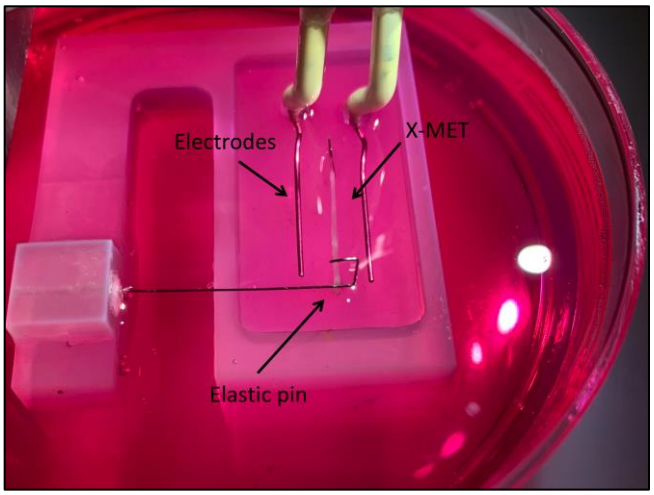

Figure 41. Picture of the sensor with the two platinum electrodes placed parallel to the X-MET [108].

These parameters were shown to elicit the maximum twitch force (F_{TW}) of the X-MET [50] in a standard supramaximal way (i.e. +50 % of the maximum current value eliciting maximum twitch force). The four tetanic stimulations were delivered in a random order, namely at 60 Hz, 20 Hz, 40 Hz and 80 Hz, to avoid tissue adaptation to increasing or decreasing frequencies, with 1 ms pulse trains of a duration of 0.8 s. A resting time of 60 s was allowed before the first train stimulation, and 120 s of rest before the following ones. These values were chosen accordingly to a series of preliminary experiments aimed at evaluating the minimum resting time necessary to avoid tissue fatigue [29], [33], [121]. Time to peak (TTP) and half relaxation time (1/2RT) were measured from the twitch response to characterize the contractile kinetics of the tested X-METs. The active force generated during the twitch test and the tetanic stimulation was measured and divided by the tissue average cross-sectional area (CSA) to compute the specific force. To this, before each test, an image of the entire tissue was acquired to calculate the cross-sectional area, for all the acquisition days. Each image was then processed with an *ad hoc* program developed in Matlab 2021, based on the evaluation of the grey levels and,

therefore, of the average diameter of the X-MET. The force-frequency curve was then obtained for control and treated X-METs.

The displacement of the elastic pin, caused by the X-MET contraction, was measured by an optical tracking method. The algorithm was developed in LabVIEW 2019 using 'IMAQ Optical Flow' VI, which is based on the computation of the change in location of a set of points between two consecutive images [Ref 38,45]. For all the experimental tests, a region of interest (ROI) of 40x15 pixels was selected on the pin in correspondence with the engineered muscle tissue with the longer side parallel to the pin axis and divided in 15 nodes [112]. However, it is important to consider that the irregular surface pattern of the X-MET could cause an inhomogeneous speckle on the same, as well as the illuminator can induce an inhomogeneous image contrast. For these reasons, it was not always possible to select a ROI in the centre of the axis between the elastic pin and the X-MET. Therefore, the errors introduced in the correlation algorithm by varying the positioning of the ROI from the central one were evaluated [112]. To do this, the elastic pin was subjected to known displacement by using a linear actuator (Zaber NA11B16-T4) with a resolution of 0.01 µm provided by a stepper motor controller (Zaber X-MCB2) (Fig. 42a). One end of the elastic pin was fixed and the other one was pushed by the linear actuator at a length of L= 22.7 mm. The pin was subjected to sinusoidal displacements of two different peak-to-peak amplitudes equal to 5 µm and 10 µm and with a frequency of 10 Hz. These parameters were chosen as better representative of the contractile kinetics of the muscle engineered tissue analyzed in preliminary experiments. The duration of the displacement signals was set at 3 s and the images were acquired by a high frequency camera (Basler acA2040-180km) mounted on a stereomicroscope (NIKON SMZ 800).

The images were acquired at 300 fps, with an optical magnification of 2X and with a resolution of 1020x300 pixels. This combination of acquisition parameters resulted to be the optimal working condition of the tracking algorithm, in terms of accuracy in capturing the actual movement of the pin [109].

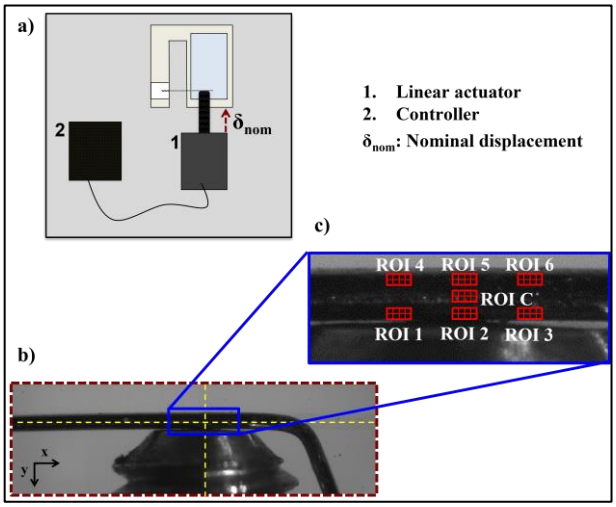

Figure 42. a) Experimental setup for ROI positioning evaluation. b) Image of the linear actuator and the elastic pin. Magnification of 2X, 1020x300 pixels. c) ROI positionings around the central one [112].

A custom-made software developed in LabView2019 allowed to set all the displacement parameters, such as the waveform, peak-to-peak amplitude, frequency and duration of the linear actuator movement, and also to synchronize the displacement with the image acquisition. The acquired images were then processed with the optical tracking algorithm to compute the displacement of the pin in different regions of interest (ROIs) to evaluate the effects of the ROI positioning compared to the central one (Fig. 42b, 42c). For all tests, we selected a ROI of 40x15 pixels divided into a fixed and regular grid of square elements and we analysed 15 nodes. Fig. 42c shows all the analysed ROIs: the central ROI was selected on the pin in correspondence with the motor axis, while the other ROIs were moved from the central ROI of the following (x, y) pixel coordinates: (-50, 8), (0, 8) and (50, 8) respectively for ROI 1, ROI 2 and ROI 3 and (-50, -8), (0, -8) and (50, -8) respectively for ROI 4, ROI 5 and ROI 6.

The error due to a wrong ROI positioning on the force measurements was evaluated for the six selected ROIs around the central one, for two displacement amplitudes, and for each of these

combinations 5 repetitions were performed. At first, we computed the relative percentage error introduced using the central ROI (ROI C), calculated as follow:

$$\varepsilon_{rel_{ROI\,C}} = \frac{\delta_{meas_{ROI\,C}} - \delta_{nom}}{\delta_{nom}} * 100 \qquad (6)$$

where $\delta_{meas_{ROI\,C}}$ is the displacement measured by the tracking algorithm for the ROI C and δ_{nom} is the nominal displacement imposed by the linear actuator. This is the systematic error of the tracking algorithm and will be then compensated during measurements. Subsequently, the relative percentage error computed for the other six ROIs with respect to ROI C was calculated as follow:

$$\varepsilon_{rel_{ROI\,X}} = \frac{\delta_{meas_{ROI\,X}} - \delta_{meas_{ROI\,C}}}{\delta_{meas_{ROI\,C}}} * 100 \qquad (7)$$

where $\delta_{meas_{ROI\,X}}$ is the displacement measured by the tracking algorithm for the six ROI analysed. These displacements were calculated as the average of the peak-to-peak amplitude for the 20 acquired periods.

It is important to note that all the displacement values obtained from the experimental tests were therefore corrected to compensate these errors.

The displacements obtained from the tracking algorithm were then converted in force values by multiplying them for the experimental elastic constant, and finally divided by the CSA to obtain the specific forces:

$$F_{specific} = \frac{\delta_{meas} * k}{CSA} \qquad (8)$$

where δ_{meas} is the displacement, along the y direction, measured by the tracking algorithm and k is the experimental elastic constant obtained through the elastic pin calibration.

6.2.3. Development of neuromuscular junction microfluidic device and electrical stimulation protocol

With the aim of promoting the formation of NMJ between the 3D engineered muscle models, as the X-MET, and neuronal cells, we designed and realized an innovative 3D microfluidic device. To accomplish this aim, we initially characterized the interaction between mouse spinal cord primary culture and the bidimensional population of the X-MET, namely primary culture obtained using muscle tissue harvested from mouse hind limbs, through a commercial 2D microfluidic device (Microfluidic Neuron Device, Xona Reasercher Protocol) for the formation of NMJ. Subsequently, we developed an innovative device to enhance the fusion and the formation of NMJ between mouse spinal cord primary culture and the X-MET.

To characterize the interaction between mouse embryonic spinal cord primary culture and the 2D population of X-MET as well as to investigate the potential role of the X-MET to be used for the generation of the 3D NMJ model, a RT-PCR was first performed for acetylcholine receptors (AChRs) β1 and β2 comparing 2D and 3D X-MET after 7 and 15 days in Differentiation Medium (DM). In addition, we conducted preliminary co-cultures between the X-MET and the mouse embryonic spinal cord primary cultures, by explanting the spinal cord from a WT mouse. Finally, we performed immunofluorescence analysis on cross-section of X-MET-Spinal cord explant for Smi-32 and Myosin Heavy Chain (MyHC) after 10 days of co-culture. Hoechst was used for nuclear staining. To fully confirm the role of the X-MET for the generation of a 3D NMJ model, we evaluated the presence of mature subunits of AChRs, namely AChR- ε and AChR- ɤ, by performing a RT-PCR in X-MET and X-MET co-cultured with E15.5 ventral spinal cord-derived from WT mice [122]. We chose to use the ventral portion of the spinal cord since it contains motor neurons responsible of skeletal muscle innervation.

The commercial microfluidic device (Neuronal Microfluidic Device, Xona Researcher Protocol) for NMJ formation consisted of two chambers connected by a microgroove barrier of 3 μm in height, which acted as a 'filter', allowing the passage of neuritic processes into the axonal side but not of cell bodies. Once obtained the 2D X-MET, the extraction of spinal cord from UBC/GFP mice was computed, and the Neural Tissue dissociation kit (Miltenyi Biotech) was used to obtain the motor neurons culture. Neural tissue from embryo spinal cord (animal age ≤ P7) were dissociated into single-cell suspension by combining mechanical dissociation with enzymatic degradation of the extracellular matrix. After the digestion phase, the samples will be resuspended in Neurobasal Medium supplemented by 2 % of Fetal Bovine Serum (FBS), 1 % Horse Serum (HS), 1 % of penicillin/streptomycin, 1 % of l-glutamine and 2 % B-27 supplement. Cells were placed on the axonal side of the microfluidic device, coated with Poly-L-Lysine.

On the basis of the results obtained with the 2D co-cultures, the 3D microfluidic device was developed to enhance the fusion and the formation of NMJ between X-MET and embryonic spinal cord-derived cells. First, the spinal cord-derived cells were plated in the nerve compartment of the device and, approximately after 7 days, the X-MET was pinned inside the device.

In parallel, to promote the formation of NMJ in 3D microfluidic device, a preliminary simulation study was conducted to analyse the electric field distribution in the 3D device for the design of different electrode systems [115]. The device was modelled in CST Studio Suite 2019, a software which is a general-purpose electromagnetic simulator based on the Finite Integration Technique (FIT) [123], that provides a spatial discretization to various electromagnetic problems, starting from the Maxwell's equations. For the simulation tests, the dielectric constant values reported in the literature for the different materials composing the device were considered. In particular, the entire device structure was simulated with the dielectric constant of the silicon, equal to ε_s=11.9 F/m. The neuronal chambers, the lateral and central grooves and the microgroove

barrier were modelled with the dielectric constant of the Neurobasal Medium used for neuronal cells culture, equal to ε_n=80 F/m [124]. On the other hand, the muscle engineered tissue chamber was modelled with the dielectric constant of Dulbecco's Modified Eagle Medium (DMEM) with fetal bovine serum, used for muscle tissue culture, corresponding to ε_m=77.59 F/m [125].

The electric field simulations were generated by the potential applied on the surface of two electrodes, placed symmetrically in the two neuronal chambers. To find out the optimal electrode configuration that could properly stimulate the neurites in the microchannels without affecting neuronal cells in the culture chambers, different simulation tests were performed by varying the electrode type, the position in the neuronal chambers, the size and the applied voltage intensity. All the tested electrodes were built as perfect electric conductors (PEC), as required by the software. Of note, the electrodes for muscle and/or nerve stimulation are usually realized in platinum, which could be considered a perfect electric conductor [126].

Initially, pin electrodes of cylindrical shape were tested, by varying four specific positions, namely high-centre, low-centre, internal and external in the neuronal chambers, as shown in Fig. 43a, and two different values of the radius (0.2 mm and 0.3 mm). Moreover, three voltage intensities (2 V, 4 V and 8 V) were tested according to preliminary results showing that potential values of 16 V and 32 V induced an electric field on the bottom of the neuronal chambers of 6.36 kV/m and 12.71 kV/m, respectively, thus resulting critical for cells survival. Subsequently, the electric field generated by two electrodes with a ring shape (O-ring) [127] was simulated, testing three voltage intensities and two positions in the neuronal chambers. In detail, they were placed on the top (h=5 mm) and at half height (h=2.5 mm) of the neuronal chambers, as shown in Fig. 43b. Two dimensions of the electrodes were varied: the first one was characterized by an external radius of 2.1 mm and internal radius of 1.7 mm, while the second one by a radius of 1.5 mm and 1.1 mm, respectively, for the external and the internal dimension.

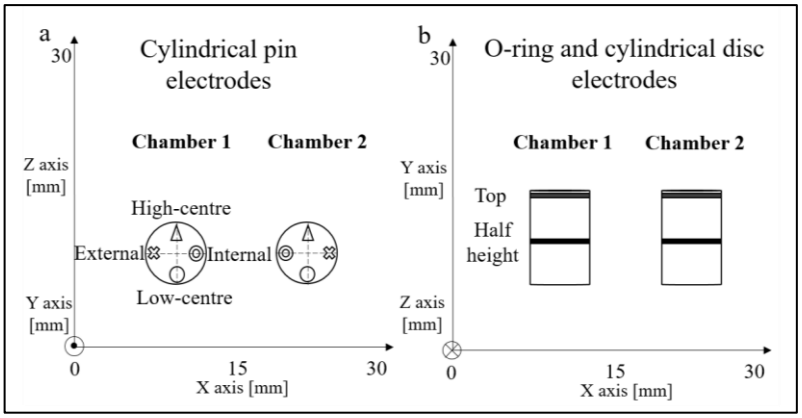

Figure 43. Schematic of the electrodes' positioning in the neuronal chambers. a) Device (top view) for cylindrical pin electrodes' positioning. b) Device (lateral view) for O-ring and cylindrical disc electrodes' positioning [115].

Finally, a couple of cylindrical disc electrodes 1 mm high was tested for their electric field distribution, by varying the position in the neuronal chambers (top and half height), the geometry (2.1 mm and 1 mm of radius) and the voltage intensities (Fig. 43b).

As described before, mouse embryonic spinal cord-derived cells were plated in Petri dish of 35 mm of diameter and stimulated with pin electrodes of 0.3 mm of radius, by applying 1 ms square wave pulses of 5 V at a frequency of 1 Hz, starting from the 7^{th} day of culture. Two different durations of the electrical stimulation (ES) were investigated, 1 hour and 2 hours, by fixing the cells with 4% paraformaldehyde (PFA) after 24 and 48 hours the end of the ES protocol. At the end of the experiment, 5 Fields Of View (FOV) were acquired for each Petri dishes and analysed the images with ImageJ software to compute the number of nuclei and the axons' elongation.

As regarding the electrical stimulation of neuronal cells plated in the 3D microfluidic device, embryonic spinal cord cells obtained from GFP^+ C57/BL6 mouse were first seeded at a density of 50000 cells/chamber in the 3D microfluidic device, and, after two days, X-MET, generated from WT mouse, was pinned in the rectangular

chamber of the device. Spinal cord-derived cells were stimulated 24 hours later with pin electrodes of 0.3 mm of radius, by applying 1 ms square wave pulses of 5 V at a frequency of 1 Hz, for 30 minutes. With the aim of promoting, as much as possible, the elongation of neurofilaments' along the microchannels, cells were stimulated 96 hours later, by applying the same electrical stimulation protocol. After two weeks, neuronal chambers were gently washed 2 times with PBS, fixed with 4 % paraformaldehyde (PFA) for 10 min for consequent fluorescent microscopy analysis.

6.3 Molecular characterization and functional effects of SOD1^{G93A} mouse extracellular vesicles on C2C12 cell line

6.3.1. Extracellular vesicles isolation from mouse serum

Extracellular vesicles were isolated from SOD1^{G93A} and WT mice blood serum, with a number of samples ranging from 3 to 6 for all tested stages of ALS, as described in literature with minor modification [128], [129]. Briefly, mouse was anesthetized with Ketamina Cloridrato (Ketalar), and then blood was collected from the sternum and placed at room temperature (RT) for about 1 h to allow complete coagulation. The blood was then centrifugated at 10000 rpm for 2 min at RT to collect the serum [130]. EVs were isolated from mouse serum by using ExoQuick KIT (SBI, System Biosciences, Palo Alto, CA), according to the manufacturer's instructions. Finally, EVs were suspended in 100 µl of PBS and stored at +4 °C.

6.3.2. Staining

According to the manufacturer's instructions, mouse blood EVs were stained with 1 mM Carboxyfluorescein succinimidyl ester (CFSE) (Life Technologies-ThermoFisher, CA) membrane-

permeable dye, whose succinimidyl group binds to intracellular lysine residues and other free primary amines, producing green fluorescence.

6.3.3. Flowcytometric analysis

To visualize EVs derived from SOD1^{G93A} mice at the presymptomatic, onset and end-stage of the disease and from age-matched WT mice, a flowcytometric analysis was performed (Fig. 44). In detail, we used nanobeads (Sperotech) with known size of 0.5, 0.7 and 1.3 µm to create a gate, with a size lower than 1 µm, where it was expected to find the EVs. As described in the previous paragraph, they were stained with CFSE dye, to point out the green cytoplasm, and used the fluorescent signal to distinguish them from the background noise. Moreover, we added an equal amount of CountBright™ Absolute Counting Beads (Life technologies, ThermoFisher), equal to 1000, to each sample, to analyse the same volume of EVs, equal to 20 µl. EVs were analysed with FACS LSR FORTESSA X-20 (BD PharMigen, BD Biosciences, San Jose, CA) and data were obtained by using the FACS DIVA 8.0 software (BD PharMigen, BD Biosciences).

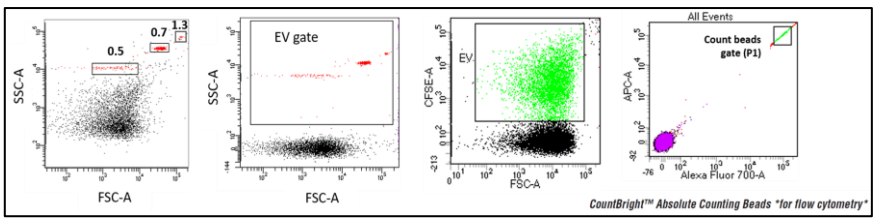

Figure 44. Schematic of the flowcytometric analysis for the visualization of EVs.

6.3.4. C2C12 cell line culture

C2C12 skeletal muscle cell line was obtained from Fondazione Santa Lucia (Rome, Italy). In detail, they were seeded at a density of 7500 cells/well in 24-well plates and were maintained as

proliferating myoblasts in Dulbecco's Modified Medium (DMEM-high glucose, w/o sodium pyruvate) supplemented by 10 % of Fetal Bovine Serum (FBS), 1 % of penicillin/streptomycin and 2 % of l-glutamine until a confluence of 70-80 % was reached. To induce myoblasts' fusion, confluent cultures were switched (Day 0) to the differentiation medium Dulbecco's Modified Medium (DMEM-high glucose, w/o sodium pyruvate) supplemented by 2 % of Horse serum (HS), 1 % of penicillin/streptomycin and 2 % of l-glutamine). C2C12 cells grown at 37 °C in a humidified 5 % CO_2 95 % O_2 air atmosphere, and differentiated for 5 days (Day 4), as reported in literature [131].

6.3.5. Uptake of mouse blood extracellular vesicles by myoblasts and myotubes

To evaluate the uptake of mouse blood EVs by C2C12 proliferating cells and by completely differentiated myotubes, $CFSE^+$ EVs were first collected. Thereafter, 5 µl/well of labelled EVs were added to proliferating myoblasts and to completely differentiated myotubes (Day 4), and incubated for 6 hours at 5 % CO2 95 % O_2 at 37 °C. Subsequently, wells were gently washed 2 times with PBS, fixed with 4 % paraformaldehyde (PFA) for 10 min for consequent confocal microscopy analysis.

6.3.6. Evaluation of the functional effects of mouse blood extracellular vesicles on C2C12 cell line

To evaluate the functional effects of mouse blood EVs on C2C12 cells during the myogenic differentiation process, cells were treated with EVs derived from $SOD1^{G93A}$ mice at the pre-symptomatic, onset and end-stage of the disease and from age-matched WT mice. In detail, when the growth medium was shifted to the differentiation one (Day 0), C2C12 cells were treated by adding 5 µl of EVs to each well of the 24-wells plate. To fully characterize their effects on the differentiation process, the C2C12

cells were stopped in the middle (Day 2) and at the end (Day 4) of the myogenic process to perform confocal microscopy analysis.

6.3.7. Immunolabeling and confocal microscopy analysis

After the treatment with mouse blood EVs, wells were gently washed 2 times with PBS, fixed with 4 % paraformaldehyde (PFA) for 10 min and blocked for 20 min with 1 % BSA and 0.2 % Triton-X in PBS. Then, wells were incubated for 45 min at RT in 1 % Goat Serum in CMF. To evaluate the uptake of $CFSE^+$ EVs by proliferating C2C12 cells, immunofluorescence analysis was performed. Hoechst was used for nuclear staining. On the other hand, to evaluate the uptake of $CFSE^+$ EVs by myotubes and the functional effects of EVs by C2C12 cells during the differentiation process, MF20 and Hoechst were employed for myosin and nuclear staining, respectively. Briefly, MF20 primary antibody diluted in 1.5 % Goat Serum in CMF was added to the wells and incubated overnight at 4° C. The wells were washed thrice with 1 % BSA and 0.2 % Triton-X in PBS. Alexa568 secondary antibody and Hoechst 1:1000 diluted in 1.5 % Goat Serum in CMF were added to the wells for 45 min at RT. The confocal microscopy analysis was then performed on a Zeiss LSM 900 laser-scanning confocal microscope. As regards the evaluation of uptake of $CFSE^+$ EVs, for proliferating C2C12 cells a Field of View (FOV) was acquired for each well using a 40x oil-immersion objective, while for differentiated myotubes, consequent images were acquired for each well using a 40x oil-immersion objective and a step-size of 0.5 µm. The mean fluorescent intensity (MFI) of CFSE was measured using ImageJ software on the digital images acquired for each sample. On the other hand, to evaluate the functional effects of EVs on C2C12 cells during the differentiation process, two FOVs were acquired for each well with a 20x objective at Day 2 and 10x objective and at Day 4, respectively. For each sample, with the aim of evaluating the effects of EVs after two days of myogenic differentiation, we calculated the number of nuclei, the number of $MF20^+$ cells and the differentiation

index, as the ratio between the number of $MF20^{+}$ cells and the number of nuclei, by using the ImageJ software [132]. On the other hand, for Day 4, we computed the fusion index, as the ratio between the number of myotubes and the number of nuclei, and the differentiation index, as the ratio between the number of nuclei per myotubes and the number of nuclei, by using ImageJ software [132].

6.4 Statistical analysis

For the development of techniques, experimental devices and testing protocols of the muscle and neuromuscular junction functionality, statistical differences were evaluated by using different tests. For the evaluation of the errors introduced by testing muscle to lift the reference optimal force rather than the experimental one, differences in fatigue time, mechanical work and power of the muscles tested at the experimental and reference optimal force were evaluated with un-paired Student's t-test. Differences in all the parameters computed for direct and indirect stimulations in WT animals were evaluated with unpaired Student's t-test, as well as differences in the parameters computed for WT and $SOD1^{G93A}$ mice during fatigue test, namely INF at 50%, INF at 80% and T_{Fat}. The distribution of all these parameters was parametric. For the measurement of NMJ functionality in $SOD1^{G93A}$ mice during Amyotrophic Lateral Sclerosis, we referred to Analysis of Variance to identity any significant differences between the means of tested groups, since a continuous outcome on the basis of categorical variables was studied. Differences in muscle mass, CSA, Intratrain Fatigue, Neurotransmission failure, fatigue time and *Isotonic Neurotransmission Failure* were evaluated with two-way ANOVA using the factors *animal strain* and *disease stage* as fixed ones. We used three-way ANOVA, followed by multiple comparisons, to analyse differences in contractile kinetics parameters (dF/dt, -dF/dt), tetanic force, specific tetanic force and maximum velocity using the factors *animal strain*, *disease stage* and *type of stimulation* as fixed ones. As regarding the development of the 3D embedded system for

the measurement of engineered skeletal muscle contractile force, the linear relationship between the force measured by the micro-force transducer and the displacements imposed by the linear actuator was assessed by linear regression with p-value fixed at 0.05, with reference to the average value of the measured force across the 10 repetitions for each displacement in input. One-way ANOVA, followed by multiple comparison, was performed to look for differences in all the measured parameters across the five days, i.e. assuming the *day* as the fixed factor, for the un-treated group and for the specific twitch force and the maximum tetanic force for the treated group. Two-way ANOVA was performed assuming the *day* and the *treatment* as fixed factors, followed by a multiple comparison test to look for differences in the specific force at all the tested frequencies, including twitch test. Of note, three treated tissues "almost died" during the "accelerated aging" treatment, and their generated force was therefore null for the remaining testing days. For these samples, it was not possible to measure TTP and 1/2RT on day 3 and day 4. For the development of 3D microfluidic device, one-way ANOVA test was used to find differences in Acetylcholine receptors β1 and β2, while differences in Acetylcholine receptors ɤ and ε were evaluated with Student's t-test. For the evaluation of the electric field intensity along the microfluidic device for the best electrodes' configuration, two-way ANOVA tests were performed, assuming *pin position* and *pin radius* as fixed factors, for each applied voltage, followed by multiple comparisons tests to look for differences in the electric field values. One-way ANOVA was used to evaluate differences in the number of nuclei and neurofilaments' length after the electrical stimulation considering the *electrical stimulation* as fixed factor.

For the molecular characterization and functional effects of $SOD1^{G93A}$ mouse EVs on C2C12 cell line, differences in the normalized number of EVs and mean fluorescence intensity (MFI), both for C2C12 proliferating cells and completely differentiated myotubes, were evaluated with Mann-Whitney test. The distribution of these parameters was not parametric. In addition, differences in

the differentiation index and fusion index were computed though one-way ANOVA considering the *treatment* as fixed factor.

Generally, for two-way and three-way ANOVA, the distribution of the analysed parameters was not parametric.

Statistical analysis was performed with GraphPad 8.0 and differences were considered significantly when p-value was lower than 0.05. Values are generally expressed as mean ± SD, except for NF and IF whose values are expressed as mean ± SEM.

7. References

[1] L. Dupuis and J. P. Loeffler, "Neuromuscular junction destruction during amyotrophic lateral sclerosis: insights from transgenic models," *Curr. Opin. Pharmacol.*, vol. 9, pp. 341–346, 2009, doi: 10.1016/j.coph.2009.03.007.

[2] A. E. Renton, A. Chiò, and B. J. Traynor, "State of play in amyotrophic lateral sclerosis genetics HHS Public Access Author manuscript," *Nat Neurosci*, vol. 17, no. 1, pp. 17–23, 2014, doi: 10.1038/nn.3584.State.

[3] P. Pasinelli and R. H. Brown, "Molecular biology of amyotrophic lateral sclerosis: Insights from genetics," *Nat. Rev. Neurosci.*, vol. 7, no. 9, pp. 710–723, 2006, doi: 10.1038/nrn1971.

[4] M. Dadon-Nachum, E. Melamed, and D. Offen, "The 'dying-back' phenomenon of motor neurons in ALS," *J. Mol. Neurosci.*, vol. 43, no. 3, pp. 470–477, 2011, doi: 10.1007/s12031-010-9467-1.

[5] D. Krakora, C. MacRander, and M. Suzuki, "Neuromuscular junction protection for the potential treatment of amyotrophic lateral sclerosis," *Neurology Research International*, vol. 2012. 2012, doi: 10.1155/2012/379657.

[6] G. Dobrowolny *et al.*, "Skeletal Muscle Is a Primary Target of SOD1G93A-Mediated Toxicity," *Cell Metab.*, vol. 8, no. 5, pp. 425–436, 2008, doi: 10.1016/j.cmet.2008.09.002.

[7] A. Alhindi, I. Boehm, and H. Chaytow, "Small junction, big problems: Neuromuscular junction pathology in mouse models of amyotrophic lateral sclerosis (ALS)," *J. Anat.*, no. February, pp. 1–19, 2021, doi: 10.1111/joa.13463.

[8] V. Cappello and M. Francolini, "Neuromuscular junction dismantling in amyotrophic lateral sclerosis," *Int. J. Mol. Sci.*, vol. 18, no. 10, 2017, doi: 10.3390/ijms18102092.

[9] L. C. Wijesekera and P. N. Leigh, "Amyotrophic lateral sclerosis," *Orphanet J. Rare Dis.*, vol. 4, no. 1, pp. 1–22, 2009, doi: 10.1186/1750-1172-4-3.

[10] D. R. Rosen *et al.*, "Mutations in Cu/Zn superoxide dismutase gene are associated with familial amyotrophic lateral sclerosis," *Nature*, 1993, doi: 10.1038/362059a0.
[11] P. H. Gordon, "Amyotrophic lateral sclerosis: Pathophysiology, diagnosis and management," *CNS Drugs*, vol. 25, no. 1, pp. 1–15, 2011, doi: 10.2165/11586000-000000000-00000.
[12] M. E. Ripps, G. W. Huntley, P. R. Hof, J. H. Morrison, and J. W. Gordon, "Transgenic mice expressing an altered murine superoxide dismutase gene provide an animal model of amyotrophic lateral sclerosis," *Proc. Natl. Acad. Sci. U. S. A.*, vol. 92, no. 3, pp. 689–693, 1995, doi: 10.1073/pnas.92.3.689.
[13] M. E. Gurney *et al.*, "Motor neuron degeneration in mice that express a human Cu,Zn superoxide dismutase mutation," *Science (80-.).*, vol. 264, no. 5166, pp. 1772–1775, 1994, doi: 10.1126/science.8209258.
[14] A. G. Reaume *et al.*, "Death After Axonal Injury," vol. 13, no. may, pp. 43–47, 1996.
[15] S. R. Iyer, S. B. Shah, and R. M. Lovering, "The neuromuscular junction: Roles in aging and neuromuscular disease," *Int. J. Mol. Sci.*, vol. 22, no. 15, 2021, doi: 10.3390/ijms22158058.
[16] S. Boillée *et al.*, "Onset and progression in inherited ALS determined by motor neurons and microglia," *Science (80-.).*, vol. 312, no. 5778, pp. 1389–1392, 2006, doi: 10.1126/science.1123511.
[17] F. Achilli *et al.*, "The SOD1 transgene in the G93A mouse model of amyotrophic lateral sclerosis lies on distal mouse chromosome 12," *Amyotroph. Lateral Scler. Other Mot. Neuron Disord.*, vol. 6, no. 2, pp. 111–114, 2005, doi: 10.1080/14660820510035351.
[18] S. Vinsant *et al.*, "Characterization of early pathogenesis in the SOD1G93A mouse model of ALS: Part I, background and methods," *Brain Behav.*, vol. 3, no. 4, pp. 335–350, 2013, doi:

10.1002/brb3.143.
[19] S. Vinsant *et al.*, "Characterization of early pathogenesis in the SOD1G93A mouse model of ALS: Part II, results and discussion," *Brain Behav.*, vol. 3, no. 4, pp. 431–457, 2013, doi: 10.1002/brb3.142.
[20] J. Hegedus, C. T. Putman, and T. Gordon, "Time course of preferential motor unit loss in the SOD1G93A mouse model of amyotrophic lateral sclerosis," *Neurobiol. Dis.*, vol. 28, no. 2, pp. 154–164, 2007, doi: 10.1016/j.nbd.2007.07.003.
[21] J. Hegedus, C. T. Putman, N. Tyreman, and T. Gordon, "Preferential motor unit loss in the SOD1 G93A transgenic mouse model of amyotrophic lateral sclerosis," *J. Physiol.*, vol. 586, no. 14, pp. 3337–3351, 2008, doi: 10.1113/jphysiol.2007.149286.
[22] W. Derave, L. Van Den Bosch, G. Lemmens, B. O. Eijnde, W. Robberecht, and P. Hespel, "Skeletal muscle properties in a transgenic mouse model for amyotrophic lateral sclerosis: Effects of creatine treatment," *Neurobiol. Dis.*, vol. 13, no. 3, pp. 264–272, 2003, doi: 10.1016/S0969-9961(03)00041-X.
[23] A. R. Punga and M. A. Ruegg, "Signaling and aging at the neuromuscular synapse: Lessons learnt from neuromuscular diseases," *Curr. Opin. Pharmacol.*, vol. 12, no. 3, pp. 340–346, 2012, doi: 10.1016/j.coph.2012.02.002.
[24] T. K. Aldrich, A. Shander, I. Chaudhry, and H. Nagashima, "Fatigue of isolated rat diaphragm: role of impaired neuromuscular transmission," *J. Appl. Physiol.*, vol. 61, no. 3, pp. 1077–1083, 1986, doi: 10.1152/JAPPL.1986.61.3.1077.
[25] S. Boyas and A. Guével, "Neuromuscular fatigue in healthy muscle: Underlying factors and adaptation mechanisms," *Ann. Phys. Rehabil. Med.*, vol. 54, no. 2, pp. 88–108, 2011, doi: 10.1016/j.rehab.2011.01.001.
[26] M. J. Fogarty, M. A. G. Porras, C. B. Mantilla, and G. C. Sieck, "Diaphragm neuromuscular transmission failure in aged rats," *J. Neurophysiol.*, vol. 122, no. 1, pp. 93–104,

2019, doi: 10.1152/jn.00061.2019.
[27] M. J. Fogarty, G. C. Sieck, and J. E. Brandenburg, “Impaired neuromuscular transmission of the tibialis anterior in a rodent model of hypertonia,” *J. Neurophysiol.*, vol. 123, no. 5, pp. 1869–2020, 2020, doi: 10.1152/jn.00095.2020.
[28] K. E. Personius and R. P. Sawyer, “Variability and failure of neurotransmission in the diaphragm of mdx mice,” *Neuromuscul. Disord.*, vol. 16, no. 3, pp. 168–177, 2006, doi: 10.1016/j.nmd.2006.01.002.
[29] S. Pisu, E. Rizzuto, A. Musaro, and Z. Del Prete, “Identification of the best stimulation parameters to measure in situ the comunication between muscle and nerve in mouse Tibialis muscle,” in *2017 IEEE International Symposium on Medical Measurements and Applications, MeMeA 2017 - Proceedings*, 2017, pp. 143–147, doi: 10.1109/MeMeA.2017.7985865.
[30] E. Van Lunteren and M. Moyer, “Effects of DAP on diaphragm force and fatigue, including fatigue due to neurotransmission failure,” *J. Appl. Physiol.*, vol. 81, no. 5, pp. 2214–2220, 1996, doi: 10.1152/jappl.1996.81.5.2214.
[31] E. Rizzuto, S. Pisu, A. Musarò, and Z. Del Prete, “Measuring Neuromuscular Junction Functionality in the SOD1G93A Animal Model of Amyotrophic Lateral Sclerosis,” *Ann. Biomed. Eng.*, vol. 43, no. 9, pp. 2196–2206, Sep. 2015, doi: 10.1007/s10439-015-1259-x.
[32] M. E. Cummins, R. S. Soomal, and N. A. Curtin, “Fatigue of Isolated Mouse Muscle Due To Isometric Tetani and Tetani With High Power Output,” *Q. J. Exp. Physiol.*, vol. 74, no. 6, pp. 951–953, 1989, doi: 10.1113/expphysiol.1989.sp003367.
[33] Z. Del Prete, A. Musarò, and E. Rizzuto, “Measuring mechanical properties, including isotonic fatigue, of fast and slow MLC/mIgf-1 transgenic skeletal muscle,” *Ann. Biomed. Eng.*, vol. 36, no. 7, pp. 1281–1290, Jul. 2008, doi: 10.1007/s10439-008-9496-x.
[34] H. Roots, G. Ball, J. Talbot-Ponsonby, M. King, K. McBeath,

and K. W. Ranatunga, “Muscle fatigue examined at different temperatures in experiments on intact mammalian (rat) muscle fibers,” *J. Appl. Physiol.*, vol. 106, no. 2, pp. 378–384, 2009, doi: 10.1152/japplphysiol.90883.2008.

[35] A. V. HILL, “the Effect of Load on the Heat of Shortening of Muscle.,” *Proc. R. Soc. London. Ser. B, Contain. Pap.*, vol. 159, pp. 297–318, 1964, doi: 10.1098/rspb.1964.0004.

[36] M. Munkvik, P. K. Lunde, and O. M. Sejersted, “Causes of fatigue in slow-twitch rat skeletal muscle during dynamic activity,” *Am. J. Physiol. - Regul. Integr. Comp. Physiol.*, vol. 297, no. 3, pp. 900–910, 2009, doi: 10.1152/ajpregu.91043.2008.

[37] C. Y. Seow and N. L. Stephens, “Fatigue of mouse diaphragm muscle in isometric and isotonic contractions,” *J. Appl. Physiol.*, 1988, doi: 10.1152/jappl.1988.64.6.2388.

[38] P. Vedsted, A. H. Larsen, K. Madsen, and G. Sjøgaard, “Muscle performance following fatigue induced by isotonic and quasi-isometric contractions of rat extensor digitorum longus and soleus muscles in vitro,” *Acta Physiol. Scand.*, vol. 178, no. 2, pp. 175–186, 2003, doi: 10.1046/j.1365-201X.2003.01123.x.

[39] J. L. Olson, A. Atala, and J. J. Yoo, “Tissue Engineering: Current Strategies and Future Directions,” *Chonnam Med. J.*, vol. 47, no. 1, p. 1, 2011, doi: 10.4068/cmj.2011.47.1.1.

[40] F. Boschetti, “Tissue Mechanics and Tissue Engineering,” *Appl. Sci.*, vol. 12, no. 13, pp. 10–11, 2022, doi: 10.3390/app12136664.

[41] L. G. Karagounis and J. A. Hawley, “Skeletal muscle: Increasing the size of the locomotor cell,” *Int. J. Biochem. Cell Biol.*, vol. 42, no. 9, pp. 1376–1379, 2010, doi: 10.1016/j.biocel.2010.05.013.

[42] R. Rudolf, M. M. Khan, S. Labeit, and M. R. Deschenes, “Degeneration of neuromuscular junction in age and dystrophy,” *Front. Aging Neurosci.*, vol. 6, p. 99, 2014, doi: 10.3389/fnagi.2014.00099.

[43] W. Hadj-Saïd *et al.*, "Effect of locomotor training on muscle performance in the context of nerve-muscle communication dysfunction," *Muscle and Nerve*, vol. 45, no. 4, pp. 567–577, 2012, doi: 10.1002/mus.22332.
[44] M. S. Kang, S. H. Lee, W. J. Park, J. E. Lee, B. Kim, and D. W. Han, "Advanced techniques for skeletal muscle tissue engineering and regeneration," *Bioengineering*, 2020, doi: 10.3390/bioengineering7030099.
[45] S. Guettier-Sigrist, G. Coupin, S. Braun, J. M. Warter, and P. Poindron, "Muscle could be the therapeutic target in SMA treatment," *J. Neurosci. Res.*, vol. 53, no. 6, pp. 663–9, 1998, doi: 10.1002/(SICI)1097-4547(19980915)53:6<663::AID-JNR4>3.0.CO;2-3.
[46] A. Khodabukus *et al.*, "Tissue-engineered human myobundle system as a platform for evaluation of skeletal muscle injury biomarkers," *Toxicol. Sci.*, vol. 176, pp. 124–136, 2020, doi: 10.1093/toxsci/kfaa049.
[47] A. Khodabukus, "Tissue-Engineered Skeletal Muscle Models to Study Muscle Function, Plasticity, and Disease," *Front. Physiol.*, vol. 12, 2021, doi: 10.3389/fphys.2021.619710.
[48] J. Kim, J. S. Kong, W. Han, B. S. Kim, and D. W. Cho, "3d cell printing of tissue/organ-mimicking constructs for therapeutic and drug testing applications," *Int. J. Mol. Sci.*, vol. 21, no. 20, p. 7757, 2020, doi: 10.3390/ijms21207757.
[49] P. Bédard *et al.*, "Innovative human three-dimensional tissue-engineered models as an alternative to animal testing," *Bioengineering*, vol. 7, no. 3, pp. 1–40, 2020, doi: 10.3390/bioengineering7030115.
[50] S. Carosio, L. Barberi, E. Rizzuto, C. Nicoletti, Z. Del Prete, and A. Musarò, "Generation of eX vivo-vascularized Muscle Engineered Tissue (X-MET)," *Sci. Rep.*, vol. 3, 2013, doi: 10.1038/srep01420.
[51] E. Rizzuto, S. Carosio, M. Faraldi, S. Pisu, A. Musarò, and Z. Del Prete, "A DIC Based Technique to Measure the Contraction of a Skeletal Muscle Engineered Tissue," *Appl.*

Bionics Biomech., 2016, doi: 10.1155/2016/7465095.

[52] S. Pisu, M. Cosentino, L. Apa, A. Musarò, E. Rizzuto, and Z. Del Prete, "Measuring the Maximum Power of an ex vivo Engineered Muscle Tissue with Isovelocity Shortening Technique," *IEEE Trans. Instrum. Meas.*, 2019, doi: 10.1109/TIM.2019.2904071.

[53] A. Alave Reyes-Furrer *et al.*, "Matrigel 3D bioprinting of contractile human skeletal muscle models recapitulating exercise and pharmacological responses," *Commun. Biol.*, vol. 4, no. 1, pp. 1–12, 2021, doi: 10.1038/s42003-021-02691-0.

[54] M. C. Turner *et al.*, "Physiological and pathophysiological concentrations of fatty acids induce lipid droplet accumulation and impair functional performance of tissue engineered skeletal muscle," *J. Cell. Physiol.*, vol. 236, no. 10, pp. 7033–7044, 2021, doi: 10.1002/jcp.30365.

[55] D. Sasaki, K. Matsuura, H. Seta, Y. Haraguchi, T. Okano, and T. Shimizu, "Contractile force measurement of human induced pluripotent stem cell-derived cardiac cell sheet-tissue," *PLoS One*, vol. 13, no. 5, pp. 1–21, 2018, doi: 10.1371/journal.pone.0198026.

[56] K. Wilson, M. Das, K. J. Wahl, R. J. Colton, and J. Hickman, "Measurement of contractile stress generated by cultured rat muscle on silicon cantilevers for toxin detection and muscle performance enhancement," *PLoS One*, vol. 5, no. 6, 2010, doi: 10.1371/journal.pone.0011042.

[57] A. Gaitas, R. Malhotra, T. Li, T. Herron, and J. Jalife, "A device for rapid and quantitative measurement of cardiac myocyte contractility," *Rev. Sci. Instrum.*, vol. 86, no. 3, 2015, doi: 10.1063/1.4915500.

[58] K. Shimizu *et al.*, "Assembly of skeletal muscle cells on a Si-MEMS device and their generative force measurement," *Biomed. Microdevices*, vol. 12, no. 2, pp. 247–252, 2010, doi: 10.1007/s10544-009-9379-4.

[59] M. Rausch *et al.*, "Measurement of Skeletal Muscle Fiber

Contractility with High-Speed Traction Microscopy," *Biophys. J.*, vol. 118, no. 3, pp. 657–666, 2020, doi: 10.1016/j.bpj.2019.12.014.

[60] F. S. Pasqualini, A. Agarwal, B. B. O'Connor, Q. Liu, S. P. Sheehy, and K. K. Parker, "Traction force microscopy of engineered cardiac tissues," *PLoS One*, 2018, doi: 10.1371/journal.pone.0194706.

[61] A. Pasquarelli, "Microelectrode Arrays, Implants, and Organs-on-a-Chip," *Biosens. Biochips*, pp. 291–322, 2021, doi: 10.1007/978-3-030-76469-2_11.

[62] L. Sala *et al.*, "Musclemotion: A versatile open software tool to quantify cardiomyocyte and cardiac muscle contraction in vitro and in vivo," *Circ. Res.*, vol. 122, no. 3, pp. e5–e16, 2018, doi: 10.1161/CIRCRESAHA.117.312067.

[63] T. Bruegmann *et al.*, "Optogenetic control of heart muscle in vitro and in vivo," *Nat. Methods*, vol. 7, pp. 897–900, 2010, doi: 10.1038/nmeth.1512.

[64] O. F. Vila, Y. Qu, and G. Vunjak-Novakovic, "In vitro models of neuromuscular junctions and their potential for novel drug discovery and development," *Expert Opin. Drug Discov.*, vol. 15, no. 3, pp. 307–317, 2020, doi: 10.1080/17460441.2020.1700225.

[65] S. G. M. Uzel *et al.*, "Microfluidic device for the formation of optically excitable, three-dimensional, compartmentalized motor units," *Sci. Adv.*, vol. 2, no. 8, 2016, doi: 10.1126/sciadv.1501429.

[66] E. Frank and G. D. Fischbach, "Early events in neuromuscular junction formation in vitro. Induction of acetylcholine receptor clusters in the postsynaptic membrane and morphology of newly formed synapses," *J. Cell Biol.*, vol. 83, no. 1, pp. 143–158, 1979, doi: 10.1083/jcb.83.1.143.

[67] E. M. Ullian, B. T. Harris, A. Wu, J. R. Chan, and B. A. Barres, "Schwann cells and astrocytes induce synapse formation by spinal motor neurons in culture," *Mol. Cell. Neurosci.*, vol. 25, no. 2, pp. 241–251, 2004, doi:

10.1016/j.mcn.2003.10.011.

[68] X. Guo, M. Das, J. Rumsey, M. Gonzalez, M. Stancescu, and J. Hickman, "Neuromuscular junction formation between human stem-cell-derived motoneurons and rat skeletal muscle in a defined system," *Tissue Eng. - Part C Methods*, vol. 16, no. 6, pp. 1347–1355, 2010, doi: 10.1089/ten.tec.2010.0040.

[69] E. R. Peterson and S. M. Crain, "Innervation in cultures of fetal rodent skeletal muscle by organotypic explants of spinal cord from different animals," *Zeitschrift für Zellforsch. und Mikroskopische Anat.*, vol. 106, no. 1, pp. 1–21, 1970, doi: 10.1007/BF01027714.

[70] M. Das, J. W. Rumsey, N. Bhargava, M. Stancescu, and J. J. Hickman, "A Defined Long-Term In Vitro Tissue Engineered Model of Neuromuscular Junctions," *Biomaterials*, vol. 31, no. 18, p. 4880, Jun. 2010, doi: 10.1016/J.BIOMATERIALS.2010.02.055.

[71] P. H. Chipman, Y. Zhang, and V. F. Rafuse, "A stem-cell based bioassay to critically assess the pathology of dysfunctional neuromuscular junctions," *PLoS One*, vol. 9, no. 3, 2014, doi: 10.1371/journal.pone.0091643.

[72] M. Demestre *et al.*, "Formation and characterisation of neuromuscular junctions between hiPSC derived motoneurons and myotubes," *Stem Cell Res.*, vol. 15, no. 2, pp. 328–336, 2015, doi: 10.1016/j.scr.2015.07.005.

[73] A. Natarajan, A. Sethumadhavan, and U. M. Krishnan, "Toward building the neuromuscular junction: In vitro models to study synaptogenesis and neurodegeneration," *ACS Omega*, vol. 4, no. 7, pp. 12969–12977, 2019, doi: 10.1021/acsomega.9b00973.

[74] H. Vandenburgh *et al.*, "Drug-screening platform based on the contractility of tissue-engineered muscle," *Muscle and Nerve*, vol. 37, no. 4, pp. 438–447, 2008, doi: 10.1002/mus.20931.

[75] V. Mudera, A. S. T. Smith, M. A. Brady, and M. P. Lewis,

"The effect of cell density on the maturation and contractile ability of muscle derived cells in a 3D tissue-engineered skeletal muscle model and determination of the cellular and mechanical stimuli required for the synthesis of a postural phenotype," *J. Cell. Physiol.*, vol. 225, no. 3, pp. 646–653, 2010, doi: 10.1002/jcp.22271.

[76] K. Mukund and S. Subramaniam, "Skeletal muscle: A review of molecular structure and function, in health and disease," *Wiley Interdiscip. Rev. Syst. Biol. Med.*, vol. 12, no. 1, pp. 1–46, 2020, doi: 10.1002/wsbm.1462.

[77] Y. Morimoto, M. Kato-Negishi, H. Onoe, and S. Takeuchi, "Three-dimensional neuron-muscle constructs with neuromuscular junctions," *Biomaterials*, vol. 34, no. 37, pp. 9413–9419, 2013, doi: 10.1016/j.biomaterials.2013.08.062.

[78] M. A. Bakooshli *et al.*, "A three-dimensional culture model of innervated human skeletal muscle enables studies of the adult neuromuscular junction and disease modeling," *bioRxiv*, pp. 1–29, 2018.

[79] M. Yoshida *et al.*, "Modeling the early phenotype at the neuromuscular junction of spinal muscular atrophy using patient-derived iPSCs," *Stem Cell Reports*, vol. 4, no. 4, pp. 561–568, 2015, doi: 10.1016/j.stemcr.2015.02.010.

[80] T. Osaki, S. G. M. Uzel, and R. D. Kamm, "Microphysiological 3D model of amyotrophic lateral sclerosis (ALS) from human iPS-derived muscle cells and optogenetic motor neurons," *Sci. Adv.*, vol. 4, no. 10, pp. 1–16, 2018, doi: 10.1126/sciadv.aat5847.

[81] O. F. Vila *et al.*, "Quantification of human neuromuscular function through optogenetics," *Theranostics*, vol. 9, no. 5, pp. 1232–1246, 2019, doi: 10.7150/thno.25735.

[82] D. Ferrara, L. Pasetto, V. Bonetto, and M. Basso, "Role of extracellular vesicles in amyotrophic lateral sclerosis," *Frontiers in Neuroscience*. 2018, doi: 10.3389/fnins.2018.00574.

[83] G. Raposo and W. Stoorvogel, "Extracellular vesicles:

Exosomes, microvesicles, and friends," *Journal of Cell Biology*. 2013, doi: 10.1083/jcb.201211138.

[84] E. Anakor *et al.*, "The Neurotoxicity of Vesicles Secreted by ALS Patient Myotubes Is Specific to Exosome-like and Not Larger Subtypes," *Cells*, vol. 11, no. 5, 2022, doi: 10.3390/cells11050845.

[85] M. Yáñez-Mó *et al.*, "Biological properties of extracellular vesicles and their physiological functions," *J. Extracell. Vesicles*, vol. 4, no. 2015, pp. 1–60, 2015, doi: 10.3402/jev.v4.27066.

[86] C. Gomes, S. Keller, P. Altevogt, and J. Costa, "Evidence for secretion of Cu,Zn superoxide dismutase via exosomes from a cell model of amyotrophic lateral sclerosis," *Neurosci. Lett.*, vol. 428, no. 1, pp. 43–46, 2007, doi: 10.1016/j.neulet.2007.09.024.

[87] O. LA, S. A, and B. JS, "乳鼠心肌提取 HHS Public Access," *Physiol. Behav.*, vol. 176, no. 5, pp. 139–148, 2017, doi: 10.1002/jnr.23798.PORT-TO-PORT.

[88] M. Sardar Sinha *et al.*, "Alzheimer's disease pathology propagation by exosomes containing toxic amyloid-beta oligomers," *Acta Neuropathol.*, vol. 136, no. 1, pp. 41–56, 2018, doi: 10.1007/s00401-018-1868-1.

[89] M. Mathieu, L. Martin-Jaular, G. Lavieu, and C. Théry, "Specificities of secretion and uptake of exosomes and other extracellular vesicles for cell-to-cell communication," *Nat. Cell Biol.*, vol. 21, no. 1, pp. 9–17, 2019, doi: 10.1038/s41556-018-0250-9.

[90] E. Anakor, L. Le Gall, J. Dumonceaux, W. J. Duddy, and S. Duguez, "Exosomes in ageing and motor neurone disease: Biogenesis, uptake mechanisms, modifications in disease and uses in the development of biomarkers and therapeutics," *Cells*, vol. 10, no. 11, 2021, doi: 10.3390/cells10112930.

[91] A. Di Credico, P. Izzicupo, G. Gaggi, A. Di Baldassarre, and B. Ghinassi, "Effect of physical exercise on the release of microparticles with angiogenic potential," *Appl. Sci.*, vol. 10,

no. 14, pp. 1–19, 2020, doi: 10.3390/app10144871.
[92] M. Battistelli and E. Falcieri, “Apoptotic bodies: Particular extracellular vesicles involved in intercellular communication,” *Biology (Basel).*, vol. 9, no. 1, 2020, doi: 10.3390/biology9010021.
[93] M. P. Caby, D. Lankar, C. Vincendeau-Scherrer, G. Raposo, and C. Bonnerot, “Exosomal-like vesicles are present in human blood plasma,” *Int. Immunol.*, vol. 17, no. 7, pp. 879–887, 2005, doi: 10.1093/intimm/dxh267.
[94] T. Pisitkun, R. F. Shen, and M. A. Knepper, “Identification and proteomic profiling of exosomes in human urine,” *Proc. Natl. Acad. Sci. U. S. A.*, vol. 101, no. 36, pp. 13368–13373, 2004, doi: 10.1073/pnas.0403453101.
[95] Y. Ogawa *et al.*, “Proteomic analysis of two types of exosomes in human whole saliva,” *Biol. Pharm. Bull.*, vol. 34, no. 1, pp. 13–23, 2011, doi: 10.1248/bpb.34.13.
[96] G. Casella *et al.*, “Extracellular Vesicles Containing IL-4 Modulate Neuroinflammation in a Mouse Model of Multiple Sclerosis,” *Mol. Ther.*, vol. 26, no. 9, pp. 2107–2118, 2018, doi: 10.1016/j.ymthe.2018.06.024.
[97] L. Rajendran *et al.*, “Alzheimer’s disease β-amyloid peptides are released in association with exosomes,” *Proc. Natl. Acad. Sci. U. S. A.*, vol. 103, no. 30, pp. 11172–11177, 2006, doi: 10.1073/pnas.0603838103.
[98] L. I. Grad *et al.*, “Intercellular propagated misfolding of wild-type Cu/Zn superoxide dismutase occurs via exosome-dependent and -independent mechanisms,” *Proc. Natl. Acad. Sci. U. S. A.*, vol. 111, no. 9, pp. 3620–3625, 2014, doi: 10.1073/pnas.1312245111.
[99] L. Le Gall *et al.*, “Optimized method for extraction of exosomes from human primary muscle cells,” *Skelet. Muscle*, vol. 10, no. 1, pp. 1–13, 2020, doi: 10.1186/s13395-020-00238-1.
[100] D. Sproviero *et al.*, “Pathological proteins are transported by extracellular vesicles of sporadic amyotrophic lateral

sclerosis patients," *Front. Neurosci.*, 2018, doi: 10.3389/fnins.2018.00487.

[101] J. M. Silverman *et al.*, "CNS-derived extracellular vesicles from superoxide dismutase 1 (SOD1)G93A ALS mice originate from astrocytes and neurons and carry misfolded SOD1," *J. Biol. Chem.*, 2019, doi: 10.1074/jbc.RA118.004825.

[102] L. Le Gall *et al.*, "Muscle cells of sporadic amyotrophic lateral sclerosis patients secrete neurotoxic vesicles," *J. Cachexia. Sarcopenia Muscle*, vol. 13, no. 2, pp. 1385–1402, 2022, doi: 10.1002/jcsm.12945.

[103] C. P. Yang *et al.*, "Muscle atrophy-related myotube-derived exosomal microRNA in neuronal dysfunction: Targeting both coding and long noncoding RNAs," *Aging Cell*, vol. 19, no. 5, pp. 1–16, 2020, doi: 10.1111/acel.13107.

[104] M. Rizzuti *et al.*, "Insights into the identification of a molecular signature for amyotrophic lateral sclerosis exploiting integrated microRNA profiling of iPSC-derived motor neurons and exosomes," *Cell. Mol. Life Sci.*, vol. 79, no. 3, 2022, doi: 10.1007/s00018-022-04217-1.

[105] F. Forconi, F. Martelli, S. Pisu, A. Musaro, E. Rizzuto, and Z. Del Prete, "Optimal force evaluation for isotonic fatigue characterization in mouse Tibialis Anterior muscle," in *IEEE Medical Measurements and Applications, MeMeA 2020 - Conference Proceedings*, 2020, doi: 10.1109/MeMeA49120.2020.9137316.

[106] F. Forconi *et al.*, "Development of a Novel Technique for the Measurement of Neuromuscular Junction Functionality in Isotonic Conditions," *Cell. Mol. Bioeng.*, vol. 15, no. 3, pp. 255–265, 2022, doi: 10.1007/s12195-022-00721-3.

[107] S. M. Greising, L. G. Ermilov, G. C. Sieck, and C. B. Mantilla, "Ageing and neurotrophic signalling effects on diaphragm neuromuscular function," *J. Physiol.*, vol. 593, no. Pt 2, p. 431, Jan. 2015, doi: 10.1113/JPHYSIOL.2014.282244.

[108] L. Apa, M. Cosentino, F. Forconi, A. Musarò, E. Rizzuto, and Z. Del Prete, "The Development of an Innovative Embedded Sensor for the Optical Measurement of Ex-Vivo Engineered Muscle Tissue Contractility," *Sensors*, vol. 22, no. 18, p. 6878, 2022, doi: 10.3390/s22186878.

[109] L. Apa, F. Martelli, E. Rizzuto, and Z. Del Prete, "Design of a new device to measure skeletal muscle engineered tissues' contractile force by using an optical tracking technique," in *Medical Measurements and Applications, MeMeA 2019 - Symposium Proceedings*, 2019, pp. 1–5, doi: 10.1109/MeMeA.2019.8802130.

[110] L. Larsson *et al.*, "Sarcopenia: Aging-related loss of muscle mass and function," *Physiol. Rev.*, 2019, doi: 10.1152/physrev.00061.2017.

[111] R. McCormick and A. Vasilaki, "Age-related changes in skeletal muscle: changes to life-style as a therapy," *Biogerontology*, vol. 19, no. 6, pp. 519–536, 2018, doi: 10.1007/s10522-018-9775-3.

[112] F. Forconi, L. Apa, C. Marianna, M. Antonio, R. Emanuele, and D. P. Zaccaria, "Effects of ROI positioning on the measurement of engineered muscle tissue contractility with an optical tracking method," *IEEE Med. Meas. Appl. MeMeA 2022 - Conf. Proc.*, 2022.

[113] J. W. Park, B. Vahidi, A. M. Taylor, S. W. Rhee, and N. L. Jeon, "Microfluidic culture platform for neuroscience research," *Nat. Protoc.*, vol. 1, no. 4, pp. 2128–2136, Nov. 2006, doi: 10.1038/NPROT.2006.316.

[114] A. Pelkonen *et al.*, "A modular brain-on-a-chip for modelling epileptic seizures with functionally connected human neuronal networks," *Biosens. Bioelectron.*, vol. 168, Nov. 2020, doi: 10.1016/J.BIOS.2020.112553.

[115] F. Forconi, M. Cosentino, E. Rizzuto, and Z. Del Prete, "Electric field distribution analysis for the design of an electrode system in a 3D neuromuscular junction microfluidic device," *IEEE Med. Meas. Appl. MeMeA 2021* -

Conf. Proc., 2021

[116] P. Shi, J. Gal, D. M. Kwinter, X. Liu, and H. Zhu, "Mitochondrial dysfunction in amyotrophic lateral sclerosis," *Biochim. Biophys. Acta*, vol. 1802, no. 1, pp. 45–51, Jan. 2010, doi: 10.1016/J.BBADIS.2009.08.012.

[117] S. V. Brooks and J. A. Faulkner, "Contractile properties of skeletal muscles from young, adult and aged mice.," *J. Physiol.*, 1988, doi: 10.1113/jphysiol.1988.sp017279.

[118] A. Moustogiannis *et al.*, "The effects of muscle cell aging on myogenesis," *Int. J. Mol. Sci.*, 2021, doi: 10.3390/ijms22073721.

[119] R. N. Baumgartner, K. M. Koehler, L. Romero, and P. J. Garry, "Serum albumin is associated with skeletal muscle in elderly men and women," *Am. J. Clin. Nutr.*, 1996, doi: 10.1093/ajcn/64.4.552.

[120] L. Rao, Y. Qian, A. Khodabukus, T. Ribar, and N. Bursac, "Engineering human pluripotent stem cells into a functional skeletal muscle tissue," *Nat. Commun.*, vol. 9, pp. 1–12, 2018, doi: 10.1038/s41467-017-02636-4.

[121] F. Forconi *et al.*, "Development of a Novel Technique for the Measurement of Neuromuscular Junction Functionality in Isotonic Conditions," *Cell. Mol. Bioeng.*, 2022, doi: 10.1007/s12195-022-00721-3.

[122] M. Martini, G. Dobrowolny, M. Aucello, and A. Musarò, "Postmitotic Expression of SOD1G93A Gene Affects the Identity of Myogenic Cells and Inhibits Myoblasts Differentiation," *Mediators Inflamm.*, vol. 2015, 2015, doi: 10.1155/2015/537853.

[123] T. Weiland, "Discretization Method for the Solution of Maxwell's Equations for Six-Component Fields.," *AEU-Archiv fur Elektron. und Ubertragungstechnik*, 1977.

[124] H. Kim *et al.*, "Single-neuronal cell culture and monitoring platform using a fully transparent microfluidic DEP device," *Sci. Rep.*, vol. 8, no. 1, pp. 1–9, 2018, doi: 10.1038/s41598-018-31576-2.

[125] A. Semisch, J. Ohle, B. Witt, and A. Hartwig, "Cytotoxicity and genotoxicity of nano - and microparticulate copper oxide: Role of solubility and intracellular bioavailability," *Part. Fibre Toxicol.*, vol. 11, no. 1, pp. 1–16, 2014, doi: 10.1186/1743-8977-11-10.

[126] H. Nakano and H. Sato, "A chemical potential equalization approach to constant potential polarizable electrodes for electrochemical-cell simulations," *J. Chem. Phys.*, vol. 151, no. 16, 2019, doi: 10.1063/1.5123365.

[127] S. Mucio-Ramírez and O. Makeyev, "Safety of the Transcranial Focal Electrical Stimulation via Tripolar Concentric Ring Electrodes for Hippocampal CA3 Subregion Neurons in Rats," *J. Healthc. Eng.*, vol. 2017, 2017, doi: 10.1155/2017/4302810.

[128] M. K. McDonald, K. E. Capasso, and S. K. Ajit, "Purification and microRNA profiling of exosomes derived from blood and culture media," *J. Vis. Exp.*, no. 76, 2013, doi: 10.3791/50294.

[129] J. S. Kwon *et al.*, "Characterization of βARKct engineered cellular extracellular vesicles and model specific cardioprotection," *Am. J. Physiol. Heart Circ. Physiol.*, vol. 320, no. 4, pp. H1276–H1289, Apr. 2021, doi: 10.1152/AJPHEART.00571.2020.

[130] J. S. Kwon, E. W. Barr, J. K. Chuprun, and W. J. Koch, "In vivo stimulation of α-and β-adrenoceptors in mice differentially alters small rna content of circulating extracellular vesicles," *Cells*, vol. 10, no. 5, May 2021, doi: 10.3390/CELLS10051211/S1.

[131] M. Conceição *et al.*, "Engineered extracellular vesicle decoy receptor-mediated modulation of the IL6 trans-signalling pathway in muscle," *Biomaterials*, vol. 266, p. 120435, Jan. 2021, doi: 10.1016/J.BIOMATERIALS.2020.120435.

[132] X. Li, J. Baker, T. Cracknell, A. R. Haynes, and G. Blanco, "IGFN1_v1 is required for myoblast fusion and differentiation," *PLoS One*, vol. 12, no. 6, pp. 1–24, 2017,

doi: 10.1371/journal.pone.0180217.

8. List of publications

F. Forconi, L. Apa, S. Pisu, I. Casola, A. Musarò, E. Rizzuto, Z. Del Prete, "Development of a novel technique for the measurement of neuromuscular junction functionality in isotonic conditions", *Cellular and Molecular Bioengineering*, 2022.

L. Apa, M. Cosentino, F. Forconi, A. Musarò, E. Rizzuto, Z. Del Prete, "Development of an innovative embedded sensor for the measurement of an ex-vivo engineered muscle tissue contractility by an optical method", *Sensors*, 2022.

F. Forconi, L. Apa, M. Cosentino, A. Musarò, E. Rizzuto, Z. Del Prete, "Effects of ROI positioning on the measurement of engineered muscle tissue contractility with an optical tracking method", *IEEE Medical Measurements and Applications, MeMeA 2022-Conference Proceedings*, 2022.

F. Forconi, L. Apa, L. D'Alvia, M. Cosentino, E. Rizzuto, Z. Del Prete, "Electric field distribution analysis for the design of an electrode system in a 3D neuromuscular junction microfluidic device", *IEEE Medical Measurements and Applications, MeMeA 2021-Conference Proceedings*, 2021.

F. Forconi, F. Martelli, S. Pisu, A. Musarò, E. Rizzuto, Z. Del Prete, "Optimal force evaluation for isotonic fatigue characterization in mouse Tibialis Anterior muscle", *IEEE Medical Measurements and Applications, MeMeA 2020-Conference Proceedings*, 2020.

9. Point by point response to the reviewers

Reviewer #1

The thesis deals with innovative techniques, measurement devices, and procedures for the measurement of muscle and neuromuscular junction (MNJ) functionality in Amyotrophic Lateral Sclerosis (ALS). The developed models could be transferred also to diverse neurodegenerative pathologies. In particular, the candidate developed and validated a technique for the in-situ measurement of murine Tibialis Anterior (TA) NMJ functionality, introducing the Isotonic Neurotransmission Failure (INF) parameter, which increases at the end-stage of the disease, meaning that the NMJ functionality is more impaired in isotonic conditions. She also proposed a non-invasive system to measure the 3D engineered skeletal muscle tissues contractility, capable to discriminate between healthy and pathological conditions. Finally, she designed and realized a 3D microfluidic device to promote the formation of NMJ between spinal cord-derived neuronal cells and 3D engineered skeletal muscle, resulted useful for the development of a more comprehensive 3D NMJ in-vitro model. The candidate also performed experiments with muscle cells populations to evaluate the role of SOD1G93A mice-derived extracellular vesicles (EVs) - involved in ALS pathological proteins transportation – on the proposed models; these EVs increase during the disease progression, impairing cells differentiation. The thesis is generally written quite well and the English is fluent; however, thoroughly re-reading the text could help in the correction of eventual typos or grammatical errors, as well as in improving the use of punctuation, hence enhancing the thesis readability. Some considerations: - The candidate presents an overview of the pathology and, after having presented her studies aims, reports the results. I would suggest reconsidering the index organization, since presenting the results at first and the materials and methods after could be misleading for the reader. However, it is more a matter of style. - A spacing should be always present between a number and related measurement unit. -

Regarding the acronym, please spell them out only once, when used for the first time. Also, a section dedicated to acronyms explanation could be added at the beginning of the thesis. - When referring to an article, even if (co-)authored by the candidate, please be sure to rephrase the content, in order to decrease the similarity score. The contextualization in the literature background is quite complete; however, some references should be added, as reported more in detail in the following comments. Moreover, please check the references format, since not all the citations seem to be complete (e.g. see Ref. 115).

I would like to deeply thank the reviewer for his appreciation, suggestions and comments.

Some specific comments and suggestions are provided below in order to help the candidate to improve the quality of the manuscript.

- Page 8, last line: the acronym NMJ should not be spelled out here, since it has been previously used. Please check and explain it only when used for the first time. It is advisable to check this aspect for all the acronyms used in the thesis.

Done.

- Page 9: it could be used to add a figure indicating the different types of muscles interested in the early pathogenesis, for the sake of clarity. Also a table summarizing the different effects of ALS on muscles and motor units could be added, together with the related bibliographic references.

I would like to thank the reviewer for this suggestion. It has to be noted that the different types of muscles interested in the early pathogenesis of ALS progression are a constantly developing research topic. For this reason, according to the studies already presented in literature on Tibialis Anterior or EDL, I added the requested table (Tab. 1) to summarize the different effects of ALS

on muscles and motor units at the end of paragraph 2.1 of Introduction section.

- Page 12: is it possible to quantify the "significant errors" present in isotonic fatigue protocols? It would be interesting to add this information.

Yes, it concerns what we analysed for a conference paper [F. Forconi et al., *IEEE Medical Measurements and Applications, MeMeA 2020 - Conference Proceedings*, 2020]. In particular, we demonstrated that when the muscle was allowed to shorten against the experimental optimal force rather than the reference value, the coefficient of variation (CV) of all isotonic fatigue parameters strongly decreased. For example, the coefficient of variation (CV) for the fatigue time decreased from 61.4% to 18.4% when experimental optimal force was employed.

- Page 14: it would be interesting to add a brief consideration on the measurement accuracy of the methods described from literature.

Thank you for this suggestion. As regarding the Si-MEMS device developed by Shimizu et al. [K. Shimizu et al., *Biomed. Microdevices*, 2010], to achieve reliable and reproducible measurements of the active tension of skeletal muscle tissues, it would be necessary to investigate the relationship between the number of cultured myotubes and the active tension. As regarding the Traction Force Microscopy, this system does not provide a direct measurement of the engineered skeletal muscle contractile force, but of the contraction and relaxation velocities curves, where contractility is usually presented as a percentage of the movement. To this, the indirect measurement of contractile force results affected by the effect of propagation of uncertainty. These considerations on the measurement accuracy of the proposed devices were added.

- Page 17: the second paragraph repeats a concept already reported at the end of page 16. Please rephrase it or consider deleting one of the two items.

Done.

- Pages 18-19: it could be useful to add a table summarizing the findings on EVs role in neurodegenerative diseases from literature.

Thank you for this suggestion. The role and effects of EVs in neurodegenerative diseases were summarizes in Tab. 2 in paragraph 2.4 of Introduction section.

- Chapter 4 (page 22): as mentioned above, the title "Results" could be misleading, since the reader expects to read first Materials and Methods section, then Results. Please evaluate to modify it to fix this possible issue for readability, or, alternatively, to move this Section (and related Discussion, Chapter 5) after M&M one. As a further alternative, Materials and Methods section and Results section for each research item presented in the thesis could be placed in a same section. However, as already said, it is more a matter of style.

Thanks for this suggestion. However, the thesis was written according to a template provided by the MIT PhD course.

- Figg. 3-4: it would be interesting to try to justify the reduction in the variance when muscles are tested at the optimal experimental force.

Thank you for this comment. The reduction in the variance when muscle was tested at the experimental optimal force rather than at the reference value was due to the fact that at the experimental optimal force the muscle developed its real maximum power, and not a power that could be quite close but also very different from

this maximum value. Indeed, by testing control mice to lift a load equal to the experimental optimal force during isotonic fatigue protocol, their behaviour was quite similar and, therefore, the variance of all the parameters measured in isotonic fatigue protocol strongly decreased. This consideration was added in the Discussion section.

- Fig. 5: it could be useful to number the 5 phases labels, for the sake of readability.

Done, I modified the figure number 5 by adding labels to each phase of the stimulation protocol.

- Page 27: please homogenise the number of digits when expressing the duration of pulse trains/resting periods.

Done.

- Fig. 6: please improve the readability of the text in this figure.

Done, the format was increased.

- Pag. 31: for the sake of clarity, it could be useful to report the equation related to the computation of relative error in the force determination.

Done, the requested equation was added.

- Fig. 20: it could be interesting to report also a picture of the developed sensor.

Thank you for this comment. A picture of the embedded sensor is already present in paragraph 6.2.2. of Materials and Methods section (Fig. 41).

- Page 53: for the sake of clarity, it should be specified how simulations were performed (e.g. which software was used?).

I added the information of the software used for the electric field propagation simulation. Of note, a more detailed description is present in Materials and Methods section (paragraph 6.2.3.).

- Page 57: a brief description of a possible option to overcome the encountered issue could be interesting.

The idea of the new device configuration would be to decrease the wide of the device to avoid as much as possible the penumbra zone resulted by using confocal microscopy. This information was added at the end of the paragraph.

- Fig. 36: please consider placing the subfigure b at the bottom of subfigure a, in order to improve readability.

Fig. 36 was modified to improve its readability.

- Chapter 6: please consider moving this section before Results (Chapter 4), for the same motivations exposed above.

Thanks for this suggestion. However, the thesis was written according to a template provided by the MIT PhD course.

- Section 6.2: a brief introduction could be added before starting with the first subparagraph (i.e. 6.2.1).

A brief introduction of section 6.2 was added by explaining the techniques, testing protocols and devices proposed before their explanation in the specific materials and methods paragraphs.

- Page 71: for the sake of clarity, it could be useful to report a scheme of the whole measurement setup used for the measurement of NMJ functionality.

The schematic of the experimental set-up for the measurement of muscle and NMJ functionality was added in Fig. 40 as subfigure a.

- Page 72: the choice of the two groups numerosity should be justified. Moreover, it could be useful to add a table reporting the computed parameters and their description, for the sake of clarity.

The numerosity of the two groups was chosen according to the sample size equation, which considers the z-score, the confidence interval and the margin of error. Moreover, the measured parameters were already descripted in paragraph 4.1.1 of Results section.

- Page 74: a proper reference should be added in relation to the choice of the displacement range.

The displacement range was chosen as that expected from the force generated by the X-MET reported in Carosio et al. and Pisu et al. Indeed, these two references were added at the end of the paragraph.

- Fig. 42: the subfigure c should be enlarged (or reported as a separate figure) for the sake of readability and to better understand what described at pages 79-80.

The subfigure c was enlarged to increase its readability.

- Section 6.2.3: a scheme of the proposed 3D microfluidic device could be added for ease of readability.

The schematic of the proposed 3D microfluidic device is represented in Fig. 27 in 4.1.3. section of Results section.

- Section 6.3.3: it could be useful to add a figure showing the detection of EVs through flowcytometric analysis.

A figure showing the flowcytometric analysis for the visualization of EVs was added as Fig. 44.

- Section 6.3.4: please add proper references to the last sentence of this paragraph.

A reference [M. Conceição et al., *Biomaterials, 2021*] was added at the end of the paragraph.

- Section 6.3.7: an example of figure related to microscope confocal analysis could be added for the sake of clarity.

Figures related to confocal microscopy analysis are already present in Results section, where the results obtaining by using EVs to treat C2C12 cells are showed.

- Section 6.4: proper references should be added for each statistical method that is mentioned in this section. Moreover, something about the normality of the distribution of the considered variables should be stated.

As regarding the un-paired Student's t-test, it requires a parametric distribution of the variables, previously verified, while Mann-Whitney test is a non-parametric t-test, previously verified. For 2 and 3-way ANOVA, the distribution of the considered variables is not parametric. These considerations were added in 6.4 section of Materials and methods section.

Reviewer #2

Overall, the thesis is a very nice example of combining engineering skills with biological skills. Having a similar background (many years ago…), I really appreciated this transversal approach to address the biological questions. The force measurements done both through the nerve as well as directly on the muscle are a very elegant way to determine key aspects of NMJ functionality. Also, the in-depth analysis of muscle functionality, not just limited to force production, but also analysing velocity and power curves, make this a very strong thesis in muscle physiology. The ALS model of the

SOD mice always leave me wondering how representative it is. This is confirmed by the functional evaluations, which show a very significant muscle phenotype already in what is defined as a pre-symptomatic phase**.** The critical role of muscle in this pathology is clearly show by the fact that direct muscle stimulation shows already very significant decreases. Something that would have been a nice addition to this thesis would be some muscle histology at the different times (either H&E, or if one has more time some electron microscopy). This would link the functional deficits to potential histological alterations observed in the tissue. While I clearly liked the overall thesis, there are some minor changes I would suggest:

First, I would like to deeply thank the reviewer for his appreciation and suggestions. Of note, the experimental results of NMJ functionality will be deeply validate by a biological point of view through molecular and histological analysis at the different stages of ALS progression.

- In some cases, new concepts are not introduced clearly enough, for example CFSE-positive vesicles. CFSE is not introduced, nor is it explained what it binds. This should be changed. The same is true for the 'treated' group in the X-MET…what is the treatment? What is the accelerated aging mentioned?

Thanks for these suggestions. The CFSE (Carboxyfluorescein succinimidyl ester) is a membrane-permeable fluorescent dye. As the dye diffuses into the cell, its succinimidyl group covalently binds to intracellular lysine residues and other free primary amines, producing green fluorescence. This information was added in paragraph 6.3.2 of Materials and Methods section. As regards the treatment of the X-MET, it was described in the paragraph 6.2.2. of Materials and Methods section. In particular, X-MET is maintained in culture in differentiation medium, constituted of DMEM high glucose, 5% horse serum, 4mM L-glutamine, 0,1% gentamicin,

penicillin/streptomycin. Historically, serum and others addition factors have been used by default as a crucial component of cell culture medium, as a supplier of complex biological molecules such as hormones, growth factors, attachment factors and numerous nutrients that enable cell growth, proliferation and differentiation (Geoffrey L. Francis, *Cytotechnology*, 2010) .To assess whether our system is able to capture alterations in the contractile force of the three-dimensional construct, we cultured X-MET in a serum-free medium enriched with bovine serum albumin (BSA). As the main protein of several sera, such as fetal bovine serum or horse serum, albumin has been indicated as the most important factor associated with successful attempts to maintain cells in the absence of serum. Epidemiological studies indicate that age-related decline of muscle mass and strength (sarcopenia) is associated with decreased levels of growth factors. Based on this evidence, we wondered whether the X-MET's morpho-functional properties could be impinged by reduced levels of growth factors and whether this culture conditions mimic the aged microenvironment.

- Some phrases are not clear, for example: Page 59: "As shown in Fig. 34, it is possible to note a different efficiency of fusion among EVs collected from transgenic and control mice, except for the presymptomatic stage.". Where can one see different fusion efficiency? More in general, how can one see a change in a dynamic process like fusion in a single image?

The different fusion efficiency of EVs to proliferating myoblasts after 6 hours of treatment, as well as to completely differentiated myotubes, can be seen through the computation of Mean Fluorescence Intensity (MFI) on images acquired at confocal microscopy. In particular, when the $CFSE^{+}$ EVs fuse to the myoblasts by realising their cargo, the cell cytoplasm turns to green. At this point, if the cell cytoplasm results greener than another, it is due to the fact that more EVs fuses to the first cell, in comparison to

the other. Therefore, in our case, by confocal microscopy analysis, it was possible to note a different efficiency of fusion among EVs collected from transgenic to control mice, except for the presymptomatic stage.

- Figure 33 in a way shows that the number of vesicles is not a critical factor in the phenotype observed in the SOD mice as muscle function is strongly impaired at all stages, however vesicle content/number is quite different in late stage disease. Figure 39b: is the decrease in the wt+EV group vs. control group not significant? If it is, why is this?

The decrease of the differentiation index is not statistically significant between cells treated with WT mice-derived EVs and untreated cells.